ANALYSIS OF ADD/DROP OPTICAL WAVEGUIDE FILTERS WITH EMBEDDED RESONANT CAVITIES USING THE METHOD OF LINES

MOHAMMAD MAHBUBUL ISLAM

ELECTRICAL ENGINEERING

April 2005

KING FAHD UNIVERSITY OF PETROLEUM & MINERALS

DHAHRAN 31261, SAUDI ARABIA

DEANSHIP OF GRADUATE STUDIES

This thesis, written by

MOHAMMAD MAHBUBUL ISLAM

under the supervision of his thesis Advisor and approved by his Thesis Committee, has been presented to and accepted by the Dean of Graduate Studies, in partial fulfillment of the requirements for the degree of

MASTER OF SCIENCE IN ELECTRICAL ENGINEERING

Thesis Committee

_____

Dr. Hussain A. Al-Jamid (Chairman)

_____

Dr. H. M. Y. Masoudi (Member)

_____

Dr. Sheikh Sharif Iqbal (Member)

_____
Dr. Jamil M. Bakhashwain
Department Chairman

_____
Dr. Mohammad Abdulaziz Al-Ohali
Dean of Graduate Studies

Date: _____

ii

Dedicated to my parents and my wife

Acknowledgements

Table of Contents

List of Tables

List of Figures

Nomenclature

English Symbols

E   electric field vector, volts/meter

H   magnetic field vector, amperes/meter

N diagonal matrix of refractive-index squared at mesh grids

I identity matrix

P time-averaged power per unit length in the y-direction, watts/m

Q matrix of the eigen-value equation

n refractive index

k_o free space wavenumber, radians/meter

h mesh size, meter

d, ω thickness of a layer, meter

j $\sqrt{-1}$

t time, sec

Greek Symbols

ψ general field component of the **E** or **H** field

Ψ general field component of the **E** or **H** sampled field, column vector

ε_0 free space permittivity, $4\pi \cdot 10^{-7}$ Vs/Am

ε_r relative permittivity

μ_0 free space permeability, $8.8541 \cdot 10^{-12}$ As/Vm

μ_r relative permeability

$\omega = 2\pi f$ angular frequency, rad/sec

α_m mth modal field coefficient

β propagation constant, radians/meter

λ wavelength, meter

∇ nabla operator, $\dfrac{\partial}{\partial x}\hat{a}_x + \dfrac{\partial}{\partial y}\hat{a}_y + \dfrac{\partial}{\partial z}\hat{a}_z$

∇^2 Laplace operator, $\dfrac{\partial^2}{\partial x^2} + \dfrac{\partial^2}{\partial y^2} + \dfrac{\partial^2}{\partial z^2}$

Abbreviations

TE Transverse Electric

TM Transverse Magnetic

MOL Method of Lines

PML Perfectly Matched Layer

BPM Beam Propagation Method

ABC Absorbing Boundary Condition

SIT	Semi Infinite Termination
WDM	Wavelength Division Multiplexing
n_{eff}	Modal Effective Index
λ_B	Bragg Wavelength
Re	Real part of a complex number
Im	Imaginary part of a complex number

Subscripts

A_x, A_y, A_z	x, y, z components of a vector **A**
$\psi_i, \psi_{i-1}, \psi_{i+1}$	sample number of field ψ
$\psi_{i^{\pm}}, \psi_{i-1^{\pm}}, \psi_{i+1^{\pm}}$	field immediately to the left or to the right of a sample point

Superscript

$\psi^{(1)}$	first derivative of ψ
$\psi^{(2)}$	second derivative of ψ
$\psi^{(3)}$	third derivative of ψ
$\psi^{(4)}$	fourth derivative of ψ
$\psi^{(5)}$	fifth derivative of ψ
$\psi^{(6)}$	sixth derivative of ψ
$A*$	complex conjugate of A

THESIS ABSTRACT

Name: MOHAMMAD MAHBUBUL ISLAM

Title: ANALYSIS OF ADD/DROP OPTICAL WAVEGUIDE FILTERS

                                WITH EMBEDDED RESONANT CAVITIES USING THE

                                METHOD OF LINES

Degree: MASTER OF SCIENCE

Major Field: ELECTRICAL ENGINEERING

Date of Degree: APRIL 2005

Narrow band filters are important elements of integrated optical circuit. Resonant cavities imbedded between two identical parallel waveguides result in compact narrow band Add/Drop filter. In this thesis work, such add/drop filters are analyzed using the Method of Lines (MOL).Add/drop filter with square, circular and elliptical cavities are investigated. The spectral response of the four port filter and the power loss spectrum are obtained. The MOL using the Layer by Layer Algorithm is applied to model the add/drop filters. In addition, the MOL with improved features is presented in this work. This included improved implementation of the transverse second derivative operator and the incorporation of a Perfectly Matched layer (PML).

Calculated results show that the Add/drop filter with an embedded circular cavity give much better spectral response when compared to the square and elliptical cavities. Almost complete optical power drop from the bus to one of the receiver ports can be achieved in the circular cavity case.

Keywords: Method of Lines (MOL), Perfectly Matched Layer (PML), Narrow Band Filter, Add/Drop Filter, Directional Coupler.

Master of Science Degree

King Fahd University of Petroleum and Minerals, Dhahran.

April 2005

ملخص الرسالة

الاسم	محمد محبوب الاسلام
عنوان الرسالة	تحليل مرشح قائد موجة إضافة وإزالة بصري ذا فجوات رنين باستخدام طريقة الخطوط
الدرجة	الماجستير في العلوم
القسم	الهندسة الكهربائية
تأريخ منح الدرجة	2005/5 م

تعتبر المرشحات البصرية ضيقة المدى الطيفي من العناصر المهمة في الدوائر البصرية المدمجة. ويمكن بناء هذه المرشحات بوضع فجوة رنين بين قائدي موجة متطابقين ومتوازيين مما يؤدي إلى إنتاج مرشحات إضافة وإلقاء ضيقة المدى وصغيرة الحجم. نقوم عبر هذه الرسالة بتحليل عمل مثل هذه المرشحات باستخدام طريقة رقمية تدعى طريقة الخطوط.

وقد استخدمنا طريقة الخطوط لمحاكاة عمل مرشحات إضافة وإزالة تحتوي على فجوات رنين مربعة الشكل ودائرية الشكل بالإضافة إلى مرشحات رنين على شكل قطع مكافيء. حيث قمنا بحساب طيف الرنين للأطراف الأربعة للمرشح وكذلك حساب طيف خسارة الطاقة.

طريقة الخطوط استعملت مع إسلوب الطبقات مع إضافة طبقة مثالية ماصة للأشعة بالإضافة إلى إستخدام تقريب دقيق للمشتقة الثانية للدالة.

وقد تبين لنا من نتائج المحاكاة بأن استعمال فجوة رنين دائرية الشكل يؤدي إلى طيف رنين أفضل من طيف الرنين الناجم عن الفجوة المربعة الشكل والفجوة التي على شكل قطع مكافيء. حيث وجدنا بأن معظم الطاقة البصرية تنتقل من مدخل المرشح إلى أحد مخارجه عند استخدام فجوة رنين دائرية الشكل.

درجة الماجستير في العلوم
جامعة الملك فهد للبترول والمعادن
الظهران، المملكة العربية السعودية

Chapter 1

Introductions

1.1 Integrated Optics

An integrated circuit which consists of miniature optical components connected via waveguides on a transparent dielectric substrate is known as an Optical integrated circuit (OIC). It performs operations similar to integrated electronic circuits for switching, modulation, filtering and signal processing. In the OIC the signal is carried by means of beams of light rather than electric current. The concept of integrated optics was first proposed in 1969 by S. E. Miller of Bell labs [1, 2].

The OIC is the third generation of optical devices. It has advantages such as reduced weight, higher bandwidth and multiplexing capacity, immunity to electromagnetic interference, low transmission loss, higher thermal and mechanical stabilities, low power consumption etc, over the previous technologies [3]. Due to the high information carrying capacity, OICs have promising aspects in the field of telecommunications.

One of the most promising applications of the integrated optics is in the field of optical fiber communications. The optical fiber has assumed importance because of its high information carrying capacity; it is here that integrated optics will play an important role in optical signal processing at the transmitting and receiving ends and on regeneration at the repeaters [4]. Other important applications are envisaged to be spectral analysis, optical signal processing and wavelength division multiplexing (WDM).

OICs are designed to perform certain functions by integrating a laser diode as the source, functional components, such as switches/modulators, and interconnection waveguides and photodiodes as detectors, on a single substrate. Through integration, a more compact, stable, and functional optical system can be expected. OICs are divided into three types from the standpoint of materials. When the three basic components (source, waveguide and detector) are all integrated on a single substrate, the device is called a monolithic OIC. Compound semiconductors, such as GaAs and InP, can be the candidate substrates for these OICs. When the three components are made of three different materials, the device is called a Hybrid OIC. A Quasi-hybrid or Quasi-monolithic OIC is an intermediate between the monolithic and hybrid OICs. Both quasi-hybrid and hybrid types consist of dielectric-film waveguides. Quite recently silicon has

been used to produce optical sources, waveguides, and detectors. The advantage of silicon is the compatibility to standard microelectronics technology. Electronic, optoelectronic and optical circuits can be implemented on one substrate (silicon) reducing fabrication costs and increasing the device reliability. The transformation of optical signals into electrical signals can also be realized monolithically on a chip up to a wavelength of 1.1μm. One disadvantage of silicon at this time is that it is not still an efficient light source.

1.2 Optical Waveguide

The optical waveguide is a structure which can confine light waves and propagate them over a distance with considerably low transmission losses due to the phenomenon of total internal reflection (TIR). The most extensively used optical waveguide is the optical fiber which is a cylindrical waveguide. To obtain TIR, the reflective index of the cladding material is always kept lower than that of the waveguide core materials.

According to the refractive index profile, the waveguides can be classified into two main categories, the step index and the graded index waveguides. The step index waveguide has a uniform refractive index profile in each layer and the graded index waveguide has a continuously varying index profile.

From the point of view of confinement of light, waveguides can be classified into two main categories, the planar waveguide and the channel waveguide. In the planar waveguides, confinement of light energy is achieved only along one transverse dimension

(and light energy can diffract in the other direction), and the channel (or the strip) waveguide, confines the light energy in both transverse directions.

Due to the theoretical and computational difficulties in modeling waveguides having a two dimensional confinement, this thesis work will only address waveguide structures with one dimensional confinement.

1.3 Directional Coupler and Add/drop Filter

Directional couplers are passive devices that are used to couple optical or microwaves signals from one waveguide to another.

The waveguides used in directional couplers may or may not be connected physically. Directional couplers are important for many applications in integrated optics. They can be used as power dividers, wavelength filters and for light switching and modulation. Directional Couplers can be of many types. For example: diffusion couplers, area-splitting couplers and beam splitter couplers, Wavelength Selective couplers [5]. In its simplest form, a directional coupler consists of two parallel dielectric waveguides in close proximity as shown in figure 1.1 (a). In this case, the power coupling is based on optical interference between the evanescent fields of the two waveguides, such that a light wave launched into one of the waveguides can be coupled completely into the other waveguide [6].

Resonators have also been used as channel dropping devices. A resonant cavity imbedded between two parallel waveguide is shown in figure 1.1 (b). This structure is

known as Add/Drop filter. The resonant cavity can be of different shapes such as square, circular, elliptical etc. If the resonators are small enough so that the spacing of the resonant frequencies accommodates the set of wavelength division multiplexing (WDM) channels within the communications window, the goal of dropping one channel by a filter without affecting the other channels can be achieved. Add/drop with resonant cavities of various shapes have been reported in the literature [7, 8, 9, 10, 11].

(a) Directional Coupler   (b) Add/Drop Filter
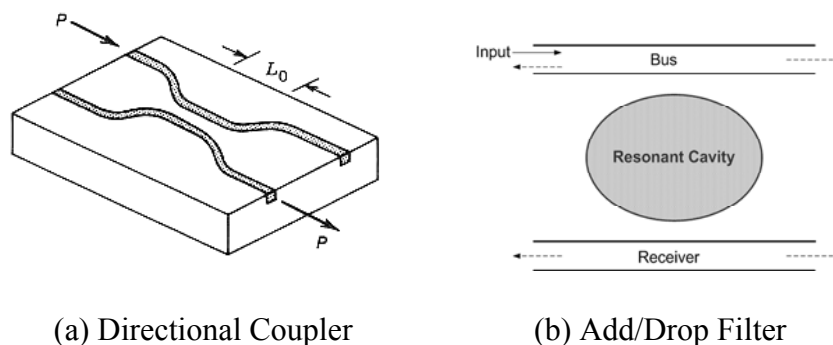
Figure 1.1: Directional Coupler and Add/Drop Filter

In the thesis, wavelength selective drop/add filters as shown in Figure 1.1(b) are considered. The basic add/drop filter considered in this thesis work consists of two identical and parallel single mode slab waveguides, coupled by a resonant cavity of various shapes. The cavity shapes we considered are single and multiple square cavities, circular cavities and elliptical cavities with different cavity size. We will investigate the effect of the various cavity shapes and sizes on the add/drop efficiencies, spectral widths, the number of channels and device power loss through radiations.

1.4 Numerical Techniques for Modeling Optical Waveguide Structures

For the last two decades, analysis and modeling of optical waveguides has been an important research topic. Several numerical methods have been developed to model waveguide structures. Among these methods are the Beam Propagation Method (BPM) [5, 12, 13], the Finite Difference Time Domain (FDTD) Method [13, 14], the Collection Method [15], the Mode Matching Method (MMM) [16] and the Method of Lines (MOL) [13, 17, 18].

The FDTD is one of the most widely used numerical techniques. It is universal, robust, methodologically simple and descriptive. The wave propagating through the structure is found by a direct integration in the time domain of Maxwell's equations in discretized form. Discretization is done both in time and in space using a staggered grid. The main shortcoming of the FDTD method is its high computational demand.

The BPM is the most widely used numerical method for the modeling of integrated and fiber-optic devices. It also involves a discretization of the electromagnetic field. It is computationally efficient, and methodologically simpler than the FDTD. The main underlying assumption in the BPM is the use of the slow varying envelope approximation, along the direction of the field propagation, leading to the parabolic form of the wave equation. In addition, the BPM generally assumes slow changes in the waveguide profile.

The Collocation Method is based on the Helmholtz equation, and does not require the Fresnel approximation for its implementation [4]. In this method, the field is expanded into a set of suitable orthogonal basis functions in the transverse direction. The choice of the basis functions depends on the problem geometry. Since these basis are not eigen-modes of the problem, we need a large number of basis functions to achieve accurate results.

The MOL is a well established and efficient numerical procedure for the analysis of a variety of optical and microwave waveguides. Its advantages stem from the fact that it is a semi analytical approach that leads to comparatively small numerical effort and high accuracy. The MOL can easily account for the backward reflected field and the forward transmitted field as well as its ability to account for optical structures with large refractive index contrast. This is an important advantage leading to the popularity of the MOL in analyzing longitudinally inhomogeneous structures. The MOL will be used in this thesis to analyze the add/drop filter shown in figure 1.1(b)

1.5 Overview of the Thesis

1.5.1 Objectives of the Thesis

The objective of this thesis is to address the following

- Developing a general 2D MOL based program. The program employs an improved higher order approximation of the transverse second derivative operator with appropriate interface conditions, a Perfectly Matched Layer (PML) absorber

that utilizes a non-uniform loss profile and the layer by layer approach in order to effectively simulate optical structures with multiple longitudinal discontinuities.

- Analyses of the filtering performance of the add/drop filter with different imbedded cavity shapes. The resonant cavities that will be considered are the square, the circular and the elliptical cavity shapes as shown in Figure 1.2. The previously developed general 2D MOL program will be used in the analysis of these odd/drop filters. The add/drop filters are simulated using MOL for 2D structures and the results are analyzed for their filtering performance.

| (a) Square Cavity | (b) Circular Cavity | (c) Elliptical Cavity |
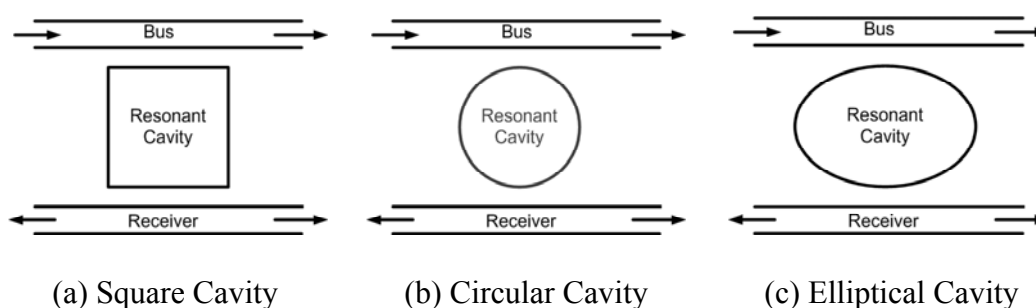
Figure 1.2: Add/Drop Filter with Different Cavity Shapes

1.5.2 Organization of the thesis

This thesis is organized in a comprehensive manner so that the reader may easily follow the progress of the work. It starts by reviewing of the basic slab waveguide theory and proceeds to our results and discussions of the optical device of interest, the optical add/drop filter.

The introductory chapter, chapter one, gives an overview of the thesis work. In this chapter integrated optics, optical waveguides, directional couplers and add/drop filters are introduced. The numerical techniques used for modeling optical waveguide structures are also discussed in briefly.

The basic planar optical waveguide (dielectric slab waveguide) is discussed in chapter two. The theory of wave transmission and reflection from longitudinal discontinuities is presented briefly. The eigenvalue equation of both the transverse electric (TE) and transverse magnetic (TM) guided modes of the three layer step index dielectric slab waveguide are also presented.

Chapter three introduces the MOL, which is used in the solution of the wave equation in the present thesis. The mathematical formulation of the MOL is presented. Then, extensions of the MOL, using improved higher order approximations of the transverse second derivative operator and interface conditions are discussed. The implementation of the PML absorber with graded loss profile is then explained. The above mentioned extensions of the MOL are applied and used in later chapters to calculate response of the directional couplers and add/drop filters.

In chapter four, the MOL analysis of longitudinal waveguide discontinuities is presented. The layer by layer algorithm in discussed which is then applied for the simulation of multiple longitudinal waveguide discontinuities. Waveguide structures with a single and multiple longitudinal discontinuities are simulated and the results are compared with published results to verify the accuracy of the simulations.

Chapter five introduces the directional coupler which consists of two parallel waveguides. The basic principles of coupling between two parallel waveguides are discussed and the response of the four ports of a directional coupler, calculated using the MOL, is presented. The effect of the waveguide separation on the coupling length is numerically calculated and compared with the theoretical results.

Chapter six and seven are devoted to the analysis of the add/drop filter with square, circular and elliptical cavities. Their basic principles and wavelength response are presented. The effect of the cavity size and air gap width between the cavity and the waveguides are also analyzed to find out the best filter response. At the end of these two chapters comparisons among the filtering responses and the behavior of the various add/drop filters are discussed.

The final chapter, chapter eight, summarizes the work presented, concludes and suggests future extensions of the thesis work.

Chapter 2

Dielectric Slab Optical Waveguides

2.1 Introduction

One of the simplest forms of optical waveguide structures is the dielectric slab waveguide. The guided and radiation modes of the slab waveguide can easily be described because of its simple geometry. The study of slab waveguide is important for the understanding of the wave-guiding properties of more complicated dielectric waveguides. Moreover they are also important for light-guidance in integrated optical circuits [19, 20, 21, 22]. In this chapter, the theory of the planar dielectric waveguide is briefly explained.

2.2 Three Layer Step Index Dielectric Slab Waveguide

The three layer step index planar dielectric waveguide is one of the simplest forms of waveguides. A three layer planar waveguide is shown in figure 2.1. The middle region, the core, is deposited on a layer called the substrate and covered by a superstrate layer which is also known as the cladding. The light wave propagates through the core which has a higher refractive index than the two adjacent regions.
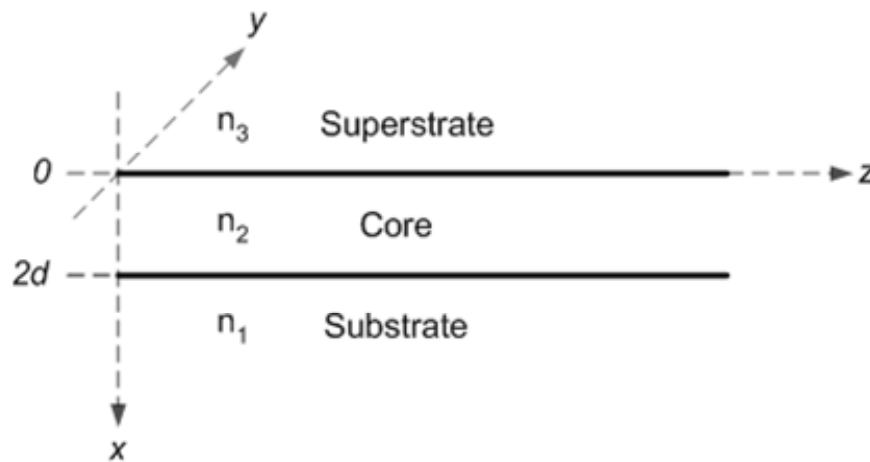
Figure 2.1: A Three-Layer Dielectric Slab Waveguide

2.2.1 The Wave Equation

The planar dielectric slab waveguide of figure 2.1 is assumed to have three non-magnetic and homogenous layers. A time-harmonic field variation of the form $e^{-j\omega t}$ is assumed. For TE polarized waves, the time harmonic two dimensional scalar wave equation which is derived from the Maxwell's equations is given by:

$$\frac{\partial^2 E_y}{\partial x^2} + \frac{\partial^2 E_y}{\partial z^2} + k_0^2 n^2 E_y = 0 \qquad (2.1)$$

Where E_y is the electric field component, k_0 is the free space wave number ($k_0 = 2\pi / \lambda_0$), λ_0 is the free space wavelength and n is the refractive index of any layer (core, superstrate or substrate). In the derivation of equation 2.1, it has been assumed that $\frac{\partial}{\partial y} = 0$, which is valid for infinite and uniform structures in the y-direction. In order to obtain a modal solution corresponding to wave propagation in the z direction, the field is assumed to vary as $e^{j\beta z}$ in the z direction (β is the longitudinal propagation constant). In this case equation 2.1 reduces to the well known Helmholtz equation:

$$\frac{d^2 E_y}{dx^2} + (k_0^2 n^2 - \beta^2) E_y = 0 \qquad (2.2)$$

Using equation 2.2 and imposing the boundary conditions at the substrate-core and the superstrate-core interfaces, the modal solutions (guided modes) of the structure as well as the corresponding propagation constants can be obtained.

2.2.2 Guided Modes of the Symmetric Dielectric Slab Waveguide

A symmetric slab waveguide is characterized by identical media above and below the core layer, which means that the substrate and the superstrate materials are the same. A symmetric slab waveguide supports a finite number of guided modes and an infinite number of radiation modes. In order to achieve guidance, the refractive index of the core

(n_1) of a symmetric slab waveguide has to be higher than the refractive indices of the substrate and superstrate (n_2).

The guided modes of a symmetric slab waveguide are either even or odd in their transverse field distributions, as shown in figure 2.2. This waveguide constitutes a limiting case of an asymmetric waveguide. The number of guided modes that can be supported by a symmetric slab waveguide as shown in figure 2.1 depends on the thickness *2d*, the wavelength λ and the indices of refraction n_1 and n_2.
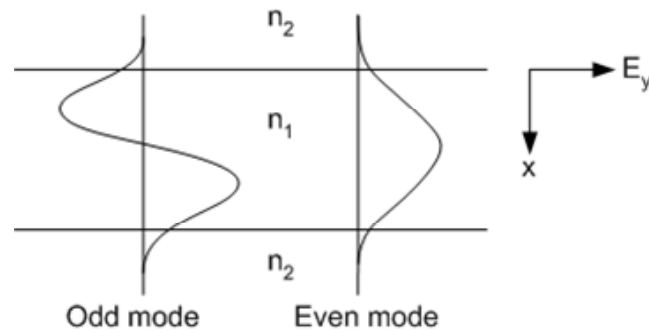
Figure 2.2: Electric Field Distribution in a Symmetric Slab Waveguide.

2.2.3 Transverse Electric (TE) Guided Modes

By solving equation 2.2 in each layer of the slab waveguide shown is figure 2.1 (along with the application of the boundary condition which requires continuity of E_y), the single nonzero electric field component E_y of the TE polarized wave can be obtained. Using Maxwell's equations, the corresponding two non-zero components of the magnetic field

H_x and H_y can also be obtained. The filed components of the TE polarized waves are given by:

$$E_y = \begin{cases} Ae^{-qx} & ,x \geq 0 \\ A\cos(qx) + B\sin(qx) & ,0 \geq x \geq -2a \\ (A\cos(2aq) - B\sin(2aq))e^{p(x+2a)} & ,x \leq -2a \end{cases} \qquad (2.3)$$

$$H_x = -\frac{\beta}{\omega\mu_0}E_y \qquad (2.4)$$

$$H_z = -\frac{j}{\omega\mu_0}\frac{\partial E_y}{\partial x} \qquad (2.5)$$

Substituting equation 2.3 in equation 2.5, and again applying the boundary conditions for the continuity of H_z, the following TE eigenvalue equation can be obtained.

$$\tan(2aq) = \frac{q^2 + pq}{q^2 - pq} \qquad (2.6)$$

where $q^2 = n_1^2 k_0^2 - \beta^2$, $p^2 = \beta^2 - n_2^2 k_0^2$. Equation 2.6 relates the wavelength, refractive indices, core thickness and propagation constant. The longitudinal propagation constant β is the only unknown quantity in equation 2.6, and hence it can be easily obtained. An example of the TE mode patterns for a three-layer symmetric slab waveguide is shown in figure 2.3. The core width is 1 μm with refractive index 3.6. Both the substrate and superstrate are 2.5 μm wide with refractive index 3.4.

TE Modes of a Waveguide

Symmetric TE$_0$ mode

Exponentially decaying
evanescent field outside
the giude core

Sinusoidal field
inside the guide

Antisymmetric TE$_1$ mode

E$_y$

x-axis
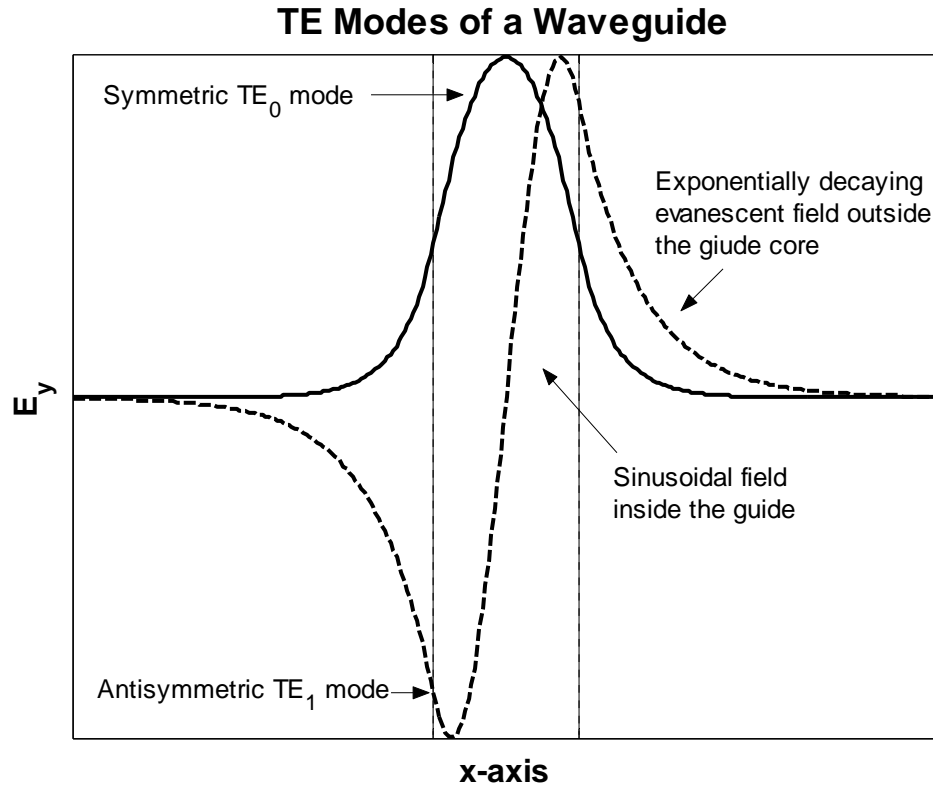
Figure 2.3: TE Mode Patterns in a Symmetric Slab Waveguide

2.2.4 Transverse Magnetic (TM) Guided Modes

Solving equation 2.2 (when it is in terms of the magnetic field H_y), the only non zero

magnetic field component H_y for TM polarized waves can be obtained in all the three

regions as

$$H_y = \begin{cases} Ce^{-qx} & ,x \geq 0 \\ C\cos(qx) + D\sin(qx) & ,0 \geq x \geq -2a \\ (C\cos(2aq) - D\sin(2aq))e^{p(x+2a)} & ,x \leq -2a \end{cases} \qquad (2.7)$$

Using Maxwell's equations, the two non-zero components of the electric field namely E_x

and E_y are given by

$$E_x = -\frac{\beta}{\omega n_i^2 \varepsilon_0} H_y \qquad (2.8)$$

$$E_z = -\frac{j}{\omega n_i^2 \varepsilon_0} \frac{dH_y}{dx} \qquad (2.9)$$

If we proceed in a similar fashion as done in the TE case, an eigenvalue equation for the TM modes can also be obtained as

$$\tan(2aq) = \frac{n_1^2 n_2^2 (p+q)}{n_2^5 q - n_1^4 p} \qquad (2.10)$$

An example of the TM polarized modal field for a symmetric slab waveguide is shown in figure 2.4. It can be seen that H_y is continuous at the layer interfaces but its first derivative is discontinuous there, causing a sudden change in the slope of H_y.
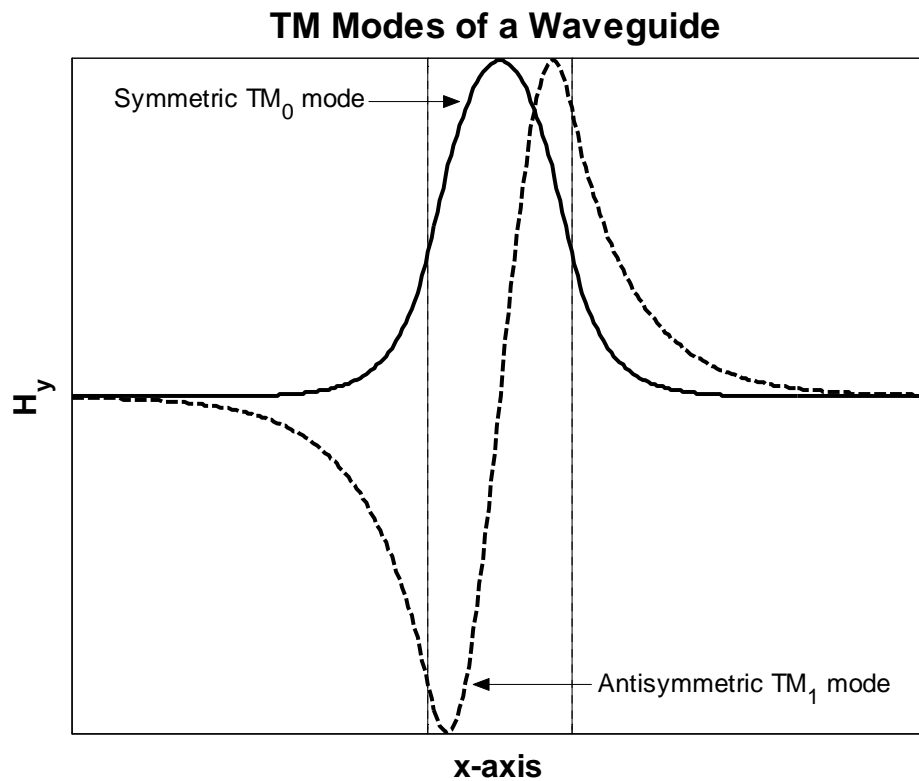
Figure 2.4: TM Mode Patterns in a Symmetric Slab Waveguide

Chapter 3

The Method of Lines (MOL) and its

Extensions

3.1 Introduction

The MOL is one of the various numerical algorithms that have been utilized for the analysis of waveguide structures and devices. This numerical method has been applied to numerous planer longitudinal uniform and nonuniform waveguide problems, including guided wave problems with abrupt longitudinal discontinuities. Using the MOL, numerical solutions of waveguides with single [23, 24] and multiple discontinuities [25, 26, 27, 28, 29, 30, 31] have been reported in the literature. The method has also been used

to model three dimensional structures [32, 33, 34], non-linear waveguides [35] and the diffraction problems from waveguide ends [36]. In order to solve the two dimensional wave equation using the MOL, the field is first discretized in one direction (the transverse direction, x) and then solved analytically in the direction of wave propagation (z direction) [37, 38, 39].

3.2 Basic MOL Algorithm

The MOL has been used to analyze guided optical structures exhibiting longitudinal discontinuities. The waveguide interfaces are kept parallel to the direction of propagation (z axis) and the field is discretized along the transverse direction (x-axis) as shown in figure 3.1. The discretization points are kept equidistant leading to a uniform mesh size Δx. In order to terminate the problem space, the structure under study is considered to be bounded by an electric wall where $E_y = 0$ or a magnetic wall where $H_y = 0$. The presence of these walls results in spurious numerical reflection at the edges of the computational window. The reflections from these walls can be eliminated by use of perfectly matched layers (PML) as will be discussed later. The resulting set of difference equations is then decoupled and manipulated through algebraic transformations.

In some instances, it might be more advantageous to have a non-equidistant discretization, leading to a nonuniform mesh size. An example of this is the case when the widths of the different layers of the structure exhibit extreme differences which results in increasing the number of lines and, consequently the associated computational time and

memory requirements. In such cases, the mesh size is increased in regions where the field exhibits slow variations and vice-versa [40, 41].
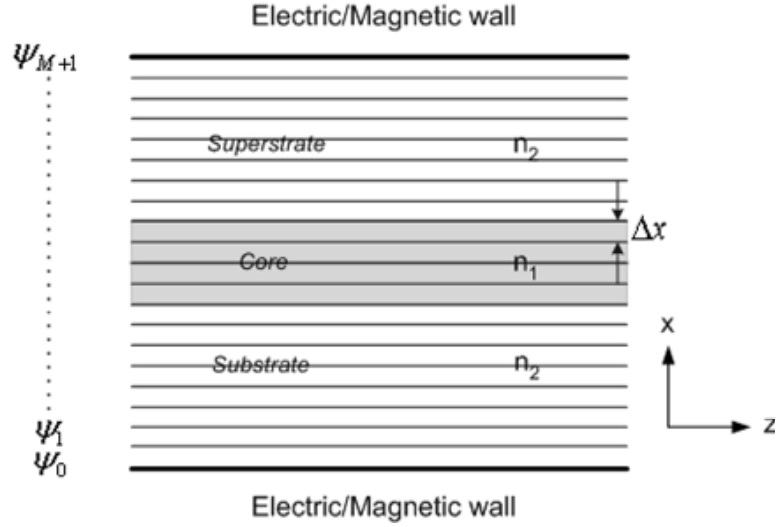
Figure 3.1: Mesh Discretization used in the MOL

3.3 Mathematical formulation

Consider the two-dimensional wave equation

$$\frac{\partial^2 \psi(x,z)}{\partial x^2} + \frac{\partial^2 \psi(x,z)}{\partial z^2} + k_0^2 n^2 \psi(x,z) = 0 \tag{3.1}$$

where ψ is the electric field E_y (for TE waves) or the magnetic field H_y (for TM waves), $k_0 = 2\pi/\lambda_0$ is the free space wave number, λ_0 is the free space wavelength and n is refractive index of the medium.

In the MOL, both the field $\psi(x,z)$ and the refractive index $n(x)$ are discretized along the x-axis and calculated analytically on the discretization lines in the z-direction

(direction of propagation). To calculate the field   in discrete form, we first need to obtain an expression for its second derivative with respect to x in discrete form. This can be accomplished using the well-known three-point central difference approximation, which is discussed in the next section.

3.3.1 The Three-Point Central Difference Approximation

To obtain an expression for the discretized second derivative of a certain function, we express the function in terms of a power series. We can have a good approximation of the given function in terms of a polynomial by neglecting all except the first few terms of the resulting series. One of the most convenient power series is the Taylor's series which can be expressed as:

$$f(x) = \sum_{n=0}^{\infty} \frac{f^{(n)}(a)}{n!}(x-a)^n \qquad (3.2)$$

where $f^{(n)}$ is the nth derivative of $f(x)$ with respect to x.

If Taylor's series is expanded about x = 0, the resulting series is often called a Maclaurin's Series expansion. Expanding $\psi(x)$ about x = 0 using equation 3.2:

$$\psi(x) = \psi_0 + \frac{\psi_0'}{1!}x + \frac{\psi_0''}{2!}x^2 + \frac{\psi_0'''}{3!}x^3 + \frac{\psi_0''''}{4!}x^4 + ... \qquad (3.3)$$

here $\psi_0 = \psi(0)$. Evaluating the above equation x = ± Δx, results in the following two equations. For the next mesh point (x = +Δx):

$$\psi_1 = \psi_0 + \frac{\psi_0'}{1!}\Delta x + \frac{\psi_0''}{2!}(\Delta x)^2 + \frac{\psi_0'''}{3!}(\Delta x)^3 + \frac{\psi_0''''}{4!}(\Delta x)^4 + ... \qquad (3.4)$$

and for the previous mesh point (x = -Δx):

$$\psi_{-1} = \psi_0 - \frac{\psi_0{}'}{1!}\Delta x + \frac{\psi_0{}''}{2!}(\Delta x)^2 - \frac{\psi_0{}'''}{3!}(\Delta x)^3 + \frac{\psi_0{}''''}{4!}(\Delta x)^4 - ....\qquad(3.5)$$

Adding the two above equations we have:

$$\psi_1 + \psi_{-1} = 2\psi_0 + \psi_0{}''(\Delta x)^2 + \frac{\psi_0{}''''}{12!}(\Delta x)^4 + ...\qquad(3.6)$$

Equation 3.6 leads to:

$$\psi_0{}'' = \frac{\psi_1 - 2\psi_0 + \psi_{-1}}{(\Delta x)^2} - \frac{\psi_0{}''''}{12!}(\Delta x)^2 - ....\qquad(3.7)$$

which can be expressed as:

$$\psi''(0) \approx \frac{\psi_1 - 2\psi(0) + \psi_{-1}}{(\Delta x)^2}\qquad(3.8)$$

It is apparent from equation 3.8 that the leading error resulting from the approximation is proportional to $(\Delta x)^2$.

3.3.2 Discretization of the Wave Equation

The second derivative operator $\left(\dfrac{\partial^2}{\partial x^2}\right)$ term in equation 3.1, is replaced by the three point central difference approximation from equation 3.8. At the *ith* grid point we have:

$$\frac{\psi_{i+1}(z) - 2\psi_i(z) + \psi_{i-1}(z)}{(\Delta x)^2} + \frac{d^2\psi_i(z)}{dz^2} + k_0^2 n_i^2 \psi_i(z) = 0\qquad(3.9)$$

If the field in the x-direction is discretized into M points, so that $i = 1, 2, 3, ... ,M$; then equation 3.9 yields the following M coupled equations:

$$i = 1: \qquad \frac{1}{(\Delta x)^2}[\psi_2 - 2\psi_1 + \psi_0] + \frac{d^2}{dz^2}[\psi_1] + k_0^2 n_1^2[\psi_1] = 0\qquad(3.10)$$

$i = 2$:
$$\frac{1}{(\Delta x)^2}[\psi_3 - 2\psi_2 + \psi_1] + \frac{d^2}{dz^2}[\psi_2] + k_0^2 n_2^2 [\psi_2] = 0 \qquad (3.11)$$

$i = 3$:
$$\frac{1}{(\Delta x)^2}[\psi_4 - 2\psi_3 + \psi_2] + \frac{d^2}{dz^2}[\psi_3] + k_0^2 n_3^2 [\psi_3] = 0 \qquad (3.12)$$

$$\vdots$$

$$\vdots$$

$i = M$:
$$\frac{1}{(\Delta x)^2}[\psi_{M+1} - 2\psi_M + \psi_{M-1}] + \frac{d^2}{dz^2}[\psi_M] + k_0^2 n_M^2 [\psi_M] = 0 \qquad (3.13)$$

The above set of equations can be written in the following matrix form:

$$\frac{1}{(\Delta x^2)}\begin{bmatrix} -2 & 1 & & & & & 0 \\ 1 & -2 & 1 & & & & \\ & 1 & -2 & 1 & & & \\ & & \ddots & \ddots & \ddots & & \\ & & & 1 & -2 & 1 & \\ 0 & & & & 1 & -2 & 1 \\ & & & & & 1 & -2 \end{bmatrix}\begin{bmatrix} \psi_1(z) \\ \psi_2(z) \\ \psi_3(z) \\ \vdots \\ \vdots \\ \vdots \\ \psi_M(z) \end{bmatrix} + \frac{d^2}{dz^2}\begin{bmatrix} \psi_1(z) \\ \psi_2(z) \\ \psi_3(z) \\ \vdots \\ \vdots \\ \vdots \\ \psi_M(z) \end{bmatrix}$$

$$+ k_0^2 \begin{bmatrix} n_1^2 & & & & \\ & n_2^2 & & & \\ & & n_3^2 & & \\ & & & \ddots & \\ & & & & \ddots \\ & & & & & n_M^2 \end{bmatrix}\begin{bmatrix} \psi_1(z) \\ \psi_2(z) \\ \psi_3(z) \\ \vdots \\ \vdots \\ \psi_M(z) \end{bmatrix} = \begin{bmatrix} 0 \\ 0 \\ 0 \\ \vdots \\ \vdots \\ 0 \end{bmatrix} \qquad (3.14)$$

The above system of equations can be written in the compact form

$$\frac{1}{(\Delta x)^2} C\Psi + \frac{d^2}{dz^2}\Psi + k_0^2 N\Psi = 0 \tag{3.15}$$

where C is a tri-diagonal second-order central-difference matrix, N is a diagonal matrix whose elements are the discrete values of the square of the refractive index in the transverse direction $(n_1^2, n_2^2, n_3^2, \ldots, n_M^2)$ and $\Psi = [\psi_1(z), \psi_2(z), \ldots, \psi_M(z)]^t$ is the discretized field vector of E_y or H_y depending on the wave polarization. The above equation may then be written in the form:

$$\frac{d^2}{dz^2}\Psi + Q\Psi = 0 \tag{3.16}$$

where

$$Q = \frac{1}{(\Delta x)^2} C + k_0^2 N \tag{3.17}$$

The general solution of the second order ordinary matrix differential equation 3.16 is formally given by [11]:

$$\Psi = e^{j\sqrt{Q}z} A + e^{-j\sqrt{Q}z} B \tag{3.18}$$

Where A and B are constant vectors having the same dimensions as Ψ. The terms $e^{\pm j\sqrt{Q}z}$ represent field propagation in the $\pm z$ direction respectively. The $M \times M$ matrices $e^{j\sqrt{Q}z}$ and $e^{-j\sqrt{Q}z}$ are evaluated by first diagonalizing Q in terms of its eigenvalues and eigenvectors, so that

$$Q = UVU^{-1} \tag{3.19}$$

where U is the eigenvector matrix and V is a diagonal matrix containing the eigenvalues of Q. The matrix exponent is then calculated using

$$e^{\pm j\sqrt{Q}z} = Ue^{\pm j\sqrt{V}z}U^{-1} \qquad\qquad (3.20)$$

3.4 Extensions of the MOL

Extensions of the MOL which result in an increase of its numerical efficiency will be discussed in this section. These extensions include, improvement to the transverse second derivative operator using an improved higher order finite difference approximation. In addition, a PML (Perfectly Matched Layer), used to absorb the rediative field, is incorporated into the MOL. The results to be presented in this chapter confirm the accuracy of our implementation.

3.5   Improved Higher Order Finite Difference Approximation of the Transverse Second Derivative Operator

The thee-point central difference approximation of the second derivative $\dfrac{\partial^2\psi}{\partial x^2}$ (section 3.3) has some major drawbacks. It is a 3-point central difference approximation with an accuracy of (Δx^2) in regions of uniform refractive index. Its accuracy however decreases at index discontinuities. Because central difference is used to derive equation 3.9, a nonuniform mesh size cannot be used in this case. Equation 3.9 also does not account properly for the TE and TM boundary conditions at material (refractive index)

discontinuities. Thus, equation 3.9 is limited to the case of low index contrast in the transverse direction. If applied to TM polarized waves in high index contrast waveguides, equation 3.9 fails and gives erroneous results. In addition, it requires a very fine mesh size (small Δx) to give an acceptable level of accuracy which leads to increased matrix size in the MOL and hence longer CPU runtime and larger memory requirement. The numerical accuracy of $\dfrac{\partial^2 \psi}{\partial x^2}$ can be improved without the use of an excessive number of discretization lines by using higher order approximations of the transverse second order derivative operator.

A higher order approximation scheme discussed in [42] will be implemented in this thesis. This technique is more efficient and more flexible than the one reported previously in [43]. It accounts for both TE and TM polarized waves and utilizes a non-uniform meshing scheme for added efficiency. This results in a reduced matrix size in the MOL, smaller computational time and lower memory usage.

In the subsequent section, a brief discussion of the interface conditions (I.Cs.) for an arbitrary mesh size and index discontinuities is given. This is followed by final expressions of the improved higher order approximation of the transverse second derivative operator algorithm, as presented in [42].

3.5.1 Interface Conditions:

For a multi-layer structures in which the material properties are uniform within each layer and change abruptly from one layer to the next at the interface, the tangential electric field E_y and its first derivative are both continuous .The tangential magnetic field H_y is continuous but its first derivative is discontinuous. All the higher order derivatives of both E_y and H_y with respect to x are discontinuous. In order to correctly model the electric and magnetic fields behavior at an abrupt interface, these interface conditions (I.Cs.) should be appropriately accounted for in the MOL formulation. We can derive these relations using Maxwell equations. For the TE polarization, using equation 2.5

$$H_z = -\frac{j}{\omega\mu_0}\frac{\partial E_y}{\partial x}$$
(3.21)

at an interface, where H_z is continuous, that is $H_z^{0^+} = H_z^{0^-}$, the above equation gives:

$$-\frac{j}{\omega\mu_0}\frac{\partial E_y^{0^+}}{\partial x} = -\frac{j}{\omega\mu_0}\frac{\partial E_y^{0^-}}{\partial x}$$
(3.22)

which leads to:

$$\frac{\partial E_y^{0^+}}{\partial x} = \frac{\partial E_y^{0^-}}{\partial x}$$
(3.23)

which is a statement of the continuity of $\dfrac{\partial E_y}{\partial x}$ at a horizontal interface. Similarly for the

TM polarization, using equation 2.9

$$E_z = \frac{j}{\omega n_j^2 \varepsilon_0}\frac{\partial H_y}{\partial x}$$
(3.24)

at an interface, where E_z is continuous, that is $E_z^{0^+} = E_z^{0^-}$, the above equation gives:

$$\frac{j}{\omega n_2^2 \varepsilon_0}\frac{\partial H_y^{0^+}}{\partial x} = \frac{j}{\omega n_1^2 \varepsilon_0}\frac{\partial H_y^{0^-}}{\partial x} \tag{3.25}$$

leading to:

$$\frac{1}{n_2^2}\frac{\partial H_y^{0^+}}{\partial x} = \frac{1}{n_1^2}\frac{\partial H_y^{0^-}}{\partial x} \tag{3.26}$$

which implies the discontinuity of $\dfrac{1}{n^2}\dfrac{\partial H_y}{\partial x}$ at any horizontal interface.

Therefore, from the above equations it can be concluded that the tangential electric field E_y and its first derivative are continuous and the tangential magnetic field H_y and

$\dfrac{1}{n^2}\dfrac{\partial H_y}{\partial x}$ are continuous.

3.5.2 Algorithm for Calculating the Improved Higher Order Transverse second Derivative Operator

There are many algorithms reported in the literature that discuss higher order approximation of the second derivative operator [43, 44]. Although these algorithms provide sufficiently high accuracy, they have some limitations. The approach of [43] has the advantage of applicability to both TE and TM polarized waves. This approach requires the use of a uniform mesh size and a uniform refractive index at two points before and two points after the discontinuity. This reduces the efficiency and flexibility of the approach.

The algorithm that will be presented here [42] does not suffer from such limitations. This algorithm will be used throughout this thesis. This improved algorithm allows both the mesh size and the refractive index to change in a completely arbitrary manner from one layer to the next, without any restrictions. This basic difference leads to a number of advantages, which includes higher flexibility, efficiency and accuracy of the results. The approach used in this reference, for obtaining higher order approximation of the transverse second derivative operator, can be easily extended to any order. Contrary to the approach presented in [43], which requires separate treatments for the points surrounding a discontinuity point, the present approach treats all point equally.

The above mentioned algorithm will not be derived here and only the relevant final expressions will be presented. The reader is referred to [42], for detailed derivation. Only the results of the 5-point approximation of $\dfrac{\partial^2 \psi}{\partial x^2}$ will be presented here. Referring to figure 3.2, the final expression for the 5-point approximation technique approximation

$$
\begin{bmatrix} \psi_i \\ \psi_{i-}^{(1)} \\ \psi_{i-}^{(2)} \\ \psi_{i-}^{(3)} \\ \psi_{i-}^{(4)} \end{bmatrix} = C^{-1} \begin{bmatrix} \psi_{i-2} \\ \psi_{i-1} \\ \psi_i \\ \psi_{i+1} \\ \psi_{i+2} \end{bmatrix}
\tag{3.27}
$$

where ψ_i is the field at the ith interface which is located to the right of the ith layer of thickness h_i and refractive index n_i. ψ_{i-} indicates the field to the left of the ith interface and ψ_{i+} indicates the field to the right of the ith interface. The superscript in $\psi^{(d)}$ denotes

the dth derivative of ψ with respect to x. ψ_{i+1} and ψ_{i-1} represents the field at next and

previous interfaces respectively. The Elements of the third row of C^{-1} provide the required

finite difference coefficients for approximating the second derivative operator. The matrix

C in equation 3.27 is defined as

$$
C \;=\;
\begin{bmatrix}
 & q_{i-1}^{-} & M_{i-1}^{-} & N_i^{-} & \\
 & & q_i^{-} & & \\
1 & 0 & 0 & 0 & 0 \\
 & & q_{i+1}^{+}M_i & & \\
 & q_{i+2}^{+} & M_{i+1}N_{i+1}^{+} & M_i &
\end{bmatrix}
\tag{3.28}
$$

where the matrices M, q and N are given below

$$
M_i^{\pm} \;=\;
\begin{bmatrix}
1 & 0 & 0 & 0 & 0 \\
0 & \rho_i^{\pm 1} & 0 & 0 & 0 \\
\mp\delta_i & 0 & 1 & 0 & 0 \\
0 & \rho_i^{\pm 1}\delta_i & 0 & \rho_i^{\pm 1} & 0 \\
\delta_i^2 & 0 & \mp 2\delta_i & 0 & 1
\end{bmatrix}
\tag{3.29}
$$

$$q_i^{\pm} = \begin{bmatrix} 1 & \pm h_i & \dfrac{h_i^2}{2!} & \dfrac{\pm h_i^3}{3!} & \dfrac{h_i^4}{4!} \end{bmatrix} \qquad (3.30)$$

$$N_i^{\pm} = \begin{bmatrix} 1 & \pm h_i & \dfrac{h_i^2}{2!} & \dfrac{\pm h_i^3}{3!} & \dfrac{h_i^4}{4!} \\ 0 & 1 & \pm h_i & \dfrac{h_i^2}{2!} & \dfrac{\pm h_i^3}{3!} \\ 0 & 0 & 1 & \pm h_i & \dfrac{h_i^2}{2!} \\ 0 & 0 & 0 & 1 & \pm h_i \\ 0 & 0 & 0 & 0 & 1 \end{bmatrix} \qquad (3.31)$$

where $\rho_i = 1$ for the TE waves and $\rho_i = \dfrac{n_{i+1}^2}{n_i^2}$ for the TM waves, and $\delta_i = k_0^2 \left(n_{i+1}^2 - n_i^2 \right)$.

The expressions corresponding to the 3-point and the 7-point approximations are presented in appendix A for reference.
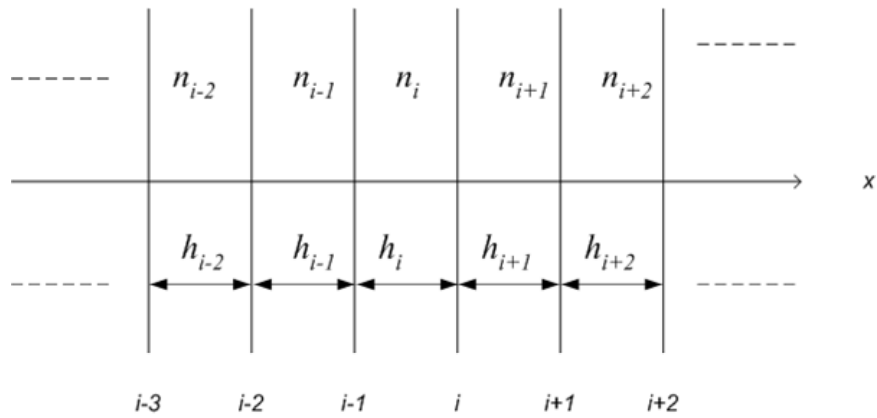
Figure 3.2: Generalized refractive index and mesh size distributions

3.5.3 Numerical Results

High contrast asymmetrical waveguide

The developed algorithm for three point central difference approximation, three point approximation with interface conditions and five point approximation of the transverse second derivative operator $\left(\dfrac{\partial^2}{\partial x^2} \right)$ are used to model the high contrast waveguide shown in the inset of figure 3.3. The effective index of the TE_0 mode and TM_0 mode of this slab waveguide is calculated using the 3 point central difference, 3 point with interface conditions and 5 point approximation as a function of the mesh size in the problem space at $\lambda_0 = 1.00 \mu m$. The outer layers thickness is kept sufficiently large so that the model field decays to a sufficiently small value before it reaches the exterior wall of the problem. The exact value of the effective index of the TE_0 mode, calculated by STF1 program (see Appendix B), is given by $n_{eff} = 3.543961609340564$. The relative error defined as

$\dfrac{\left| n_{eff,exact} - n_{eff,calc} \right|}{n_{eff,exact}}$, as a function of mesh size is shown in figure 3.3. The error is seen to

decrease smoothly as the mesh size decrease. It is observed that though the 5-point approximation requires higher computational time, it gives a better estimate of n_{eff} with relatively fewer sample points when compared to the 3-point central difference and the 3-point formulation with interface conditions.
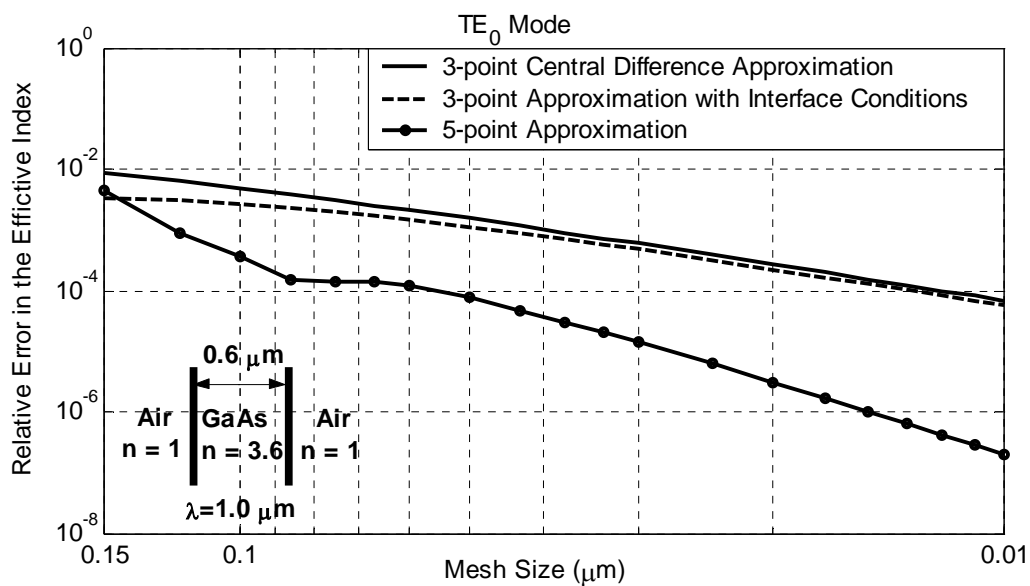
Figure 3.3: Variation of the error with the total number of mesh points (TE$_0$ Mode)
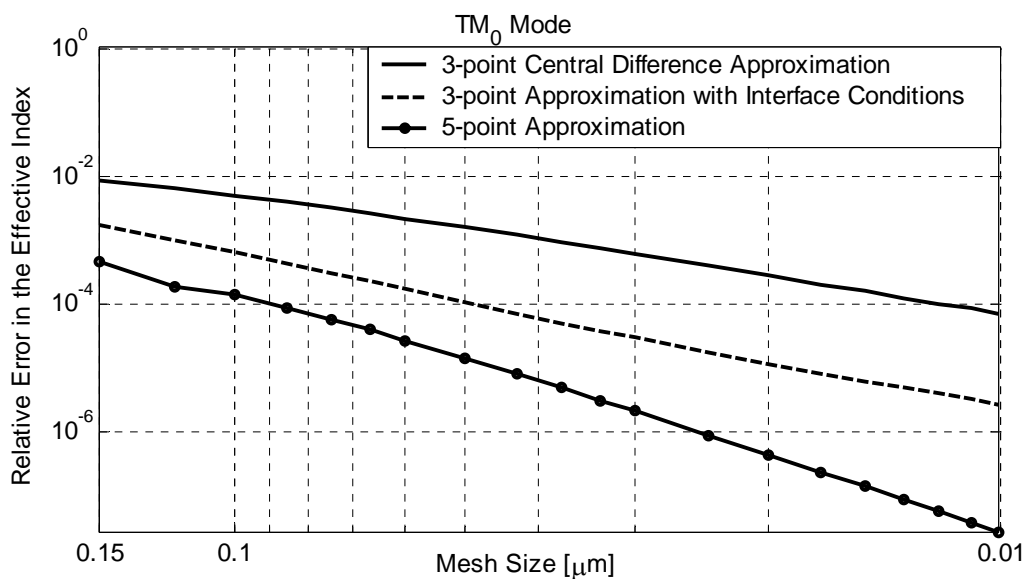
Figure 3.4: Variation of the error with the total number of mesh points (TM$_0$ Mode)

3.6 Absorbing Boundary Conditions

For the analysis of any waveguide structure, the waveguide has to be enclosed in a box called "the computational window" or "the problem space". This is done in order to limit the computational effort and model an open space problem using a finite width window. The truncation of the field at the edges of the computational window is usually obtained by assuming an electric wall $(E_y = 0)$ or a magnetic wall $(H_y = 0)$ at both edges of the computational window. The presence of these undesirable walls causes the waves to completely reflect back in to the computational window. These reflected waves interfere with the field inside the computational window, leading to error in the calculated results. In order to improve the accuracy of the MOL, absorbing boundary condition is used for the purpose of absorbing the radiated field.

3.6.1 Perfectly Matched Layer (PML)

The perfectly matched layer (PML) is an example of an absorbing boundary condition. The PML region occupies the outer edge of the computational window. In this region, space is transformed in the complex domain [45, 46].

The distance x within the PML is mapped into the complex domain according to $x \rightarrow x(1+j\sigma)$ [$\Delta x \rightarrow \Delta x(1+j\sigma)$ in discrete form]. This results in the formation of an attenuation factor in the PML (towards the inside of the PML) followed by a termination of the mesh point. The parameter $\sigma\,(\sigma\rangle 0)$ controls the spetial rate of decay within the

PML. The radiative field e^{+jkx} propagating in the $+x$ direction in the real space is transformed to:

$$e^{+jkx(1+j\sigma)} = e^{+jkx}e^{-k\sigma x}$$

(3.32)

in the complex space. The term $e^{-k\sigma x}$ results in wave attenuation in the $+x$ direction. The choice of the decay factor σ is discussed in reference [46].

If the term $\Delta x\sigma$ remains unchanged throughout the PML, then we have a uniform PML. If this term gradually increases into the PML, following a certain profile, then the PML is termed non-uniform or graded PML. In general, graded loss profiles are superior in performance to the uniform profile [47].

Inside the PML the complex mesh size h can be expressed as $h = \Delta x(1 + j\sigma) = h' + jh''$, where h_i' and h_i'' are the real and the imaginary parts of h_i, respectively.

The PML region is shown in figure 3.5, where the mesh point at the *ith* point is given by $h_i = h_i' + jh_i''$. The PML region is divided into M layers and the parameter I take the values $i = 1,2,.......,M$. The real part of h_i is chosen to have a fixed valuefor all i. In the following we describe an approach for the implementation of the PML loss profile through h_i''. Let us define the parameter $x_i = ix_0$ (i $=$ $1,2,......,M$), where $x_0 = (\pi/2)/(M+1)$. For a uniform PML loss profile, we set:

$$h_i'' = (\eta/M)$$

(3.33)

which is independent of *i*. In the case of a nonuniform PML loss profile, h_i'' is chosen to be an increasing function ot *i*. In this thesis work, we select the tangent loss profile, which is characterized by

$$h_i'' = (\eta / M)\tan(x_i) \tag{3.34}$$

The reader is referred to reference [47] for more details.
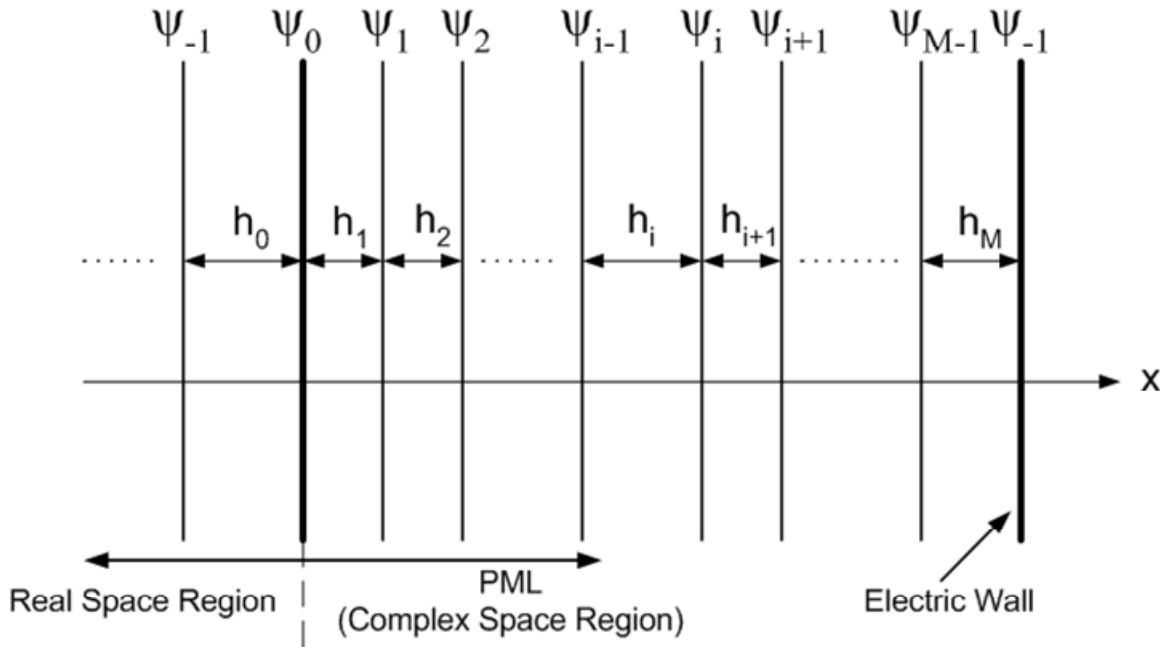
Figure 3.5: PML incorporated with slab waveguide

3.6.2 Numerical Results for a PML with Tangent Loss Profile

Figure 3.6 show a Gaussian beam of spot size 0.75 μm propagating through air (refractive index = 1) at different distances. The computational window width is 12 μm and the mesh

size is 50 *nm*. The Gaussian beam is calculated for two cases, when the computational window has no PML layers and when the computational window is terminated with PML layers of tangent loss profile. Without any PML layer the Gaussian beam reflects from the electric walls back into the computational window as it propagates. When the PML with tangent loss profile are present there is absolutely no reflections from the electric walls and the Gaussian beams propagates without any interference.
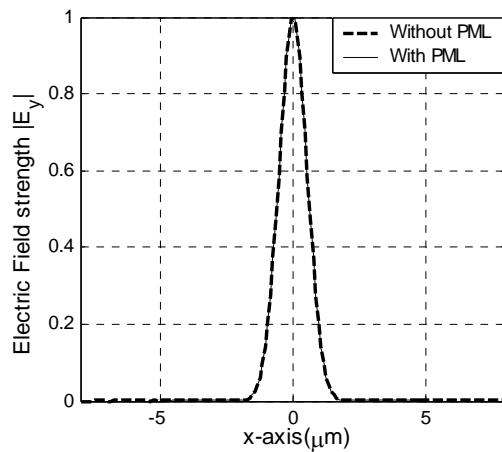
(a) Gaussian beam at the input
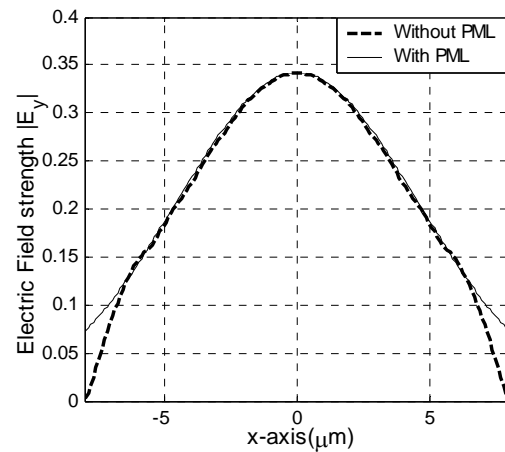
(b) Gaussian beam after 15 *μm*
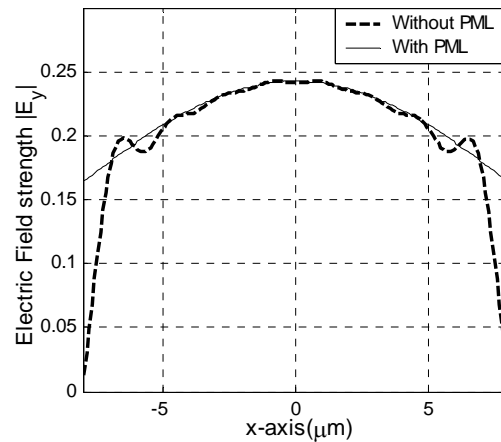
(c) Gaussian beam after 30 *μm*

Figure 3.6: Gaussian Beam Propagation with and without PML

Chapter 4

MOL Analysis of Longitudinal Waveguide Discontinuities

4.1 Introduction

Discontinuity problems in optical waveguide devices are of considerable theoretical and practical interest. They play an important role in designing practical devices such as tapers, bends, couplers, mode converters, filters, waveguide junctions, etc. Much effort has been made to understand the reflection and transmission phenomena at a longitudinal discontinuity.

The solution of the classical problem of mode scattering from a single and multiple waveguide discontinuities solved with different analytic and numerical techniques can be found in the literature. The methods used are the Mode Matching Method [49], the Method of Lines [50, 51, 52, 53], and the Equivalent Transmission Network Method [54]. The MOL is especially suitable for the analysis of longitudinal discontinuities in optical waveguides, because it can account for both the transmitted and the reflected fields.

The add/drop filter analyzed in this thesis work will be simulated by considering it as a structure with multiple discontinuities. Thus, in order to simulate the add/drop filter correctly, the MOL must account correctly for the reflection and transmission at multiple longitudinal discontinuities. In this chapter, MOL treatment of single and multiple discontinuity problems will be presented. This includes derivation of a simple expression for the single discontinuity case and a derivation of a general procedure (the Layer by Layer Procedure) for the treatment of the multiple discontinuity case. The MOL results will be compared with previously published results in order to demonstrate the accuracy of our implementation.

4.2 Analysis of a Single Waveguide Discontinuity

A single longitudinal discontinuity separating longitudinally uniform waveguide regions, region 0 and region 1 is shown in figure 4. The incident field in region 0, (z < 0) results in a backward reflected field in the same region and a transmitted field in region 1, (z > 1). The total field in each region is the summation of the forward field, represented by $e^{+jSz}A$,

and the backward field represented by $e^{-jSz}B$, where $S = \sqrt{Q}$. Thus the total field in region

0 is the sum of the incident field $e^{+jS_0z}A_0$ and the reflected field $e^{-jS_0z}B_0$, and in region 1,

only the transmitted field $e^{+jS_1z}A_1$ exists.
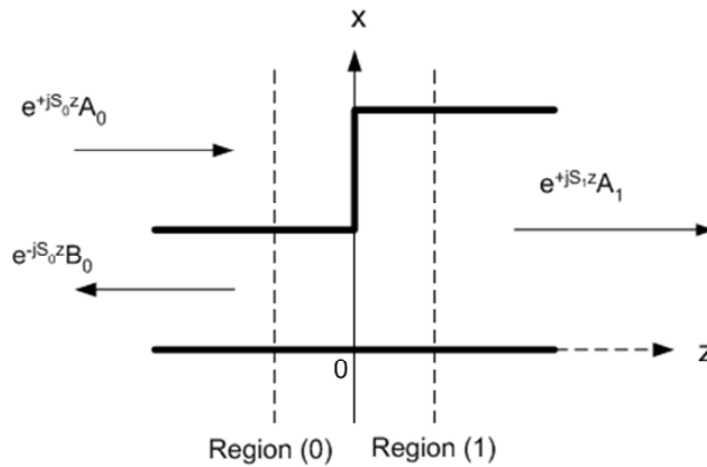
Figure 4.1: A Single Waveguide Discontinuity

The total fields Ψ_0 and Ψ_1 in region 0 and 1, respectively are thus given by:

$$\Psi_0 = e^{+jS_0z}A_0 + e^{-jS_0z}B_0 \tag{4.1}$$

$$\Psi_1 = e^{+jS_1z}A_1 \tag{4.2}$$

where Ψ is a column vector containing the sampled fields. A_0, B_0 and A_1 are constant

vectors. A_0 and B_0 are the incident and the reflected field in region 0 at $z = 0$. A_1 is the

transmitted field in region 1 at $z = 0$. $S = \sqrt{Q}$ and Q is defined in chapter 3 (equation

3.17).

By applying the appropriate boundary conditions at the longitudinal interface $z = 0$, it is possible to express the reflected field B_0 and the transmitted field A_1 in terms of the incident field A_0.

The boundary condition at the interface between region 0 and region 1 along the z-axis are given by:

$$\Psi_0\big|_{z=0^-} = \Psi_1\big|_{z=0^+} \tag{4.3}$$

and

$$\psi'\big|_{z=0^-} = \psi'\big|_{z=0^+} \qquad \text{(For TE waves)} \tag{4.4}$$

$$\frac{\psi'}{n^2}\bigg|_{z=0^-} = \frac{\psi'}{n^2}\bigg|_{z=0^+} \qquad \text{(For TM waves)} \tag{4.5}$$

The above boundary condition will be implemented for TM polarized waves. The results can then easily be modified to account for TE polarized waves. From equation 4.1 and 4.2, we have:

$$A_0 + B_0 = A_1 \tag{4.6}$$

For TM polarized waves, the fields in region 0 and region 1 are related by:

$$\left(N_0\right)^{-1} \Psi_0' = \left(N_1\right)^{-1} \Psi_1' \tag{4.7}$$

where the matrix N_0 and N_1 are the diagonal matrix of refractive indices squared n_i^2 at each sample point of region 0 and region 1 respectively as shown in equation 3.15. Differentiating equation 4.1 with respect to z and evaluating the result at the interface $z = 0$, we have:

$$\Psi'_0 = jS_0 e^{jS_0 z} A_0 - jS_0 e^{-jS_0 z} B_0 \tag{4.8}$$

$$\Psi'_0\big|_{z=0} = jS_0 \left(A_0 - B_0 \right) \tag{4.9}$$

similarly from equation 4.2:

$$\Psi'_1 = jS_1 e^{jS_1 z} A_1 \tag{4.10}$$

$$\Psi'_1\big|_{z=0} = jS_1 A_1 \tag{4.11}$$

substituting equation 4.9 and 4.11 into equation 4.7 and simplifying we have:

$$\left(A_0 - B_0 \right) = S_0^{-1} \left(N_0 \right) \left(N_1 \right)^{-1} S_1 A_1 \tag{4.12}$$

By eliminating B_0 from equations 4.6 and 4.12, we get the transmitted field, A_1:

$$A_1 = 2 \left(I + S_0^{-1} N_0 N_1^{-1} S_1 \right)^{-1} A_0 = TA_0 \tag{4.13}$$

where I is the identity matrix and T is the transmission matrix. Similarly eliminating A_0 from equation 4.6 and 4.12 we obtain the reflected field B_0:

$$B_0 = \left(I - S_0^{-1} N_0 N_1^{-1} S_1 \right) \left(I + S_0^{-1} N_0 N_1^{-1} S_1 \right)^{-1} A_0 = RA_0 \tag{4.14}$$

where R is the reflection matrix.

The results shown in equations 4.14 and 4.15 are valid for TM polarized waves only. For TE polarized waves, both the field Ψ and its first derivative with respect to z are continuous across the interface (see equation 4.3 and 4.5), which necessitate replacing the matrix $N_0 N_1^{-1}$ by the identity matrix I. The resulting relations for TE polarized waves are given by:

$$A_1 = 2 \left(I + S_0^{-1} S_1 \right)^{-1} A_0 = TA_0 \tag{4.15}$$

$$B_0 = \left(I - S_0^{-1} S_1 \right) \left(I + S_0^{-1} S_1 \right)^{-1} A_0 = R A_0 \qquad (4.16)$$

The transmission and the reflection matrices at a single longitudinal discontinuity are related by:

$$A_1 = B_0 + A_0 = \left(R + I \right) A_0 = T A_0 \qquad (4.17)$$

thus:

$$T = I + R \qquad (4.18)$$

4.2.1 Numerical Results for a single waveguide discontinuity

The single longitudinal waveguide discontinuity shown in figure 4.2(a) is simulated at λ = 1.55 μm using MOL five-point approximations with 7.5nm mesh size. The TE_0 mode is assumed to be incident from the left hand side of the discontinuity (region 0). The waveguide core widths are 0.3 μm and 0.6 μm in region 0 and region 1, respectively. The waveguide core has a refractive index of 3.6, deposited on a substrate of refractive index 3.4 and surrounded on the top by air (the refractive index of air equals to 1). The incident field results in a reflected field in region 0 in the opposite direction and a transmitted field in region 1 in the same direction as the incident field. The computational window is terminated with a layer PML at the end of the x-axis. The results are shown in figure 4.2 along with the results of reference [58]. This reference uses the same waveguide dimensions and refractive indices as shown in figure 4.2(a). it also uses the MOL based on a five-point approximation and a PML with uniform loss profile for simulations.

Figure 4.2(b) shows the incident field in region 0 which is the source field propagated to the discontinuity, figure 4.2(c) shows the reflected field in region 0, and 4.2(d) shows the transmitted field at region 1. The results show agreement with the reference results.

(a) Single longitudinal
waveguide discontinuity

(b) Incident Field in regions 0
(at the discontinuity, $z = 0$)

(c) Reflected Field in regions 0
(at the discontinuity, $z = 0$)

(d) Transmitted Field in regions 1
(at the discontinuity, $z = 0$)
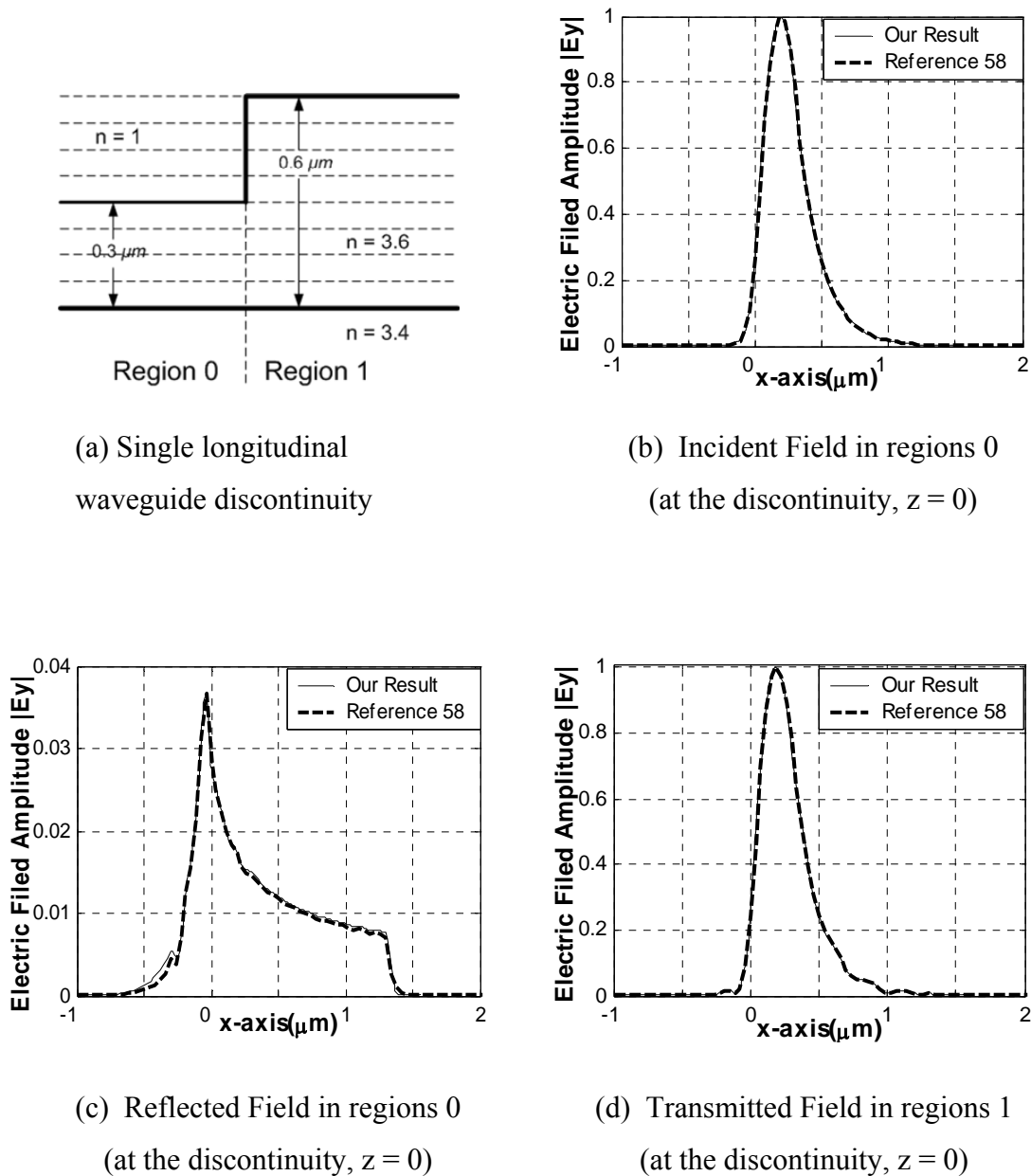
Figure 4.2: Fields at a single discontinuity

4.3 The Layer by Layer Algorithm

The MOL is widely used for the analysis of multiple waveguide discontinuities. A number of algorithms such as the cascading and doubling algorithm and the layer by layer algorithm are used with the MOL for the analysis of such waveguide discontinuities [55, 56, 57]. Here, we present the Layer by Layer Algorithm [55], which will be used throughout the thesis to account for multiple waveguide discontinuities in the longitudinal direction.

Consider the multi-layer structure shown in figure 4.3.
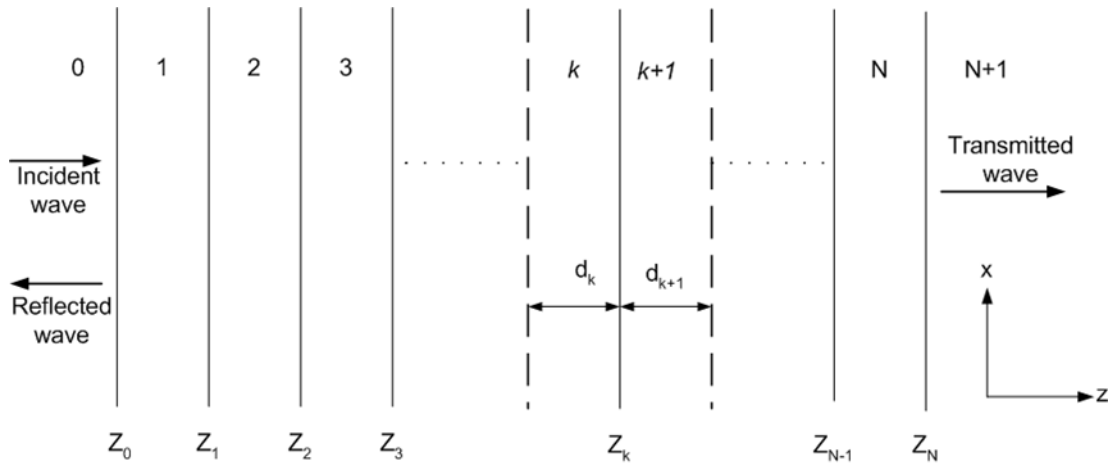
Figure 4.3: Multiple waveguide discontinuities in the z direction.

The total field in each region along z-axis is the sum of the forward and the backwards waves, that is:

$$\Psi_0 = e^{+jS_0 z} A_0 + e^{-jS_0 z} B_0 \tag{4.19}$$

$$\Psi_1 = e^{+jS_1 z} A_1 + e^{-jS_1(z-z_1)} B_1 \tag{4.20}$$

$$\vdots$$

$$\Psi_k = e^{+jS_k(z-z_{k-1})} A_k + e^{-jS_k(z-z_k)} B_k \tag{4.21}$$

$$\vdots$$

$$\Psi_{N+1} = e^{+jS_{N+1}(z-z_N)} A_{N+1} \tag{4.22}$$

In figure 4.3, the wave is assumed to be incident on the interface located at $z=0$ from the left. In the right most region of the figure, region $N+1$, the wave is assumed to propagate without reflection in the $+z$ direction. The boundary condition for TM polarized waves requires the continuity of the field ψ and $\frac{1}{n^2}\frac{d\psi}{dz}$. Applying these boundary condition at $z = z_k$ (equation 4.21), results in the following relationships [55]

$$e^{jS_k d_k} A_k + B_k = A_{k+1} + e^{jS_{k+1} d_{k+1}} B_{k+1} \tag{4.23}$$

and

$$N_k^{-1} S_k \left(e^{jS_k d_k} A_k - B_k \right) = N_{k+1}^{-1} S_{k+1} \left(A_{k+1} - e^{jS_{k+1} d_{k+1}} B_{k+1} \right) \tag{4.24}$$

For TM polarized waves, by defining $U_i = N_i^{-1} S_i$, equation 4.24 can be rewritten as

$$U_k \left(e^{jS_k d_k} A_k - B_k \right) = U_{k+1} \left(A_{k+1} - e^{jS_{k+1} d_{k+1}} B_{k+1} \right) \tag{4.25}$$

From equation 4.23 and 4.24, it can be shown that [55]

$$B_k = 0.5[\left(I - U_k^{-1} U_{k+1} \right) A_{k+1} + \left(I + U_k^{-1} U_{k+1} \right) D_{k+1} B_{k+1}] \tag{4.26}$$

and

$$D_k A_k = 0.5[(I + U_k^{-1} U_{k+1}) A_{k+1} + (I - U_k^{-1} U_{k+1}) D_{k+1} B_{k+1}] \qquad (4.27)$$

where $D_k \equiv \exp(jS_k d_k)$. By introducing the square matrix Γ_k, the relation between the incident and the reflected field at an interface may be expressed as:

$$B_k = \Gamma_k (e^{jS_k d_k} A_k) = \Gamma_k (D_k A_k) \qquad (4.28)$$

Substituting equation 4.28 into equations 4.26 and 4.27 and after some manipulations, we obtain:

$$\Gamma_k = [(I - U_k^{-1} U_{k+1}) + (I + U_k^{-1} U_{k+1}) D_{k+1} \Gamma_{k+1} D_{k+1}] \times$$
$$(I + U_k^{-1} U_{k+1}) + (I - U_k^{-1} U_{k+1}) D_{k+1} \Gamma_{k+1} D_{k+1}]^{-1} \qquad (4.29)$$

where $k=0, 1, 2,...., N$; $d_0 = d_{-1} = 0$ and $B_{N+1} = 0$ (since there is no reflected field in the transmission region, $k = N+1$). This recursive relationship expresses the reflection matrix Γ_k of layer k in terms of the reflection matrix Γ_{k+1} of layer $k+1$ for TM polarized waves. The last layer (transmission layer) has only a forward wave and hence $\Gamma_{N+1} = 0$. We start from the last layer and work backward to find out the reflection matrices until Γ_0 is computed. Using $B_0 = \Gamma_0 D_0 A_0 = \Gamma_0 A_0$, we are able to obtain the reflected field B_0 in terms of the incident field A_0 for any number of discontinuities in z-direction. Then the incident field A_0 and the reflected field B_0 of the region 0 can be used to calculate the transmitted field of the next region (region 1) with the following expression:

$$A_{k+1} = 0.5[(I + U_{k+1}^{-1} U_k) D_k A_k + (I - U_{k+1}^{-1} U_k) B_k] \qquad (4.30)$$

The reflected field of region 1 is then calculated by substituting the calculated values of the transmitted fields of region 1 in equation 4.28. Thus using equation 4.30 and 4.28

along with the values of the reflection matrices for each layer, Γ_k, the transmitted and the reflected fields of any layer can be calculated gradually for TM polarized waves.

For TE polarized waves reflection matrices, transmitted fields and reflected fields can be calculated by defining $U_i = S_i$ in equation 4.29 and 4.30.

4.3.1 Numerical Results for a double discontinuity

The waveguide with two longitudinal discontinuities shown in figure 4.4(a) has been simulated using the Layer by Layer algorithm in the MATLAB environment. The transmitted and the reflected fields when the TM$_0$ mode is incident from the left are compared with the results in reference [58]. The results of reference [58] agree with our results signifying the accuracy of our simulations. However the reflected field shown in figure 4.4 (c) has some differences. this minimal differences are due to the facts that, the reference simulations used a PML with a uniform loss profile and a Higher-order finite difference Approximations and in our case a PML with a tangent loss profile and improved higher-order finite difference approximations are employed.
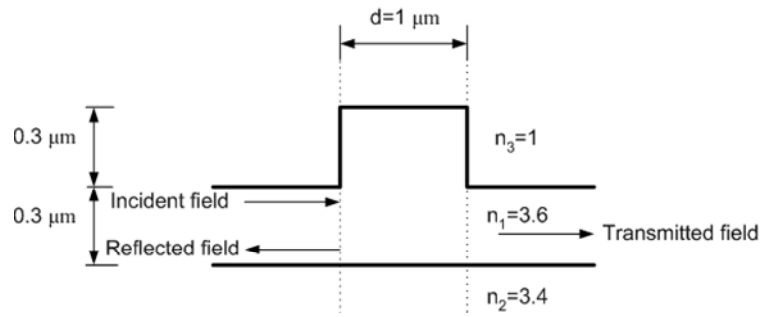
(a) Waveguide with Two Longitudinal Discontinuities
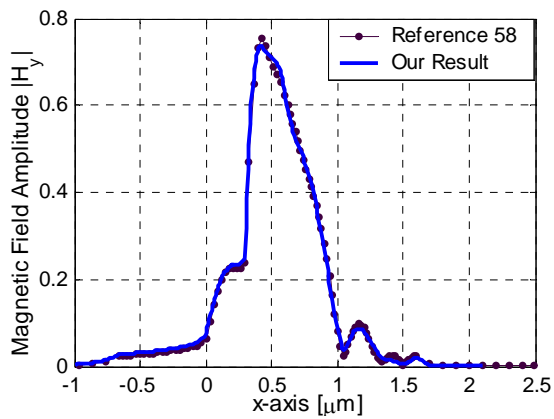
(b) Transmitted field
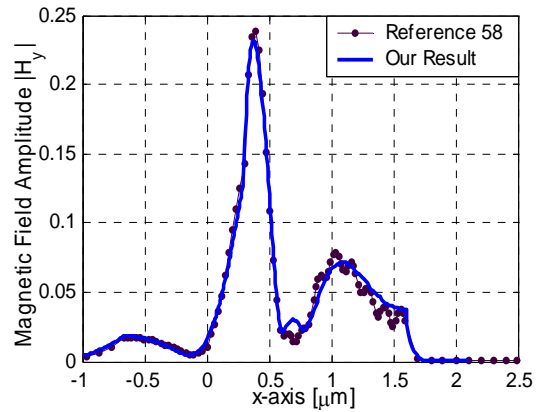
(c) Reflected field

Figure 4.4: Transmitted and Reflected Fields of a Double Discontinuity

Chapter 5

Analysis of Directional Coupler with two

Adjacent Waveguides

5.1 Introduction

In its simplest form, a directional coupler consists of two or more parallel dielectric waveguides in close proximity. This directional coupler configuration is known as the diffusion coupler.

When two parallel waveguides are in close proximity, the power coupling is based on the optical interference between the evanescent modal fields of the two waveguides.

Figure 5.1 shows a directional coupler with two parallel waveguides. If a light wave is launched into one of the waveguides, it is possible to couple the field power to the other waveguide almost completely [59].
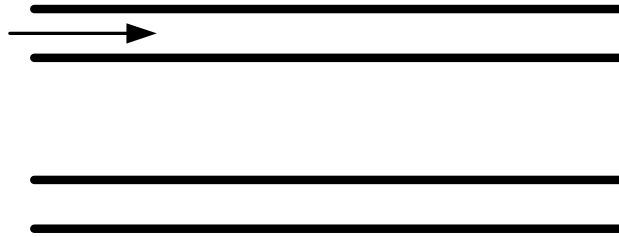
Figure 5.1: Simple directional coupler in parallel over a finite distance, the evanescent field from the primary wave**PORT 1**

In diffusion couplers, coupling occurs via the evanescent field that extends into the **BUS** substrate of an optical waveguide. When two single mode waveguides are placed builds up a secondary field in the secondary waveguide. The two waveguides are chosen to be single mode and identical for evanescent field coupling. If the waveguides are multimode or not identical, power coupling from one waveguide to another becomes very weak [60].

RECEIVER

5.2 Basic principles

PORT 4

If two parallel waveguides are placed sufficiently close to each other, the part of their evanescent fields must overlap spatially. Usually the inter-waveguide gap required for this

overlap to be significant is of the order of the waveguide width. When the two single mode waveguides are brought in close proximity to each other, the combined coupled structure supports two modes. One of these modes has an even transverse electric field variation, while the other is characterized by odd transverse field. The even and the odd modes of the coupled structure are shown in figure 5.2 (a) and (b). These modes are known to have almost similar values of effective index with the even mode having a slightly larger effective refractive index n_{eff} than that of the odd mode. The refractive index distribution of the twin waveguide system is also shown.

(a) Even TE_0 mode

(b) Odd TE_0 mode

(c) Refractive indices of the parallel symmetric waveguide
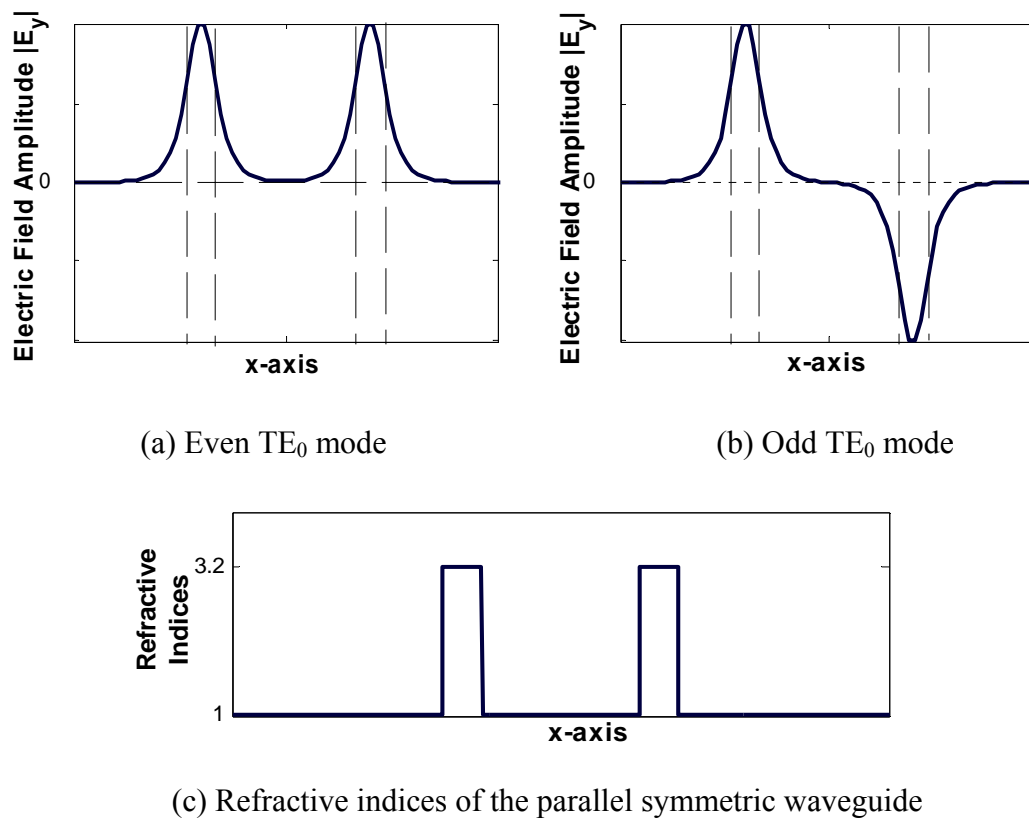
Figure 5.2: The overlap of the transverse fields and refractive indices of two adjacent, parallel symmetric slab waveguides

Because of inter-modal overlap; it is very hard to decide which guide the light in the overlap region actually belongs to. This implies that there must be a mechanism for light in one waveguide to be transferred to the other. It turns out that if the two waveguides satisfy a particular set of conditions and run parallel for sufficient distance, this interchange of power can be highly significant, reaching almost 100% in many cases. The light then start coupling back, so the power transfer process must be periodic with distance. We can present this power transfer between waveguides as shown in figure 5.3.
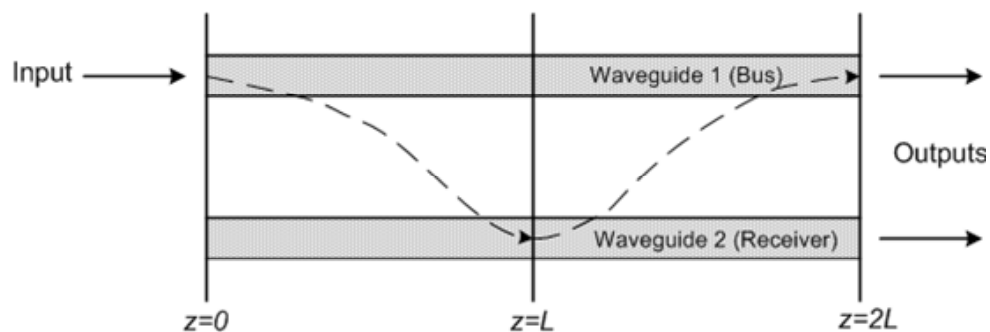
Figure 5.3: Conceptual representation of the coupling process

Here the input is applied to waveguide 1, at $z = 0$. We shall assume that complete coupling occurs at $z = L$ where all the light has been transferred to waveguide 2. At $z = 2L$, therefore, the light will have been completely coupled back to waveguide 1, and so on. In fact the process is continuous. The condition that the guides must satisfy for 100 per cent power transfer is therefore that they are synchronous (i.e. have the same propagation constant) so that all the scattered contributions add up in-phase. This usually requires them to be identical.

5.3 Method of Lines Analysis of Directional Couplers

The MOL algorithm has been programmed to analyze a simple directional coupler which consists of only two identical parallel dielectric waveguides in close proximity surrounded by air. To simulate the input of the device TE_0 mode of an isolated waveguide is used at the input. The input field used in the structure is shown in figure 5.4. This input configuration is used through out the thesis.
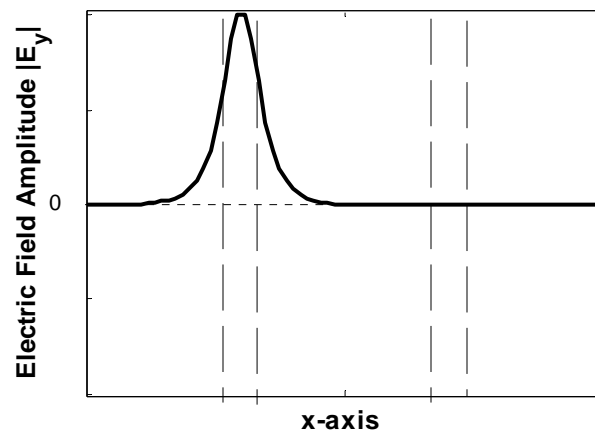
Figure 5.4: Electric Field Amplitude at the Input $(z = 0)$

5.3.1 Numerical Results for Add/Drop Filter with single Cavity

The directional coupler shown in Figure 5.1 has been simulated using the MOL as shown in figure 5.4. The top waveguide is referred to as the Bus and the bottom waveguide is referred to as the Receiver. The left side of the top waveguide is referred to as Port 1, the right side of the top waveguide as Port 2; the right side of bottom waveguide

as Port 3 and the left side of the bottom waveguide as port 4 for all cases. Each waveguide

core is assumed to be 0.2 μm wide and the distance between the two waveguides is set at

0.5 *μm*. Each waveguide core has a refractive index of 3.2. The surroundings material is

assumed to be air, with a refractive index of 1. The fundamental TE mode of an isolated

single waveguide at the wavelength of 1.55 *μm* is used to excite the upper waveguide

from port 1.
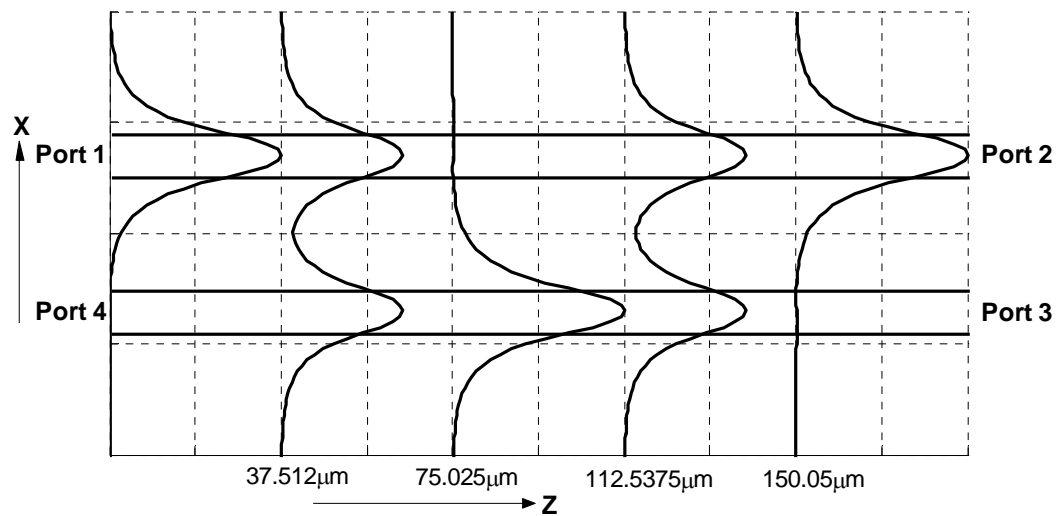
Figure 5.5: The TE$_0$ Mode at Different Points of Directional Coupler Calculated using the

Method of Lines

From the simulation results it can be seen that the field traveling through the bus is

coupled to the receiver completely after a distance 75.025 *μm*, and again coupled back to

the bus after the same distance.

Effects of waveguide separation:

For complete power transfer, the two waveguides have to be kept parallel for a certain distance. This length is known as the coupling length. The coupling length of a directional coupler can be theoretically calculated by:

$$L_c = \frac{\pi}{\Delta\beta} \qquad\qquad (5.1)$$

where $\Delta\beta$ is the difference of the propagation constant of the even and odd modes of the structure.

The distance between the waveguides is known as the separation. Figure 5.6 shows the effect of separation on the coupling length of the directional couple. The separation is varied from $0.1\mu m$ to $1\mu m$. As seen in figure 5.6, the coupling length increases with waveguide separation. The coupling length is found by calculating the phase constant of the TE_0 and the TE_1 modes of the coupled structure (namely β_0 and β_1) from which we can obtain $\Delta\beta$ by using $\Delta\beta = \beta_0 - \beta_1$. The coupling length is also calculated numerically by the MOL. The coupling length calculated numerically and theoretically are both shown in figure 5.6. The theoretical and the numerical results have exact match. This shows the correct implementation of the procedure.
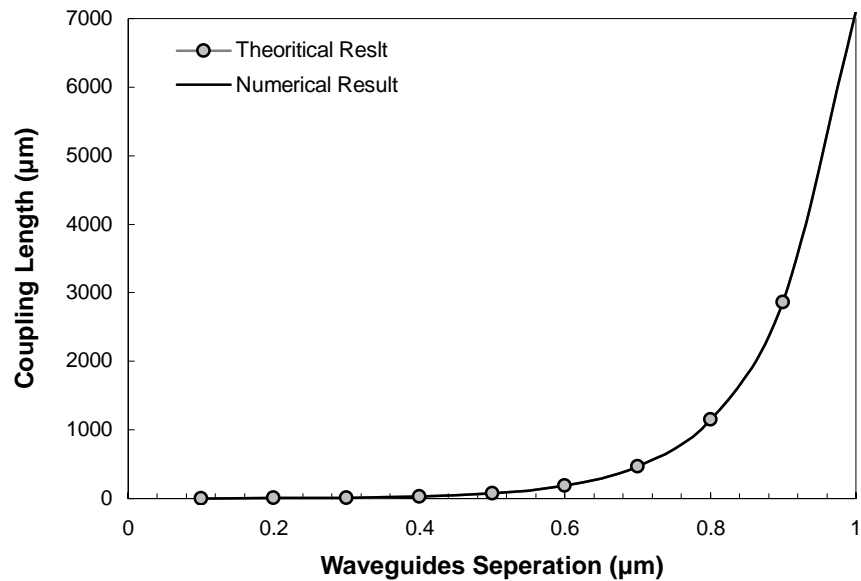
Figure 5.6: Coupling length at different waveguide separations

Wavelength Response of the directional coupler:

Wavelength has an effect on a directional coupler with fixed waveguide separations. Figure 5.7 shows the trasmissivities at port 2 and port 3 of the directional coupler for a range of wavelength from 1 μm to 1.7 μm. The separation between the waveguides is 0.5 μm and the length of the directional coupler is assumed to be 75 μm. Transmissivity at the bus port 2 drops to zero and the transmissivity at the receiver port 3 reach unity at $\lambda = 1.55$ μm. This implies a complete coupling between the waveguides at this wavelength. The coupling also occurs at higher wavelengths.

The wavelength response of this directional coupler is very broad. So it becomes unsuitable for marrow band operations.
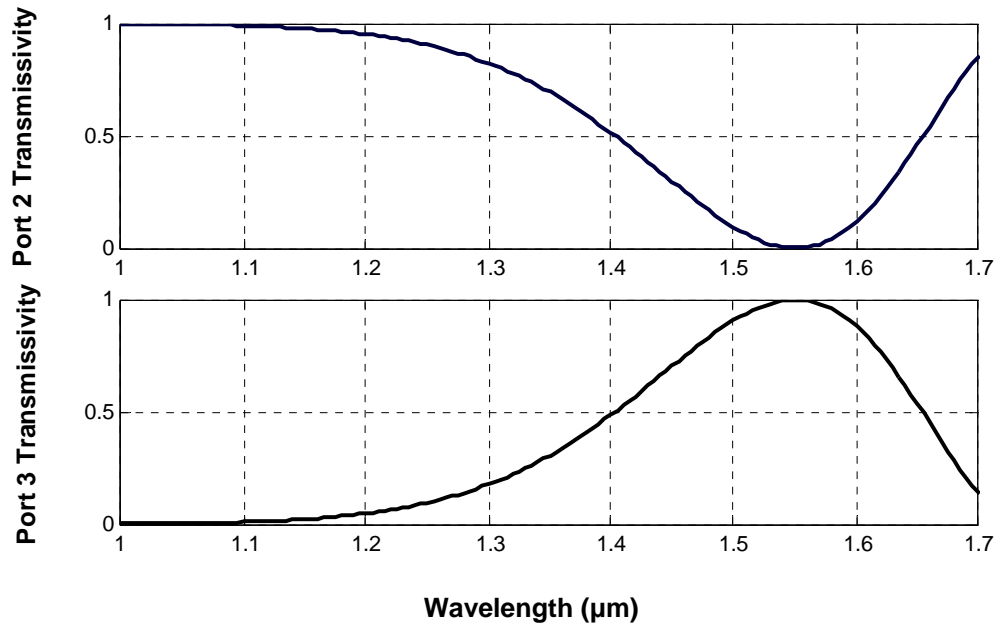
Figure 5.7: Trasmissivities at port 2 and port 3 of a directional coupler at different

wavelengths

Chapter 6

Analysis of Add/Drop Filter with A Square Cavity

6.1   Introduction

A filter which can be used to drop and add a certain wavelength from a group of wavelengths is referred to as an add-drop filter. The wide use of optical wavelength division multiplexing (WDM), calls for compact, convenient and narrow band channel add-drop filters. In this and the following chapters resonators of different sizes and shapes will be considered for channel dropping and adding devices. If the resonators are small enough so that the spacing of the resonant frequencies accommodates the set of WDM

channels within the communications window, the goal of dropping one channel by one filter without affecting the other channels is achieved.

Add/drop filters with resonant cavities of various shapes have been reported in the literature [62, 63, 64, 65, 66]. A device, which consist of a square cavity imbedded between two identical and parallel waveguides (see figure 6.1), acts as a channel add/drop filter as reported in [64, 65]. The most commonly reported cavity shape is the circular cavity [64] and the ring cavity [67].

In this chapter we analyze the operation of the add/drop filter with a square cavity using the MOL. Both the single and the multiple square cavity cases are treated.

6.2   Transmissivity and Reflectivity Calculations of Add/Drop Filter

Figure 6.1 shows an add/drop filter. The top waveguide is called the bus and the bottom waveguide is called the receiver waveguide. The modal transmissivity at the bus port 2 is referred to as T2, the modal transmissivity at the receiver port 3 as T3, the modal transmissivity at the receiver port 4 as T4 and the modal reflectivity at the bus port 1 as R1.

By using the modal orthogonally relationship in matrix form, the reflectivity R1 of port 1 of the directional coupler structure is calculated as:

$$R1 = \left| \frac{B_0' A_0}{A_0' A_0} \right|^2 \qquad (6.1)$$

and the transmissivities T2, T3, and T4 are calculated as:

$$T2 = \left| \frac{A_{N+1}' A_0}{A_0' A_0} \right|^2 \qquad (6.2)$$

$$T3 = \left| \frac{A_{N+1}' A_R}{A_R' A_R} \right|^2 \qquad (6.3)$$

$$T4 = \left| \frac{B_0 A_R}{A_R' A_R} \right|^2 \qquad (6.4)$$

here B_0 is the column vector containing the reflected fields in region 0 as shown in equation 4.24, A_0 is the column vector containing the input field (shown in figure 5.3 c), A_0' and B_0' are the transpose transposes A_0 and B_0 respectively. A_{N+1} is the column vector containing the transmitted field at the final layer as shown in equation 4.26 and A_R is a column vector containing a field similar to the input filed, but in this vector the peak value is at the center of the bottom waveguide (i.e. the receiver). The power radiated from the devise is termed as the fractional power radiated (FPR). In the thesis work FPR is calculated as:

$$FPR = 1 - (T2 + T3 + T4 + R1) \qquad (6.5)$$

For the directional coupler T4 and R1 will be zero. So

$$FPR = 1 - (T2 + T3) \qquad (5.6)$$

6.3 Add/Drop Filter with a Single Square Cavity

The basic implementations of the channel add/drop filter considered in this section is a four-port system that consists of a square resonator placed between two waveguides. A schematic is shown in Figure 6.1. The width of the resonator is d and the air gap between the waveguides and the cavity is g. The fundamental mode of the isolated waveguide is used as the input at port 1 of the add/drop filter. The resonator is evanescently coupled to the bus and the receiver. In general, the resonator modes interact with the forward and backward propagating modes of the waveguides over a finite length.

When an optical signal is propagated from port 1 (see figure 6.1), for a certain cavity dimension, the square cavity resonates at a certain wavelength and a fraction of the optical power is dropped to the receiver ports 3 and 4. A fraction of power is also reflected back to port 1 of the bus.
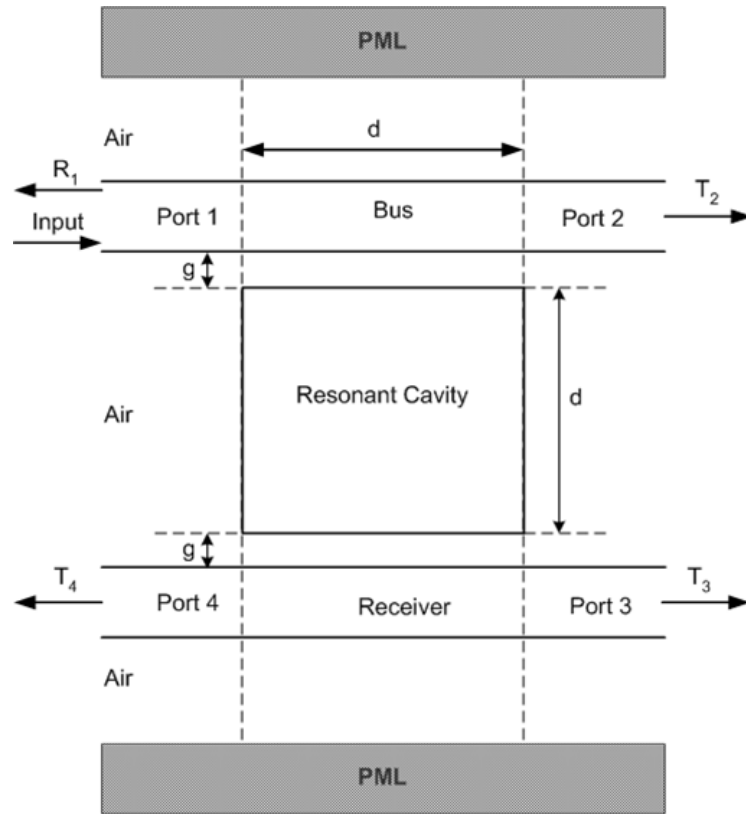
Figure 6.1: Add/Drop Filter with an Imbedded Square Cavity between two Parallel

Waveguides

6.3.1 Numerical Results for Add/Drop Filter with single Cavity

An add/drop filter with a square imbedded cavity has been simulated. The waveguides and the cavity have a refractive index of 3.2. The surrounding media is air with a refractive index of 1. Both waveguide cores widths are 0.2 μm. A PML layer of tangent loss profile is used at both ends of the computational window to prevent reflections from the electric walls. The Layer by layer approach is used to calculate the modal transmissivities T2, T3 and T4 and modal reflectivity R1 of the four ports. The mesh size

along x-axis is taken as 2.5 *nm*. The air gap widths g, between the cavity and the waveguides are identical and are each 0.28 *μm* in width. The square cavity width d is 1.54 *μm*. The waveguide and the cavity dimensions are taken from reference [67].

Figure 6.2 shows the filter responses of the four ports R1, T2, T3 and T4 for wavelength range 1.524 *μm* to 1.54 *μm*. The results show clear wavelength selectivity of the filter at the resonance wavelength $\lambda \approx 1.532 \mu m$. At the resonant wavelength part of the energy is dropped from the upper waveguide into the lower waveguide. The transmissivity at the bus port 2, T2 drops from unity to 0.369 at the resonance wavelength. At resonance, the reflectivity R1 increases to 0.164 and the transmissivity at the receiver ports T3 and T4 increase to 0.165 and 0.168 respectively. The fraction of power radiated FPR reaches a maximum value of 0.133 at resonance.
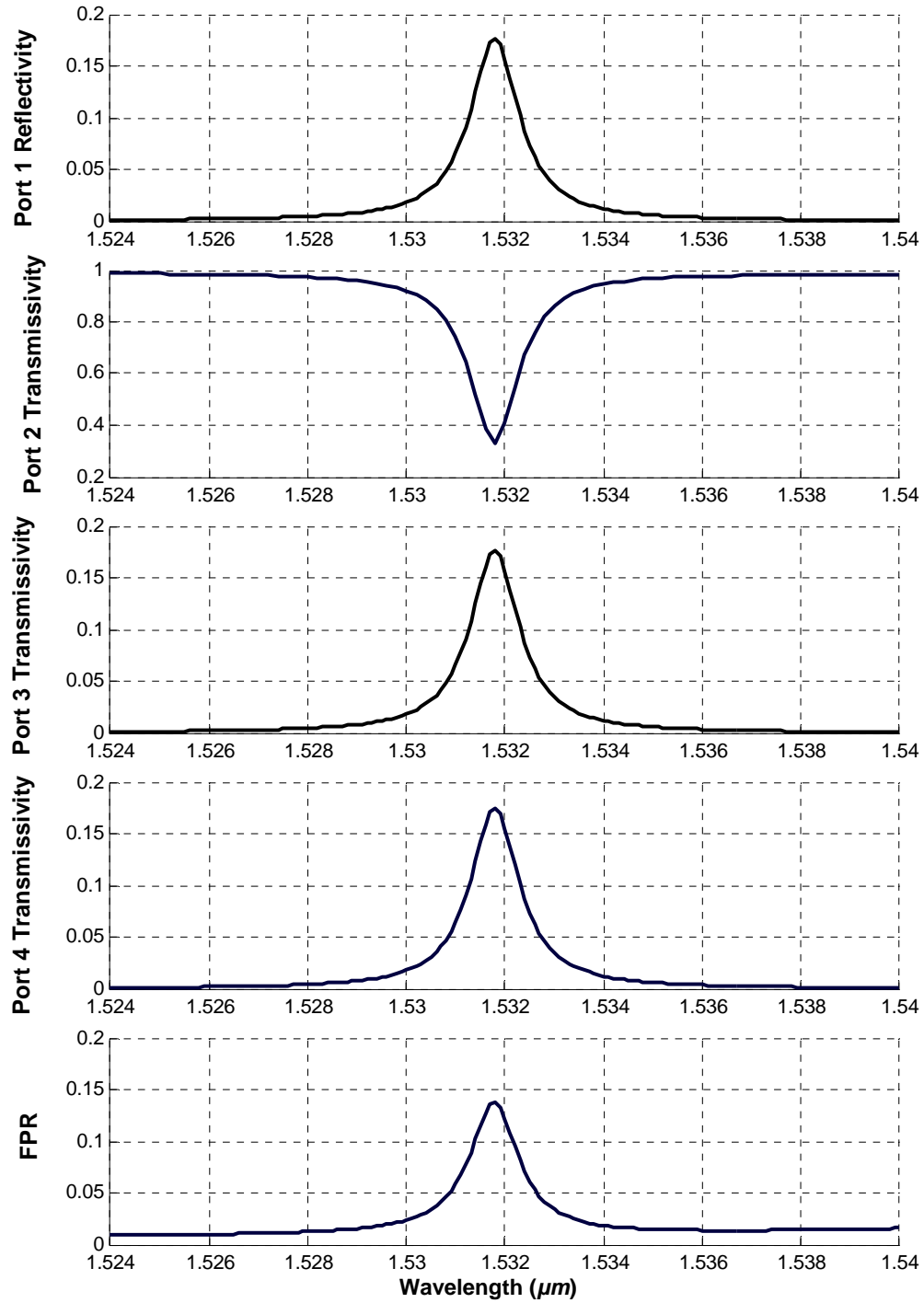
Figure 6.2: Response of the Add/drop the Filter with Single Cavity

(Cavity Width d = 1.54 *μm* and Air Gap Width g = 0.28 *μm)*

Figure 6.3 shows an image of the field intensity distribution in the add/drop filter at the resonant wavelength. The sanding waves inside the cavity are clearly visible in the image. The field intensity inside the cavity is higher than the field intensity in the waveguide. This phenomenon is known as Field Intensity Enhancement (FIE). The field intensity enhancement factor inside the cavity is 5.32. This means that the maximum field intensity inside the cavity is 5.32 times the maximum field intensity of the input field. The electric field intensity enhancement is due to the standing wave pattern, it does not imply that there is an overall increase in the power inside the cavity.
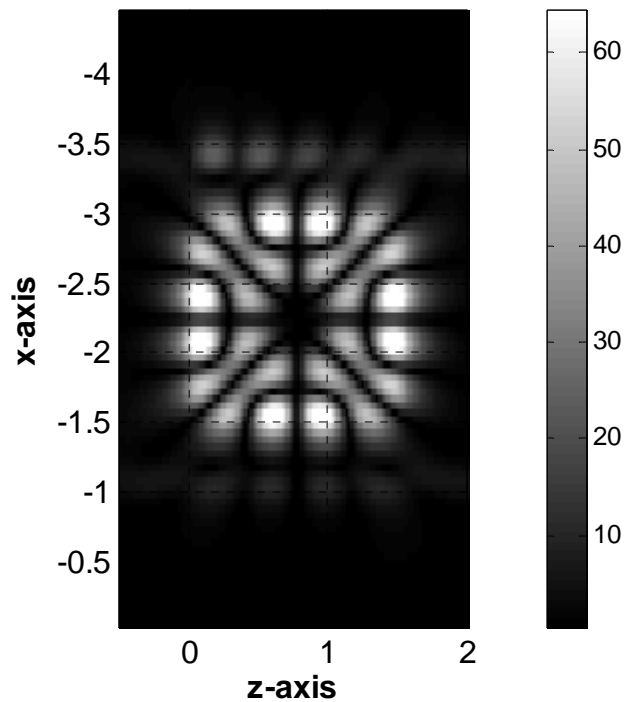
Figure 6.3: Add/Drop Filter with single cavity modal response

The drop efficiency of the Add/drop filter may be improved by use of different cavity sizes and air gap widths.

Effect of the Air Gap Width:

Figure 6.5 shows the filter response of the four ports of an Add/Drop filter for different widths g of the air gap. The cavity width is kept 1.54 μm. It can be seen from the figure that as the air gap is reduced:

    I. The resonance shifts towards lower wavelength,

   II. The spectral width increases,

  III. T2 drops T3 and T4 increases. This indicates that the power coupling from the bus to the receiver increases.

  IV. R1 increases and FPR decrease up to a certain limit.
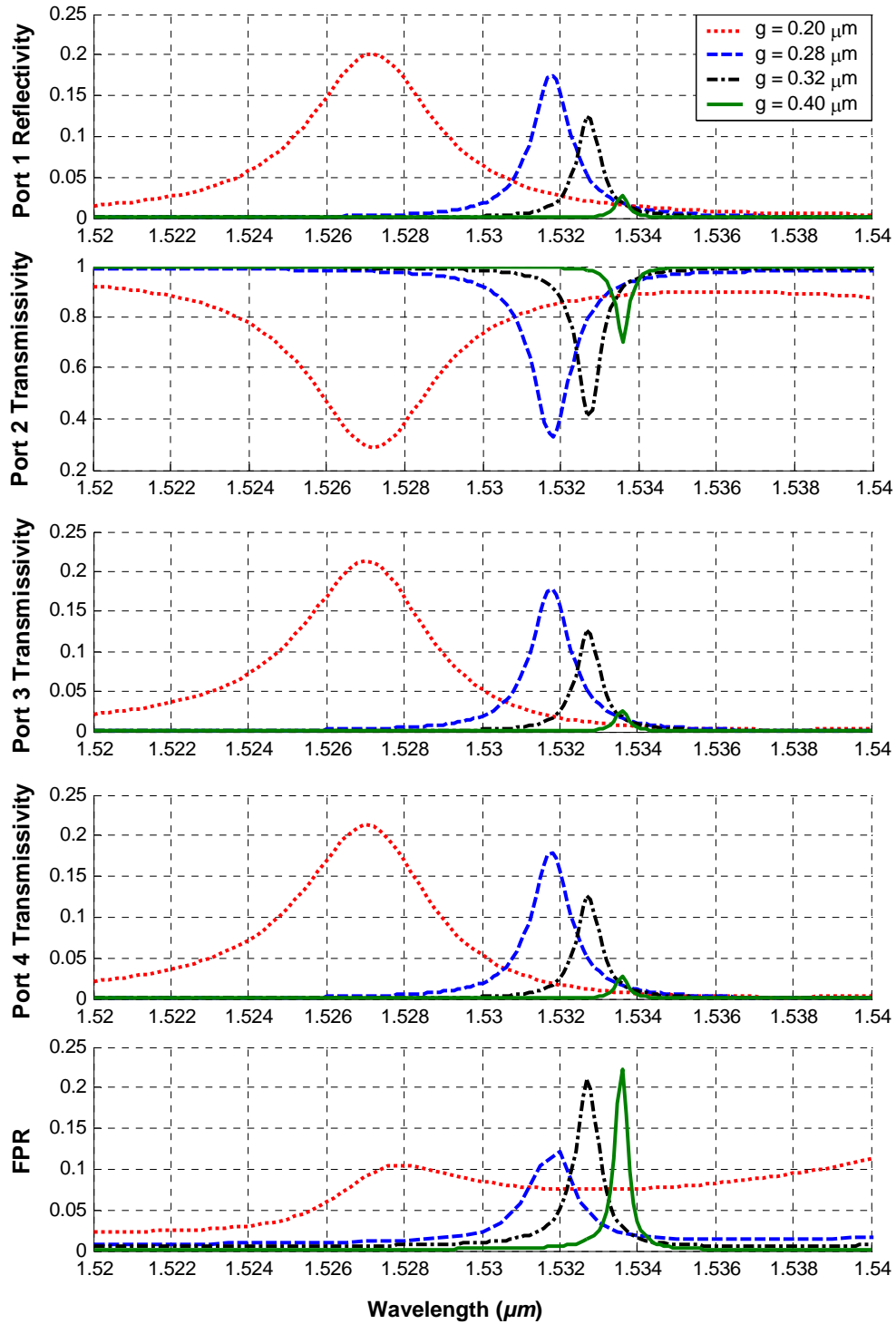
Figure 6.4: Filter Response of the Add/Drop Filter with Single Cavity for different Air

Gaps Widths

Effects of the square cavity width:

In this section we consider the effect of the square cavity width for a fixed air gap width g = 0.28 μm. Figure 6.5 shows the response of the four ports of the add/drop filter for different cavity width d = 1.50 μm, 1.54 μm and 1.58 μm. As the cavity width is increased the following occur:

  I. Resonance shifts towards higher wavelength.

 II. T2 decreases while T3 and T4 increase. This indicates that the coupling between the bus and receiver increases in this case.

III. R1 increases.

    From the numerical results for the add/drop filter with a single square cavity, it can be observed that T3 ≈ T4, which means the drop at the receiver waveguide is not biased towards a particular port. Moreover, R1 is almost equal to T3 and T4. That is, although the drop performance improves by increasing cavity width, the modal reflectivity R1 at the bus becomes higher. A large modal reflectivity R1 is not desirable, because it may cause signal distortion and may interfere with the operation of the light source. In addition, a large value of R1 reduces the filter efficiency. It can be concluded that the overall drop performance of the present filter is poor.
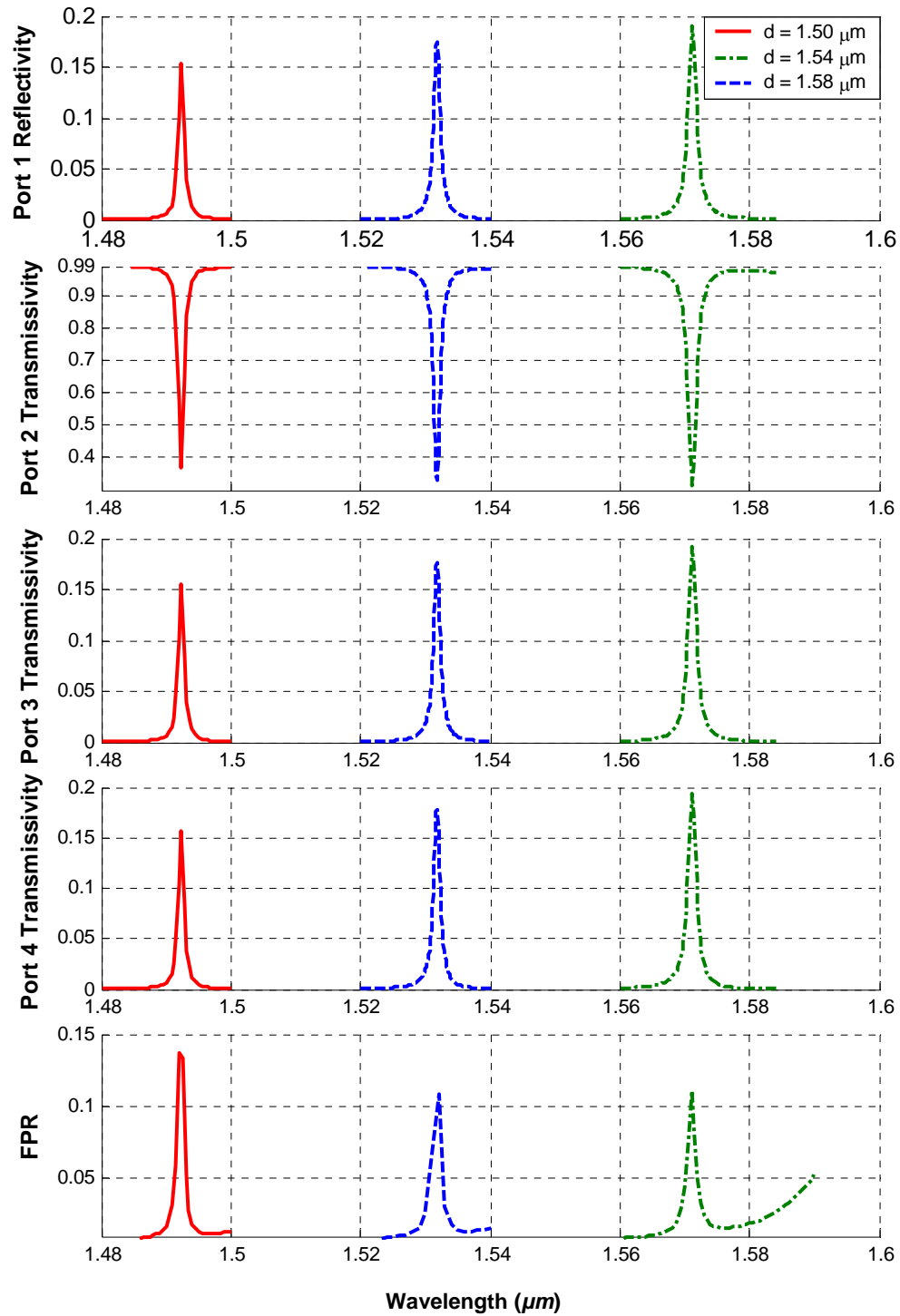
Figure 6.5: Response of an Add/Drop Filter with Single Cavity at different cavity sizes

At its best, half the input power at the resonant wavelength remains in the bus and is equally distributed into ports 1 and 2 while the other half, reduced by a fraction due to loss is equally distributed into ports 3 and 4 of the receiver [67].

6.4 Add/Drop Filter with Two Square Cavities

To achieve better filtering efficiency an add/drop filter with two symmetrical square cavities has been simulated as shown in Figure 6.6. The Square cavities of refractive index 3.2 are imbedded between two waveguides of the same refractive index. The surroundings of the waveguides and the cavities had a refractive index 1. Similar to the add/drop filter simulations Layer by layer approach is used to calculate the modal transmissivities and reflectivity of the four ports. The only difference is that there are extra layers in the z-axis to simulate the second cavity. The mesh size along x-axis is taken as 2.5 *nm* for accurate response. The air gap between the waveguide and the cavity is g and the separation between the cavities is s.
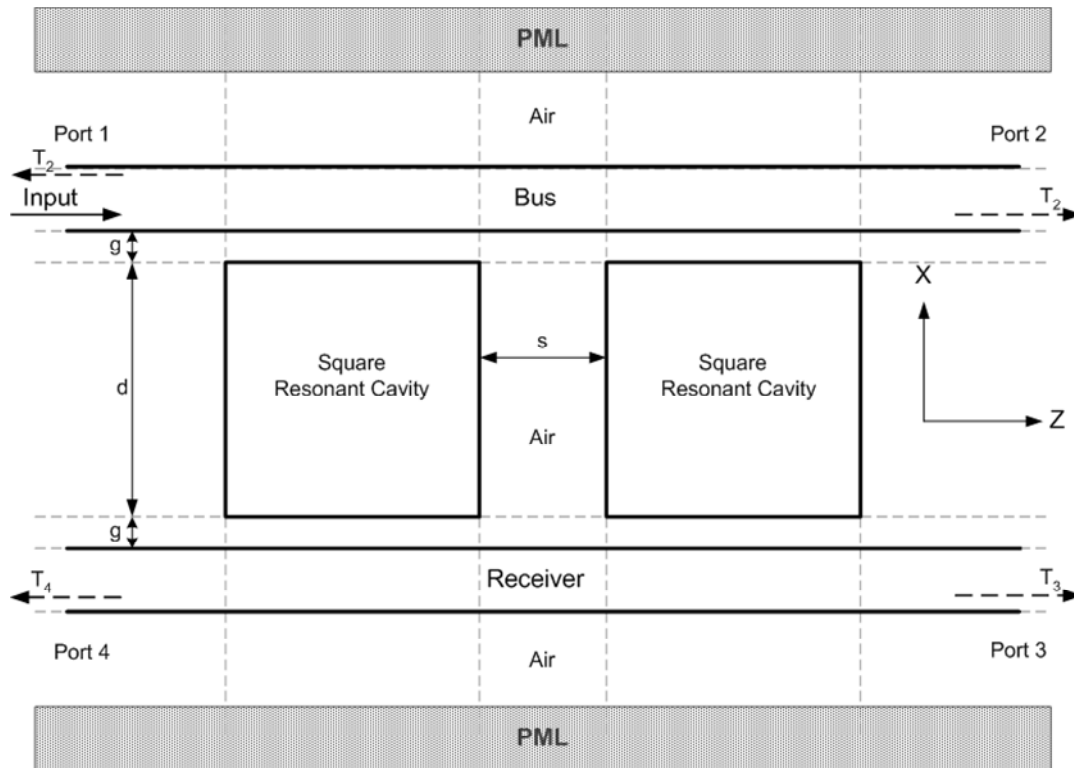
Figure 6.6: Representation of an Add/Drop Filter with two cavities in regions for MOL

simulations

6.4.1 Numerical Results for Add/Drop filter with Two Square

Cavities

An add/drop filter with two square cavities in the horizontal direction (see figure 6.6) has

been simulated using the MOL and the layer by layer algorithm. The results that will be

presented show better response than that with a single square cavity.

Figure 6.7 shows the modal response of the filter with two square cavities. With two

identical square cavities each having a width of 1.54 μm, air gap width g = 0.28 μm,

separated by s = 0.715 *µm*, the resonance wavelength is 1.532 *µm*. With two identical cavities, the transmissivity at port 3 increases dramatically due to the constructive interference between the cavities resonances. This shows a significant increase in coupling at a single receiver port (T3>T4) as suggested in [67]. T3 increase to 0.65 and T2 decreases to 0.05. T4 and T1 drop down to 0.01. T4 and T1 are 0.105 at wavelength 1.5315 *µm*, and 0.06 at wavelength 1.5325 *µm*. The FPR is 0.29 at the resonant wavelength.
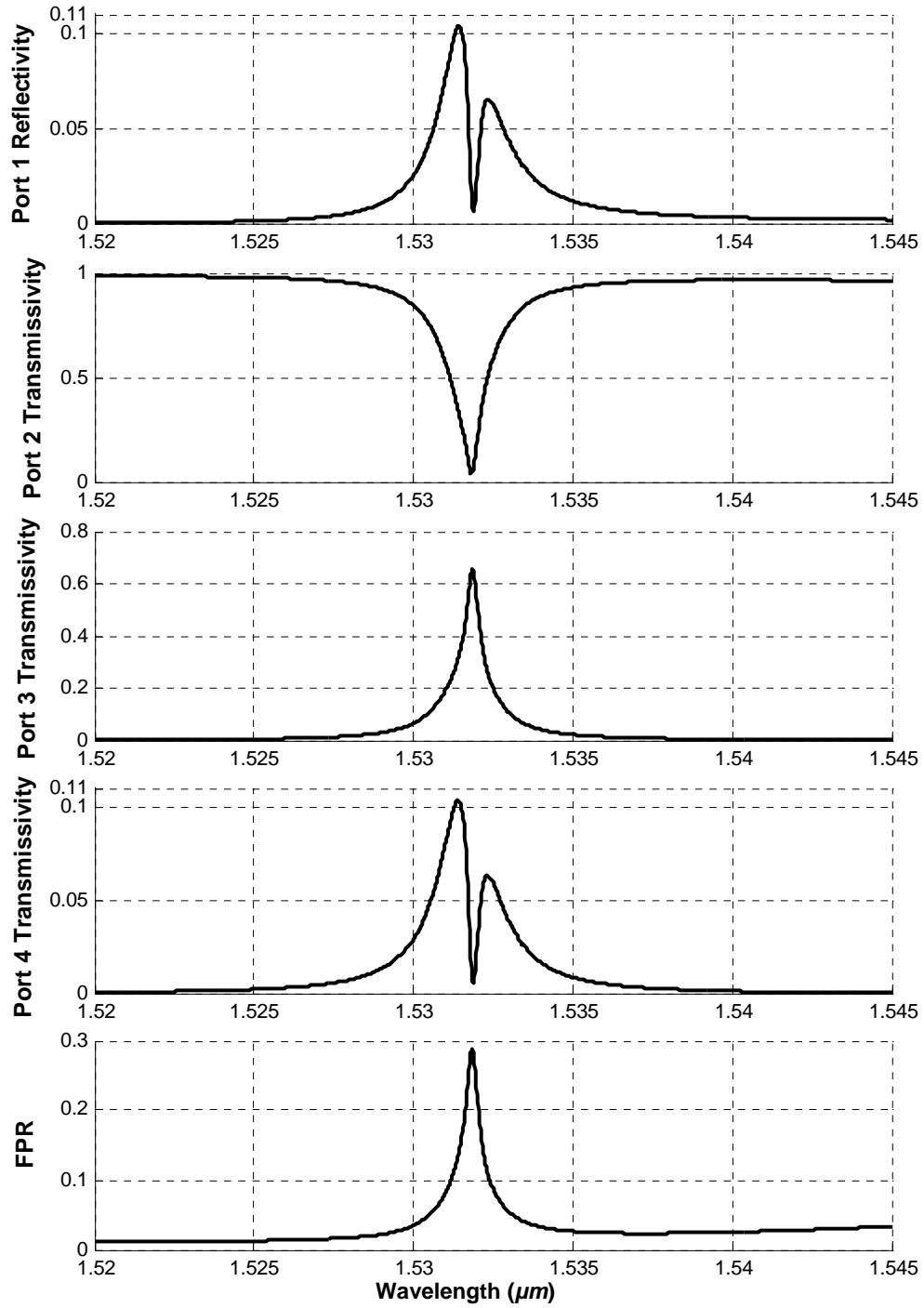
Figure 6.7: Response of the Add/Drop Filter with two Square Cavities

(Cavity Width d = 1.54 *μm*, Air Gap Width g = 0.28 *μm*, Cavity Separation s = 0.715 *μm*)

Figure 6.8 shows an image of the field intensity at the resonant wavelength $\lambda = 1.5318$ μm. A field intensity enhancement similar to add/drop filter with a single cavity is seen also here. The first cavity has higher a FIE than that seen in the second cavity.

The responses of the ports vary with the variation of cavity width d and air gap width g.
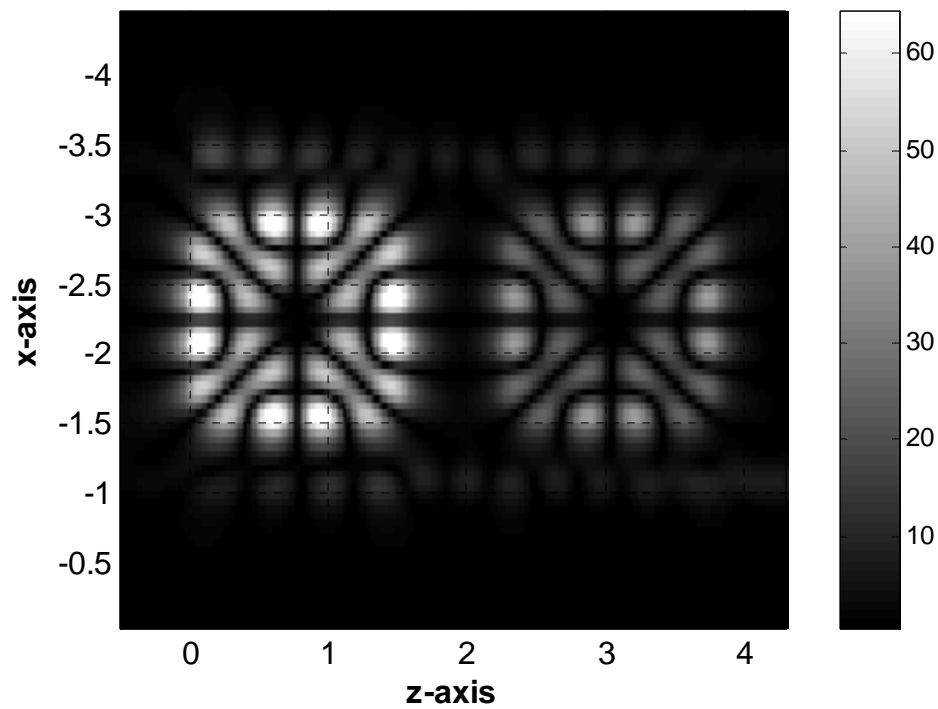
Figure 6.8: Add/Drop Filter with single cavity modal response

Effect of the Cavity Separations:

Cavity separation has a strong effect on the filter response. For a given square cavity width d, air gap width g, cavity separation s, the transmissivity at port 3 is maximized at resonance due to constructive interference. Figure 6.9 shows such a case for the cavity width d = 1.54 μm and air gap width g = 0.28 μm. In this case at the wavelength of 1.5318 μm when the cavity separation s is varied the following occurs:

I. As the cavity separation s increases the T2 decreases and T3 increases.

II. When s = 0.715 μm, maximum power is coupled at the receiver port 3. T3 increases to 0.65 and T2 decreases to 0.05. T4 and T1 drop down to 0.01. T4 and T1 are 0. The FPR is 0.29 at the resonant wavelength.

III. When s is grater than 0.715 μm coupling decreases and

IV. T4 and R1 have maximum values at s = 0.933 μm.

V. PFR have maximum value 0.30 at s = 0.702 μm.

The filter performance of the add/drop filter with two square cavities is better than add/drop filter with a single cavity as the transmissivity at receiver port 3; T3 is maximized at resonance due to constructive interference.
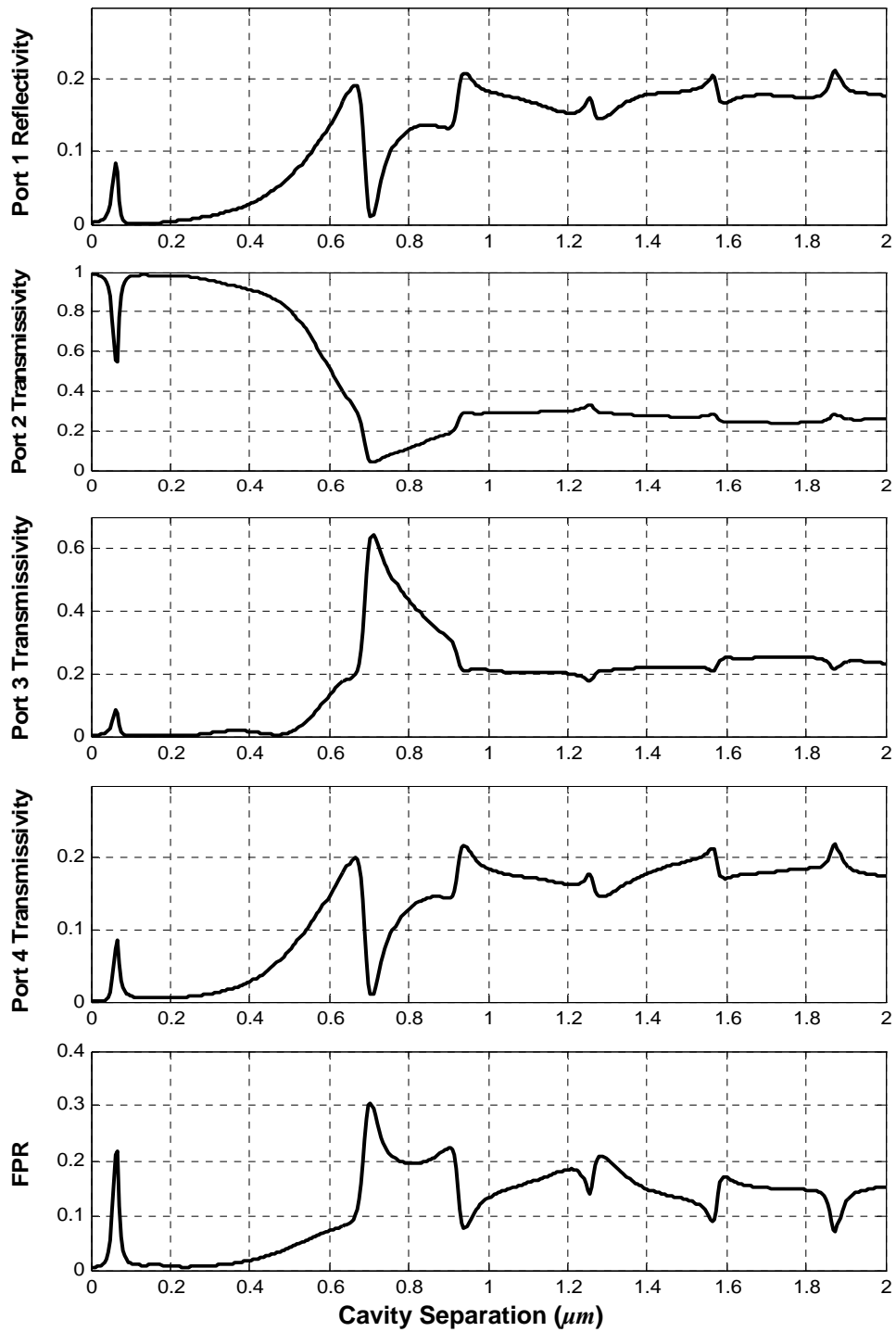
Figure 6.9: Response of the Add/Drop Filter with Two Square Cavities for different cavity

separations at $\lambda = 1.5318\ \mu m$. (Cavity width d = 1.54 μm, air gap width g = 0.28 μm)

6.5 Add/Drop Filter with Three Square Cavities

An add/drop filter with three identical square cavities has been simulated as shown in Figure 6.10. The Square cavities of refractive index 3.2 are imbedded between two waveguides of the same refractive index. The surroundings of the waveguides and the cavities had a refractive index 1. The air gap between the waveguide is the cavity is g. The two cavity separations are identical.
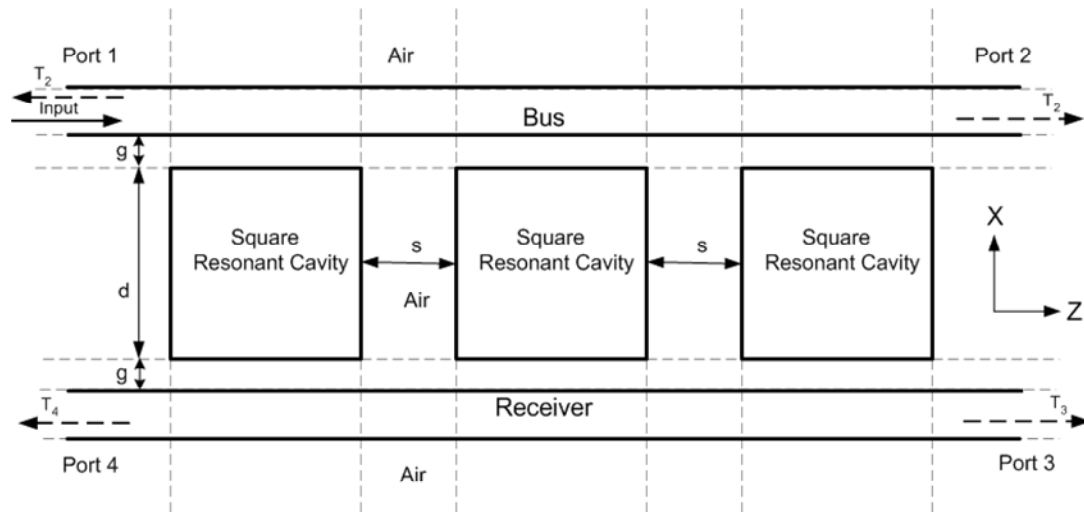
Figure 6.10: Representation of an Add/Drop Filter with three cavities in regions for MOL simulations

6.5.1 Numerical Results for Add/Drop filter with Three Square Cavities

Figure 6.11 shows the comparison of the responses of the add/drop filters with two and three identical square cavities. The cavity width is fixed at d = 1.54 μm each, the air gap

width is g = 0.28 *μm* and cavity separations is s = 0.715 *μm*. With three cavities constructive interference does not occur. Instead of a single resonant wavelength the add/drop filters with three cavities resonates at two wavelengths very close to each other causing wider bandwidth. At these resonance wavelengths T2 reaches minimum values and T3 reaches maximum values. T2 of these resonant wavelengths are not as small as the T2 response of the add/drop filter with two square cavities. Similarly at the resonance wavelengths the values of T3 peaks of the add/drop filters with three cavities are not as high as that of the add/drop filters with two cavities.

For add/drop filter with three square cavities in the horizontal direction, the constructive interference does not occur. This causes poorer filter response when compared to add/drop filter with two cavities.
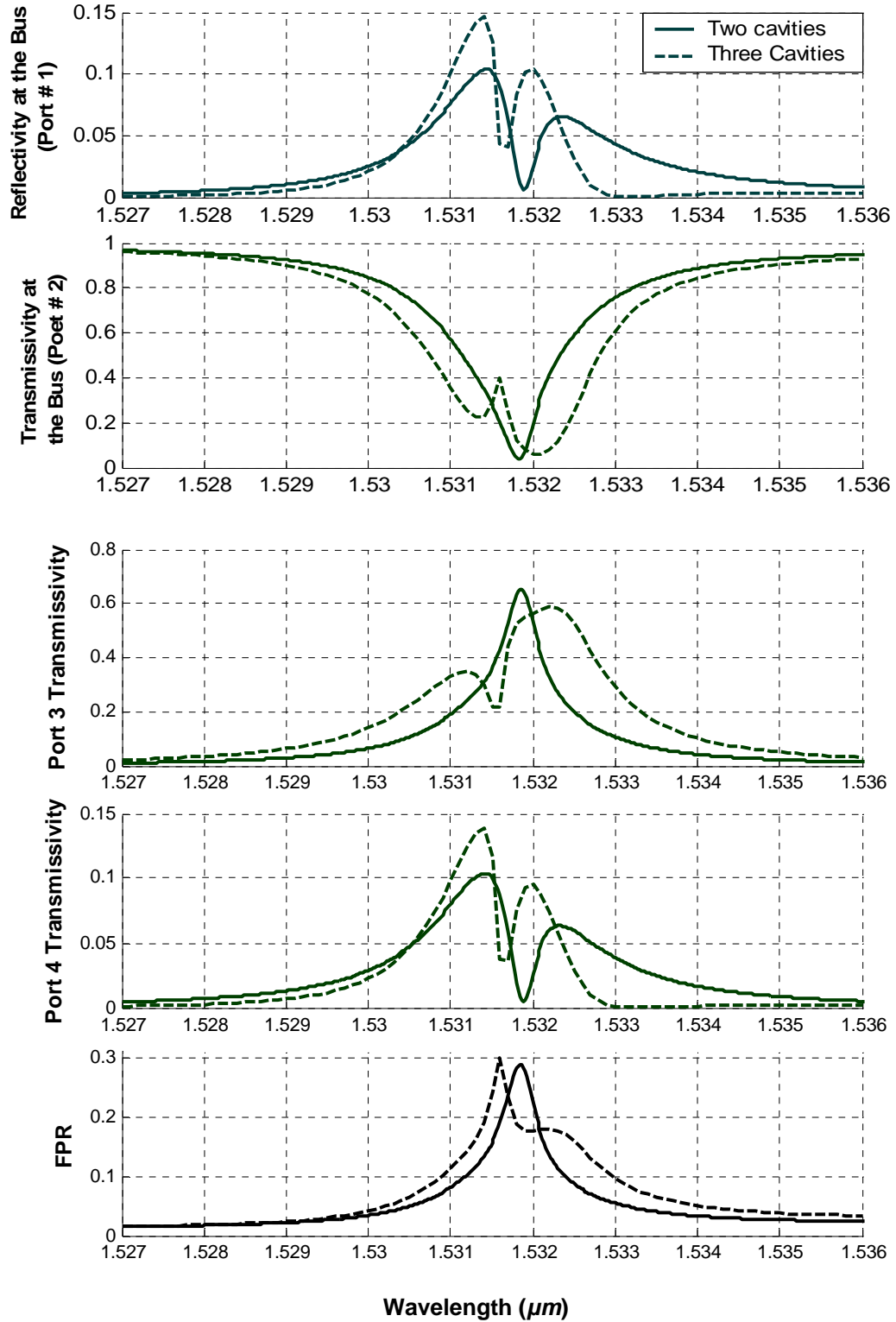
Figure 6.11: Comparison between add/drop filters with two and three Cavities. (Cavity

Dimension 1.54 μm, g = 0.28 μm and s = 0.715 μm)

Chapter 7

Analysis of Add/Drop Filters with Circular and Elliptical Cavities

7.1 Introduction

Circular resonators are known as versatile elements in photonics with various applications. They are also known as Circular Whispering-Gallery Mode (WGM) Resonators. The term whispering-gallery mode describes the electromagnetic wave that circulates around the inner surface of a dielectric sphere or cylinder as a result of total internal reflection [69]. With size flexibility, mechanical stability and adaptability to integrated circuits WGM resonators are widely used for basic research and in various applications [70–80].

In the optical range, the WGM resonator is usually a dielectric cylinder [72–78]. It guarantees the building up of the electromagnetic field of a certain wavelength, which is very important in the applications of wavelength selection [72], spectroscopy [73], nonlinear optics [74] and the microlaser cavity [75]. At telecommunication wavelengths, similar micro ring resonators have been reported for wavelength filtering and modulation [77].

In this chapter, the MOL is used to simulate as add/drop filter with a circular and an elliptical cavities. The numerical results are then discussed.

7.2 Basic principles

A WGM resonator is usually excited by the external evanescent fields of a coupler, which can be a dielectric prism [72, 73], an optical fiber [75, 78], a microstrip transmission line [79] or a dielectric waveguide [80]. When the electromagnetic wave of the coupler passes through the coupler–resonator contact region, part of the field is coupled into the resonator and propagates around its inner surface. In the case of a continuous wave (cw) coupling source a set of discrete wavelengths give rise to constructive interference. These resonant wavelengths are determined by the dimensions, the coupling condition of the dielectric resonator and the polarization of the coupling source.

7.3   Filter Response Calculations using the MOL

As shown in Figure 7.1, a circular cavity of refractive index 3.2 is imbedded between two waveguides of the same refractive index. The surroundings material is assumed to be air, with a refractive index of unity. PML layers having a tangent loss profile are used to prevent reflections from the electric walls of the computational window.
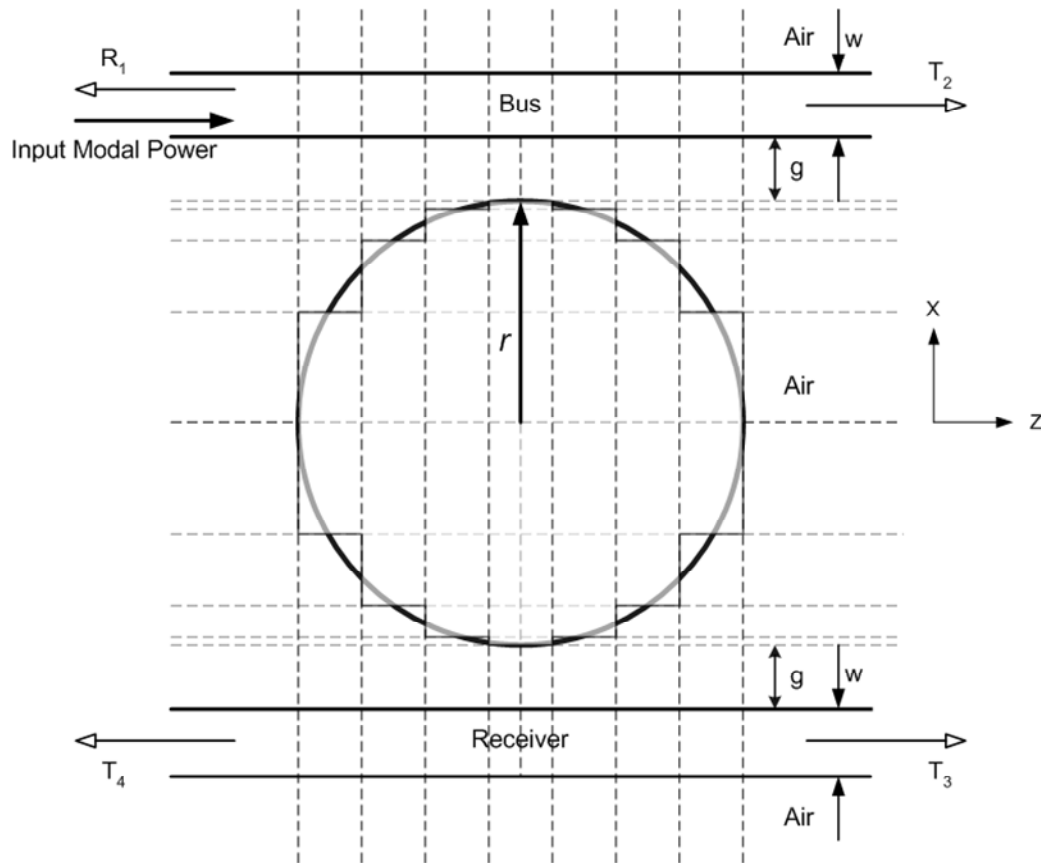
Figure 7.1: Add/Drop Filter with a circular cavity

7.3.1 Convergence of MOL for Circular Cavity

The Staircase approximation is used to simulate the circular cavity as shown in figure 7.1. The computational window is discretized in regions along the x-axis with an appropriate number of layers in the z direction. The filter response is then calculated using the layer by layer approach.

Two approaches were used to approximate the circular cavity, using a uniform layer width and a nonuniform layer width. With the first approach uniform layer widths along x-axis and z-axis were used to approximate the circle. Using this approach, a large number of layers are required for the structure to converge which in turn requires a large computational time and memory. The second approach is based on a nonuniform layer width. The second approach is used throughout the thesis because it requires less number of layers which is more time and memory efficient than the fist approach. The total number of layers along the x-axis and the number of layers in z-axis are equal. The layer width along the z-axis is uniform for all layers. The nonuniform layer widths along x-axis are calculated from the equation of a circle as shown below:

$$x^2 + z^2 = r^2 \qquad (7.1)$$

where r is the radius of the circle whose centre is at 0,0. From equation 7.1 we can write:

$$x_i = \sqrt{r^2 - z_i^2} \qquad (7.2)$$

here $i = 1, 2, 3, \ldots, n$; n = number of layers along z-axis. Distance of each layer from the centre of the circle can be calculated from equation 7.2. The width of each layer along the x-axis can then be calculated by taking the difference $x_{i+1} - x_i$.

This results in a nonuniform layer width along the x-axis. The layer widths are small at the top and bottom boundary (along x-axis) of the circle and gradually increase towards the center of the circular cavity (See figure 7.1).

Figure 7.2 shows the modal transmissivities of port 2 and 4 versus the number of layers used to approximate the circular cavity along the z-axis. The curves show that beyond 50 layers the value of T2 and T4 remain unchanged with further increase in number of layers. This indicates that the structure simulated converges to a circle. In the thesis work, a total of 60 layers were used throughout to simulate the circular cavity.
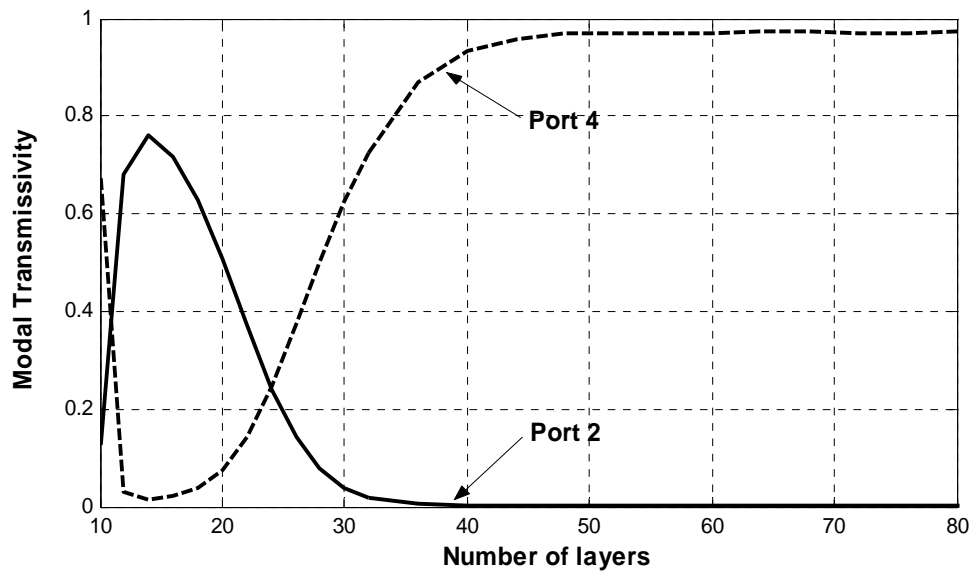
Figure 7.2: T2 and T4 versus Number of Layers

7.3.2 Numerical Results for the Add/Drop Filter with Circular cavity

Figure 7.3 shows the filter response of an add/drop filter with bus and receiver waveguides of .2 μm and a circular cavity of radius of 0.85 μm for a range of wavelength. The air gap between the waveguides and the cavity has a width g = 0.15 μm. These dimensions are selected so that the cavity resonates at λ = 1.55 μm where the drop and add to ports 2 and 4 respectively, are maximized. The input port is excited using the fundamental TE mode of the isolated waveguide. The curves show that at λ = 1.55 μm, the circular cavity resonates and all the power input at Port 1 is coupled clockwise to port 4 by the whispering-gallery mode (WGM). The following are observed from the curves:

I. At the resonant wavelength (λ = 1.55 μm) T2 reduces zero and T4 reaches a peak value of 0.978.

II. T3 and R1 are very small at the resonant wavelength and have maximum values at λ = 1.564 μm. The maximum values of T3 and R1 at wavelength 1.564 μm are 0.0028 and 0.0033, respectively. The values of T3 and R1 are very small in the wavelength range of figure 7.3.

III. At the resonant wavelength the FPR equals 0.025. The FPR reaches to a maximum value of 0.13 at λ = 1.564 μm.

IV. The 3dB spectral width is 5 nm.
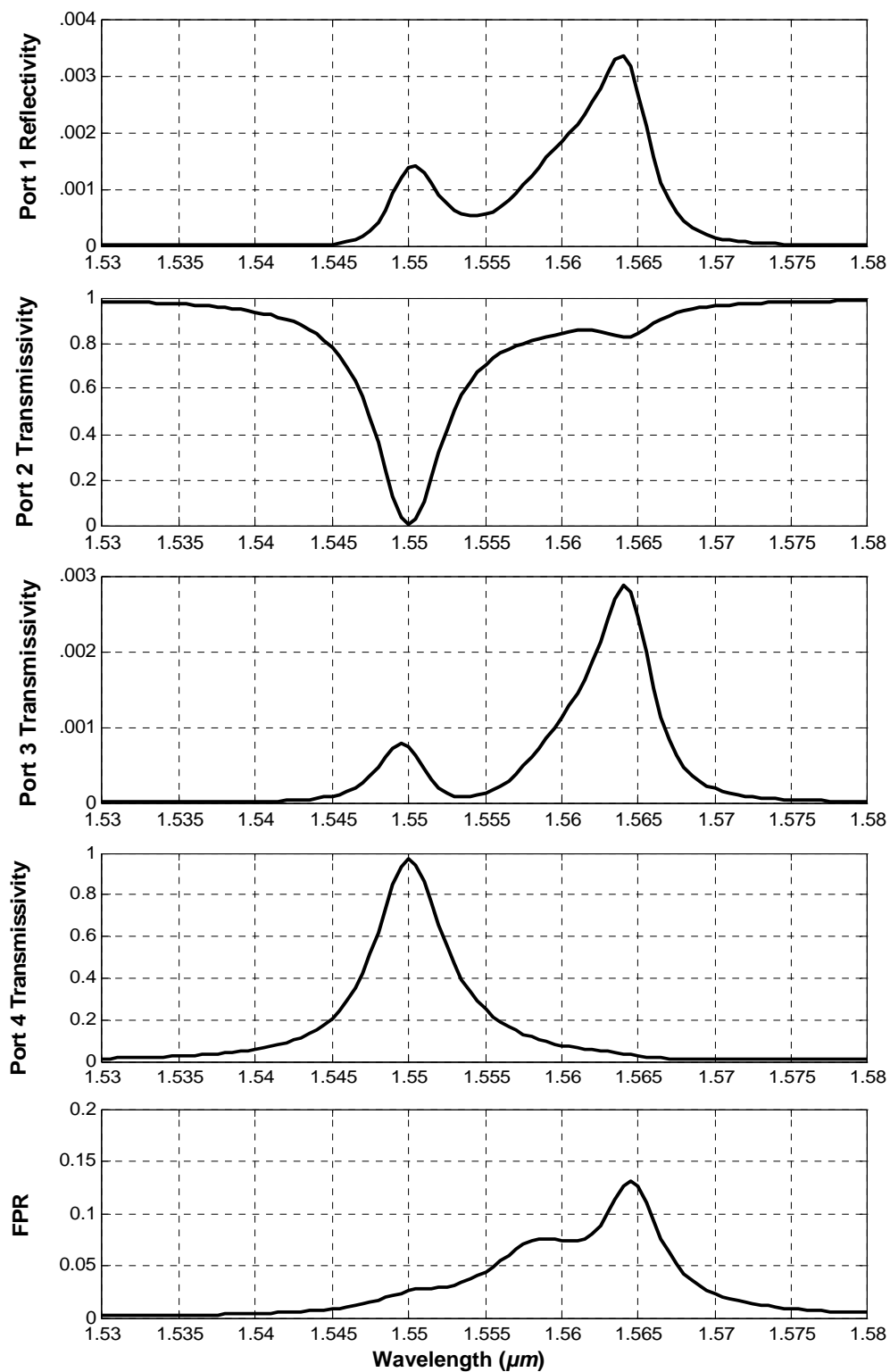
Figure 7.3: Response of an Add/Drop Filter with Circular Cavity

(Radius r = 0.85 *μm*, Air Gap Width g = 0.15 *μm*)

The over all filer response of the add/drop filter with circular cavity is better than the add/drop filter with the single and double square cavities. Next, we will consider the effects of the various parameters on the performance of the add/drop filter.

Effects of Circular Cavity Radius:

By fixing all parameters, including the operating wavelength, the effect of the cavity radius is examined. The cavity is seen to resonate at certain cavity radius (see figure 7.4) and coupling between the bus and the receiver waveguides increases at higher resonances. The air gap width g is fixed to 0.15 μm and wavelength $\lambda = 1.55$ μm. As the cavity size is varied the followings are observed from the curves:

I. At $\lambda = 1.55$ μm, the circular cavity resonates at several values of radii.

II. When the cavity size is small, T4 is very small at resonance radii. As the cavity size increases T4 at resonance increases reaching a maximum value of 0.978 at $r_x = 0.85$ μm. T4 at resonance radii reduce gradually after $r_x = 0.85$ μm.

III. R1 and T3 at resonance drop with increasing cavity radius. However, both R1 and T3 remain small in the entire range of figure 7.4.

IV. The power loss to radiation as indicated by the FPR is about 0.08 at $r_x = 0.85$ μm μm and it is large at resonance radii lower or higher than $r_x = 0.85$ μm.

It can be concluded that with g = 0.15 μm, the circular cavity with radius r = 0.85 μm, has the best filtering performance at the resonant wavelength $\lambda = 1.55$ μm.
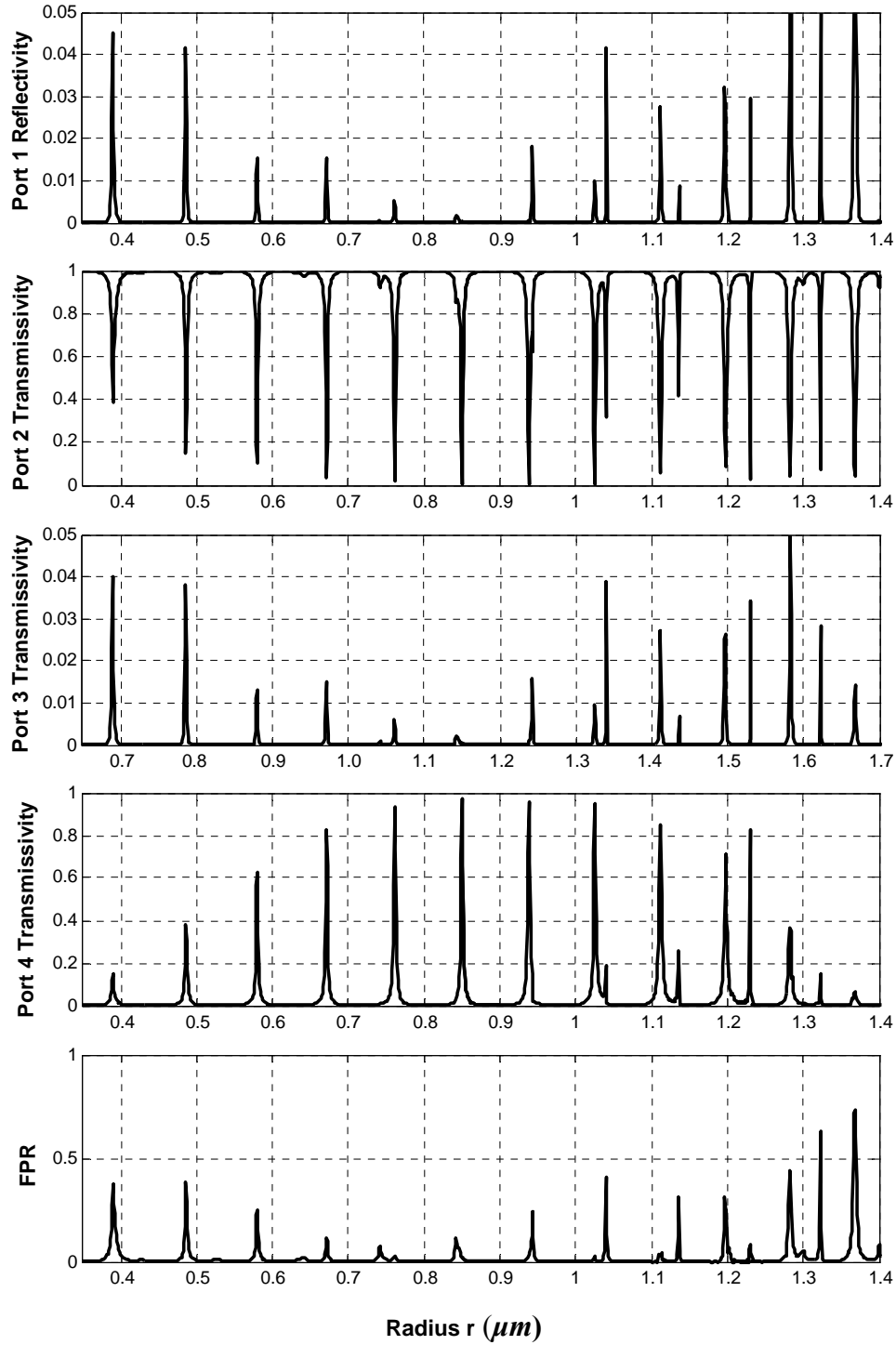
Figure 7.4: Filter Responses of Add/Drop Filters with Circular Cavities of Different

Cavity Radii. (g = 0.15 μm, λ = 1.55 μm)

Effect of the Air Gap:

Figure 7.5 shows the effects of varying the air gap g on T2, T3, T4 and R1 with different air gap widths. The results shown in figure 7.5 were obtained by fixing λ = 1.55 μm and r = 0.7612 μm. The following can be observed from the various curves:

I. Power coupling to port 4 reached a peak value of about 0.956 at g = 0.15 μm.

II. The optical power is almost completely dropped from the bus (T2 $\approx$ 0) at g = 0.15 μm.

III. The above observations lead us to conclude that the filter performance is optimized at g = 0.15 μm.

IV. The filter performance is substantially decreased for values of g lower or higher than 0.15 μm, causing T2 to increase and T4 to decrease in values.

V. Both R1 and T3 remains low ($\leq$ 0.008) in the entire range of figure 7.6.

VI. FPR gradually decrease with increasing g, reaching a value of about 0.032 at g = 0.15 μm.
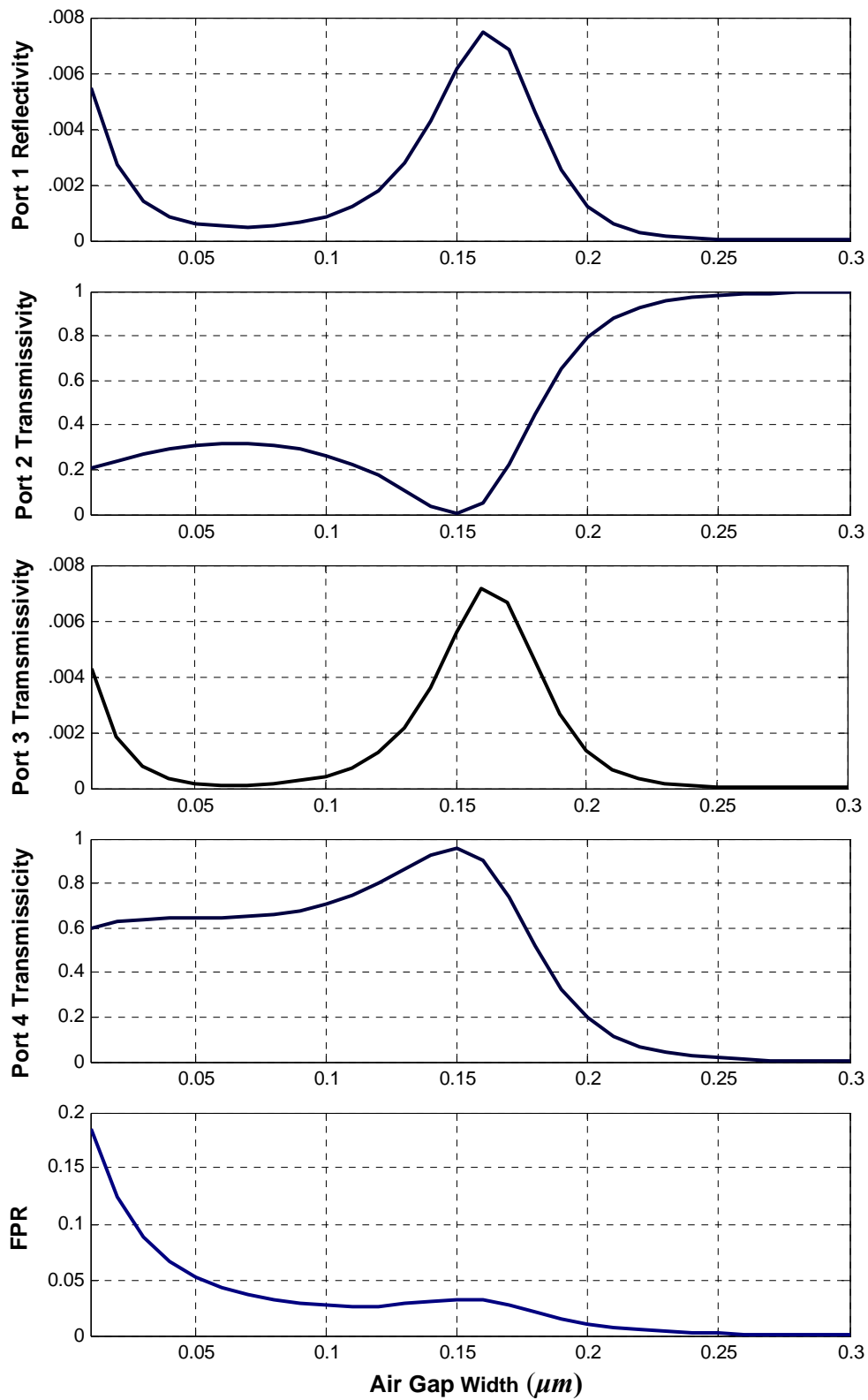
Figure 7.5: Effects of Air Gap (Cavity Radius 0.7612 μm, $\lambda = 1.55 \mu m$)

Images of the field intensity distributions are shown in figure 7.6 for various values of resonance radius. The images shown in figure 7.6 correspond to the resonant radii seen in figure 7.4. When r = 0.3890 μm (figure 7.6 a), the highest electric field intensity in the cavity is 1.8969 and three cycles are resonated inside the circular cavity. When r = 0.4859 μm (figure 7.6 b), the highest electric field intensity in the cavity is 1.7765 and four cycles are resonated inside the circular cavity. When r = 0.5796 μm (figure 7.6 c), the highest electric field intensity in the cavity is 1.9254 and five cycles are resonated inside the circular cavity. When r = 0.6712 μm (figure 7.6 d), the highest electric field intensity in the cavity is 2.2141 and six cycles are resonated inside the circular cavity. When r = 0.7612 μm (figure 7.6 e), the highest electric field intensity in the cavity is 2.2176 and seven cycles are resonated inside the circular cavity. When r = 0.8500 μm (figure 7.6 f), the highest electric field intensity in the cavity is 2.1904 and eight cycles are resonated inside the circular cavity. With increase of cavity size the number of cycles resonated in the cavity increases.

(a) 3 Cycles   (b) 4 Cycles   (c) 5 Cycles

(d) 6 Cycles   (e) 7 Cycles   (f) 8 Cycles
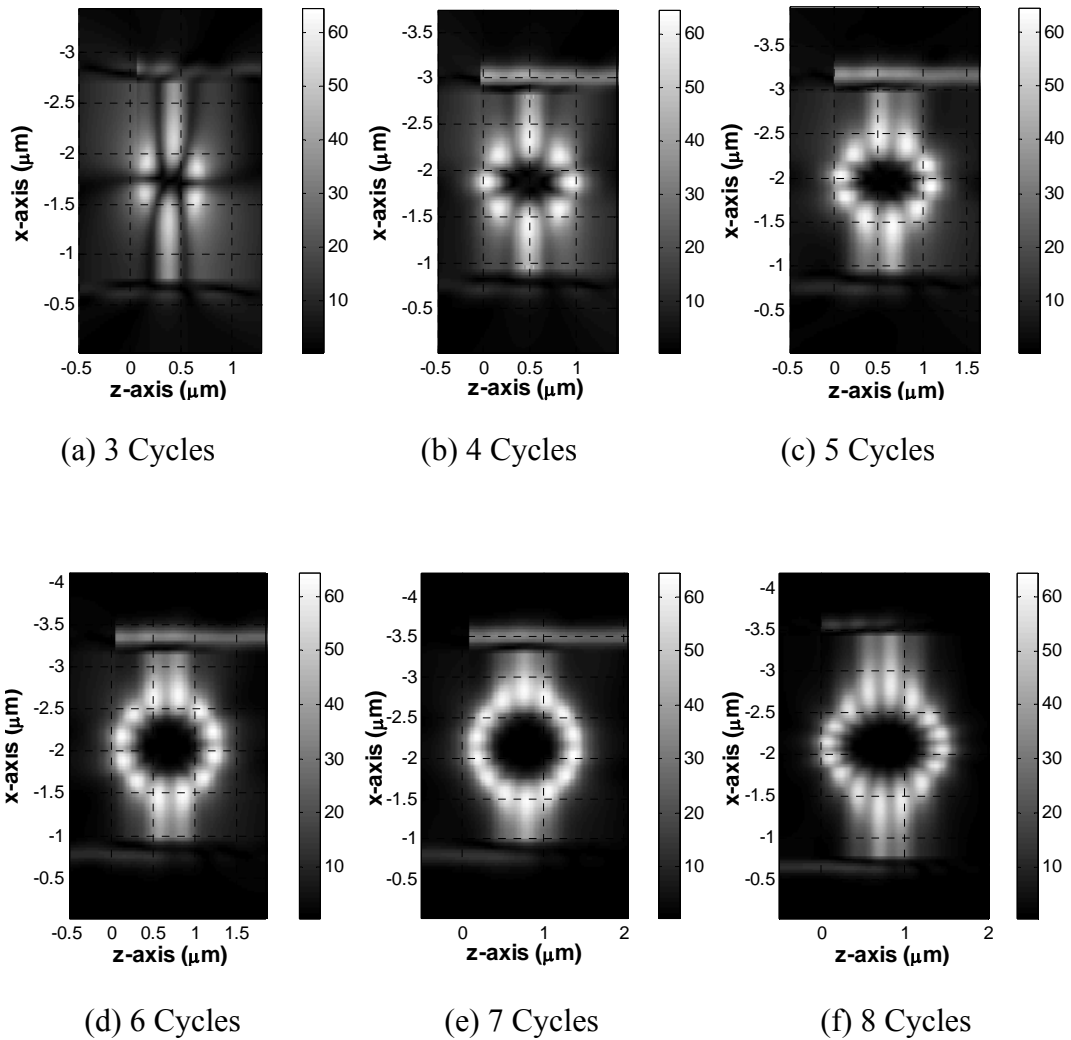
(a) Cavity Radius 0.3890 *μm*; (b) Cavity Radius 0.4859 *μm*;

(c) Cavity Radius 0.5796 *μm*; (d) Cavity Radius 0.6712 *μm*;

(e) Cavity Radius 0.7612 *μm*; (f) Cavity Radius 0.8500 *μm*.

Figure 7.6: Field Intensity Distribution of the Add/Drop Filter with Circular Cavity for various resonant radii. ($\lambda = 1.55$ *μm*, g = 0.15 *μm*.)

With add/drop filters with circular cavities in series in an optical network it is possible to drop different wavelengths for different users by using add/drop filers of suitable cavity sizes and air gap widths. The following figure (figure 7.7) shows a optical fiber network where two wavelengths λ_1 and λ_2 are dropped from a group of n wavelengths in a WDM system. In addition, the users can also use the add property of the filter to send information over the optical fiber network, using their allocated wavelength.
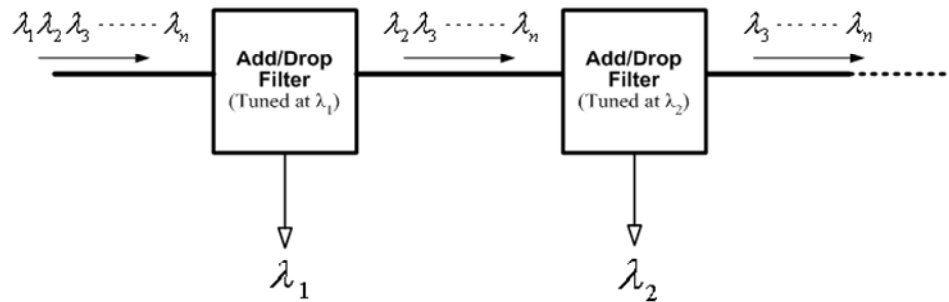
Figure 7.7: Add/drop filters with circular cavities connected in series in an optical fiber network

Port 4 responses of the add/drop filter with a circular cavity for r = 0.7612 μm and r = 0.7300 μm are shown in figure 7.8. The air gap width in both cases is fixed at g = 0.15 μm. It can be seen in the figure that for r = 0.7612 μm, the resonance wavelength is 1.55 μm. However there are two additional resonances at λ = 1.40 μm and λ = 1.755 μm on the two sides of the central resonance wavelength λ = 1.55 μm. When r is reduced to 0.7300 μm all the three resonance wavelengths shift toward lower wavelengths. We can also notice that the separation between the central and the side resonance wavelengths has increased lightly when the cavity radius is reduced from r = 0.7612 μm to r = 0.7300 μm.
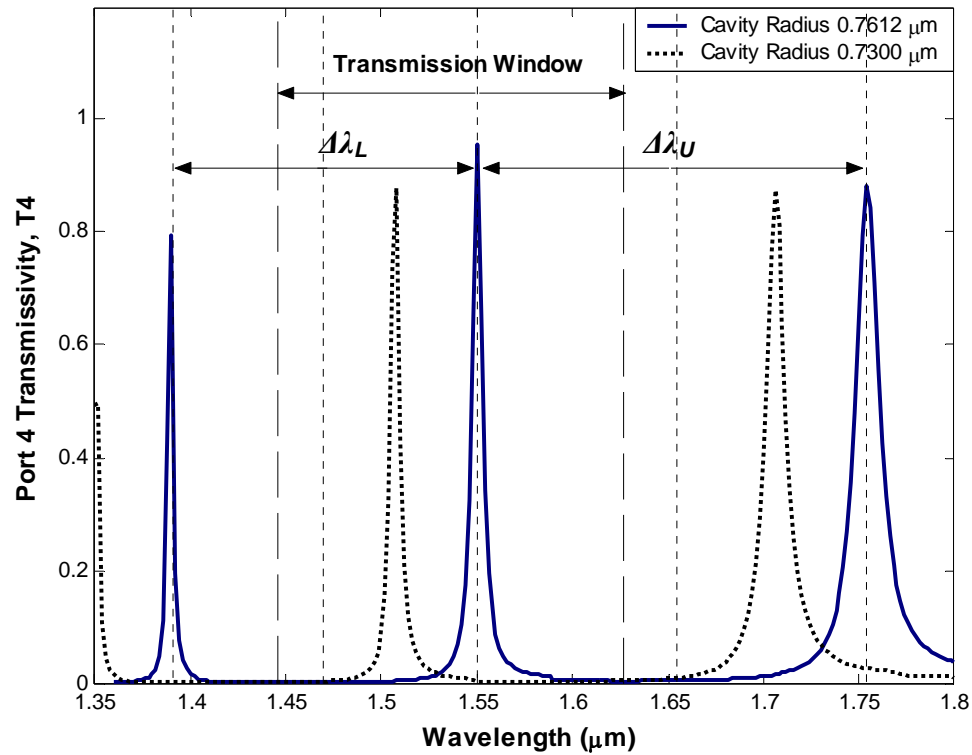
Figure 7.8: Port 4 Transmissivity of the Add/drop Filters with Cavity Radius 0.7612 *μm*

and 0.7300 *μm*. (g = 0.15 *μm*)

From figure 7.8 it can be suggested that we change the add/drop filter cavity radius and air gap widths to drop different wavelengths as long as the side resonance of one add/drop filter does not coincide with the central wavelength of another add/drop filter. So there has to be a range of wavelength where there will be only the central resonance wavelengths of add/drop filters of different cavity radii. This wavelength range is referred as the Transmission Window in the thesis work.

The transmission window size can be calculated from the difference between the central resonance wavelength and the two nearby resonance wavelengths. If the difference between central resonance wavelength and resonance at nearest lower wavelength is $\Delta\lambda_L$ and the difference between central resonance wavelength and resonance at nearest higher wavelength is $\Delta\lambda_U$ then the transmission window ($\Delta\lambda_W$) can be estimated by the following:

$$\Delta\lambda_W = \frac{\Delta\lambda_L + \Delta\lambda_U}{2} \qquad\qquad (7.4)$$

The number of add/drop filters that can be used in series depends on the width of the transmission window $\Delta\lambda_W$ and the minimum acceptable signal to noise ratio at the receiver. We will assume that the minimum acceptable signal to noise ratio at any receiver is 3dB. The noise in this case caused by optical interference from adjacent signals in a WDM fiber optics system. Table 7.1 shows the estimated highest possible number of channels which can be used in a WDM fiber optics system where the add/drop filters are connected in series. It can be seen from the table that with smaller cavity size it is possible to accommodate more channels because for small cavities the spectral widths decrease and the transmission window increases.

The smaller cavities look more attractive because of the higher number of channels in the transmission window, but those are difficult to fabricate with high precisions. An additional drawback of small cavity size is they have a lower drop/add efficiency when compared with the large cavity sizes.

Cavity Radius (*μm*)	Transmission window $\Delta\lambda_W$	Spectral width (3dB)	Estimated Number of channels in the transmission window
0.8500	0.1615	0.0032	50
0.7612	0.1824	0.0030	60
0.6712	0.2100	0.0030	70
0.5796	0.2486	0.0028	88
0.4859	0.3200	0.0038	84
0.3890	0.3856	0.0037	104

Table 7.1: Estimated number of channels for different circular cavity size

7.4 Add/Drop Filters with Elliptical cavity

The Elliptical cavity is simulated using the same approach used in the simulation of the circular cavity. We have used the stair-case approximation along with the equation of the ellipse to simulate the elliptical cavity shown in figure 7.9. If r_x and r_z are the two radii of an ellipse along x-axis and z-axis respectively then from the equation of ellipse:

$$\frac{x^2}{r_x^2} + \frac{z^2}{r_z^2} = 1 \tag{7.5}$$

The uniform layers along the z-axis of the circular cavity is reduced or expanded to achieve an elliptical cavity. Similar to circular cavity layers along x-axis and layers along z-axis and x-axis are calculated taking $r_z = r_x$. Then the uniform layers of z-axis are expanded or reduced to achieve the elliptical shape. r_z is taken greater than r_x ($r_z > r_x$) for an ellipse expanded along z-axis (see figure 7.9 a) and r_z is taken less than r_x ($r_z < r_x$) for an ellipse reduced along z-axis (see figure 7.9 b).
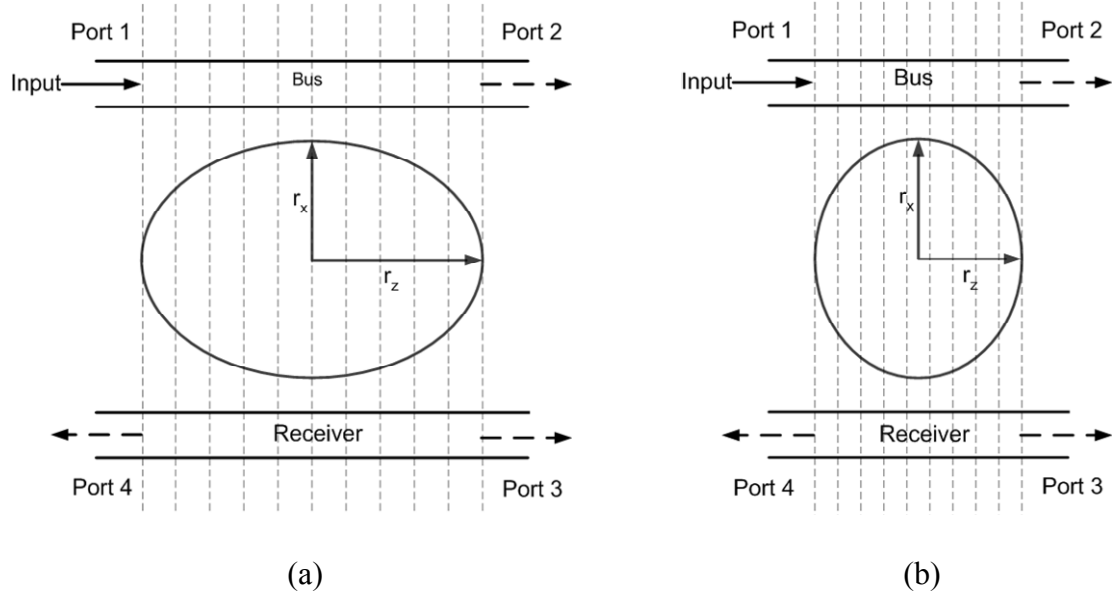
Figure 7.9: Add/drop Filter with elliptical Cavities. (a) $r_z > r_x$; (b) $r_z < r_x$

7.4.1 Numerical Results for Add/Drop Filters with Elliptical cavity $(r_z > r_x)$

In this section we present the numerical results of the add/drop filter with elliptical cavities of where $r_z > r_x$. The numerical results are shown along with the results of the circular cavity for convenience and added clarity.

Figure 7.10 shows the filter response of an add/filter with an elliptical cavity. Here radius $r_x = 0.7612$ μm and $r_z = 1.1$ r_x. The two waveguide are identical and have width 0.2 μm and air gap width g = 0.15 μm. The following are observed from the curves:

I. For the elliptical cavity with $r_z = 1.1$ r_x, the central resonant wavelength is at 1.632 μm, which is greather than 1.55 μm (which is the central resonance wavelength for circular cavity with $r_x = 0.7612$ μm).

II. At the central resonant wavelength ($\lambda = 1.632$ μm) T2 reduces to a value 0.035 and T4 reaches a peak value of 0.784.

III. T3 and R1 are very small at the resonance wavelength $\lambda = 1.632$ μm and have maximum values to 0.016 and 0.012 respectively.

IV. FPR reaches to 0.162 at $\lambda = 1.632$ μm and reaches to 0.282 at the next higher resonant wavelength $\lambda = 1.850$ μm.

V. The spectral width at the resonance wavelength ($\lambda = 1.632$ μm) of the add/drop filter with elliptical cavity ($r_z > r_x$) is more if compared to the spectral width at the resonance wavelength ($\lambda = 1.55$ μm) of the add/drop filter with circular cavity.
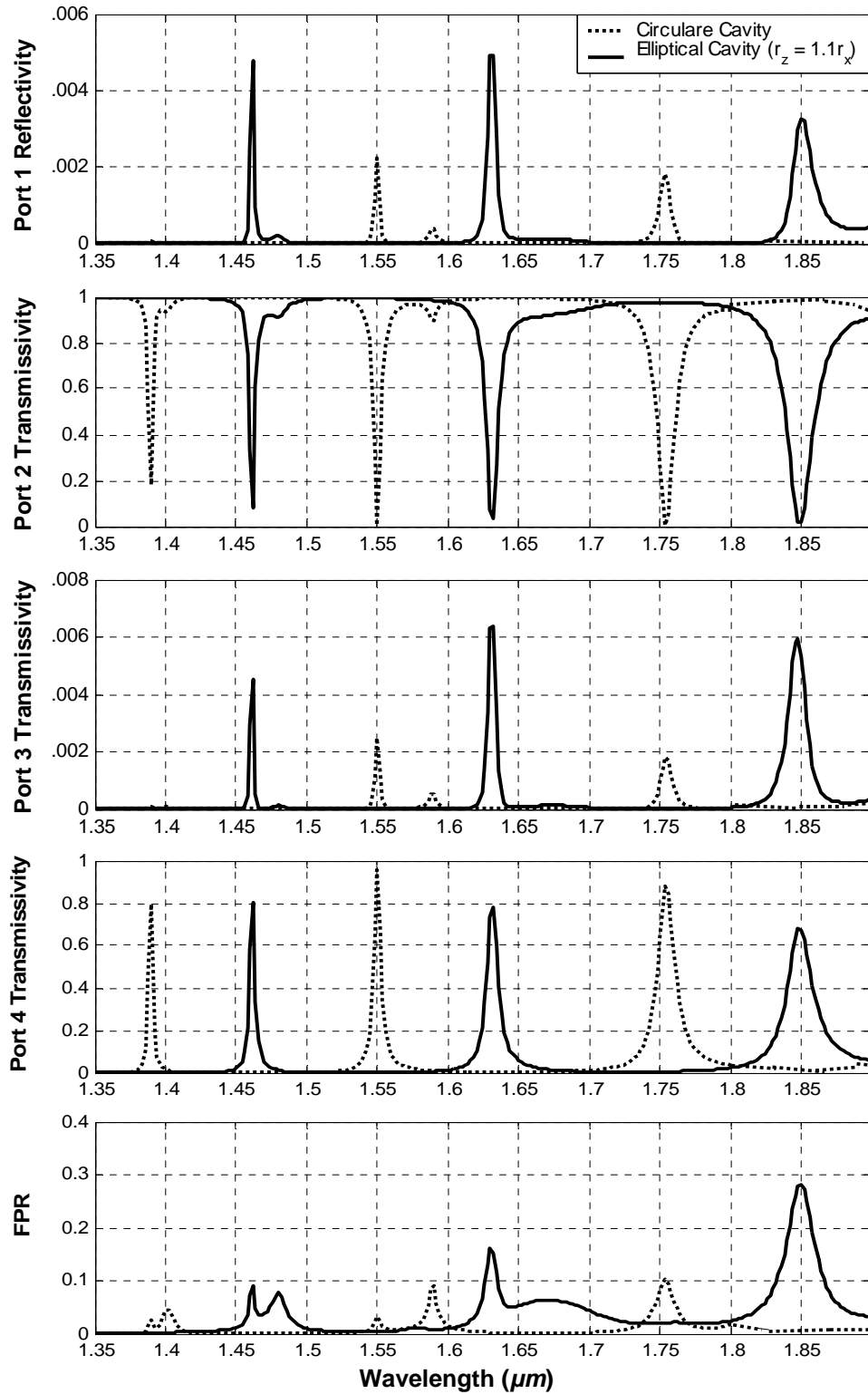
Figure 7.10: Filter Responses of Add/Drop Filters with Elliptical cavity ($r_z = 1.1\ r_x$) and

Circular Cavity with radius $r = r_x$. (g = 0.15 μm, $r_x = 0.7612\ \mu m$)

Effects of the Elliptical Cavity Radius for $r_z > r_x$

By fixing all parameters, including the operating wavelength, the effect of the cavity radius is examined. The wavelength is 1.55 μm and the air gap width is also fixed at 0.15 μm. The elliptical cavity is assumed to have a larger dimension in z-direction than its dimension in the x-direction with $r_z = 1.1\ r_x$. r_x is varied from 0.35 μm to 0.90 μm. Figure 7.11 shown the filter responses of the four ports of the add/drop filter. The followings are observed from the curves:

I. Similar to the circular cavity, the elliptical cavity also resonates at several values of radii at $\lambda = 1.55\ \mu m$. However the resonances occur at smaller radii than those of the circular cavity.

II. When the cavity radius is small, the value of T4 is very small at resonance radius. As the cavity size increases the value of T4 at resonance radius increases reaching a value of 0.849 at $r_x = 0.809\ \mu m$.

III. The values of R1 and T3 at resonance radii drop with increasing cavity radius. However, both R1 and T3 remain small (≤ 0.05) in the entire range of figure 7.11.

IV. The power loss to radiation as indicated by the FPR is large at the low resonance radii. The value of the FPR peaks to 0.432 at resonance radii $r_x = 1.1\ \mu m$.

V. The overall response of the add/drop filter with elliptical cavity of $r_x = 0.8\ r_x$ is poorer than the circular cavity.
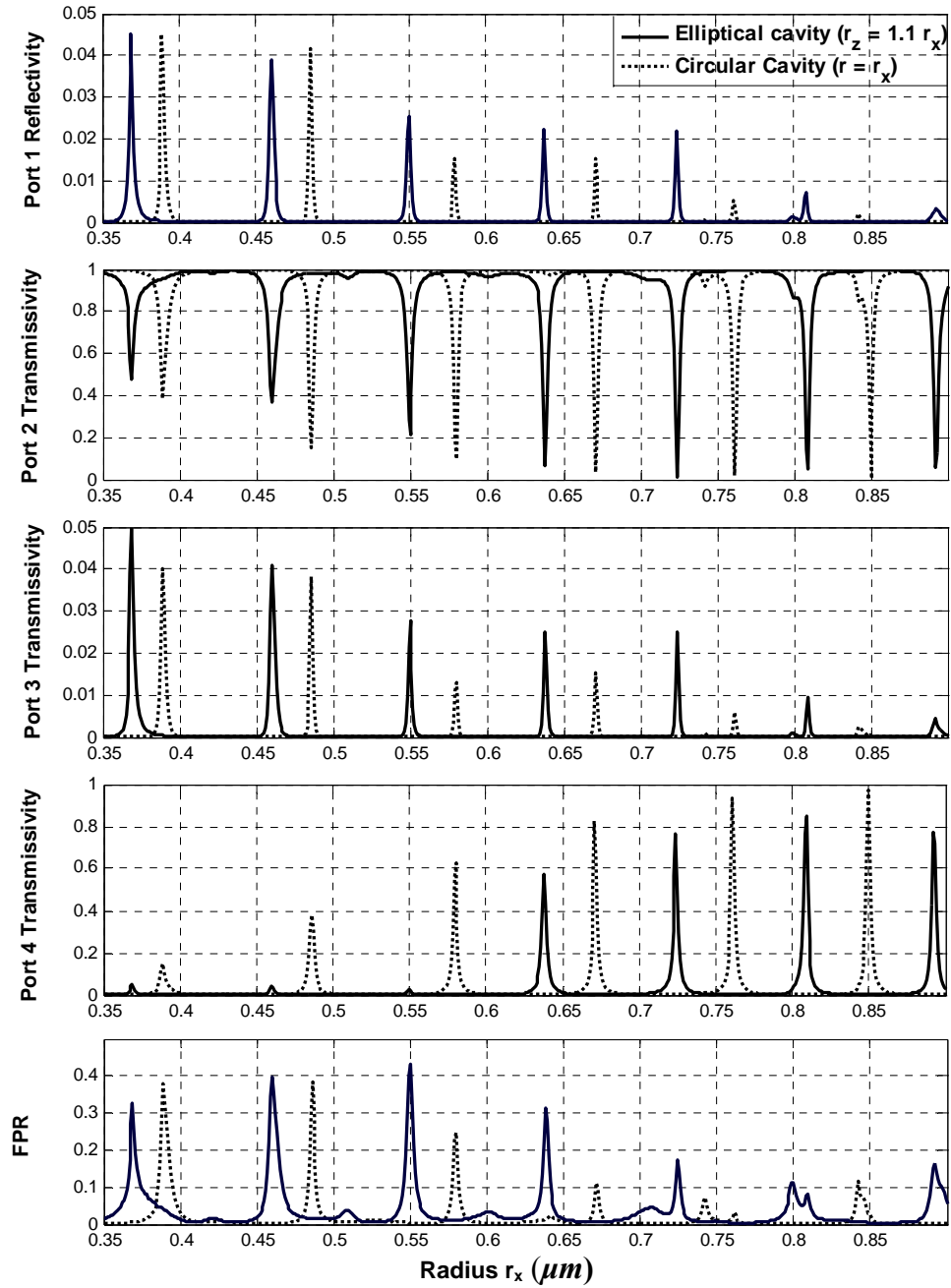
Figure 7.11: Filter Responses of Add/Drop Filters with Elliptical cavity ($r_z = 1.1\ r_x$) and Circular Cavity ($r = r_x$) with different Cavity Radii. (g = 0.15 μm, λ = 1.55 μm)

7.4.2 Numerical Results for Add/Drop Filter with elliptical cavity $(r_z < r_x)$

When the circular cavity radius along z-axis r_z is reduced to 0.8 r_x, the circle appears as an ellipse as shown in figure 7.9 (b).

Figure 7.12 shows the filter response of an add/filter with an elliptical cavity with $r_z <$ r_x. Here radius r_x = 0.7612 μm and r_z = 0.8 r_x. The two waveguide are identical and have width 0.2 μm and air gap width g = 0.15 μm. The followings are observed from the curves:

I. For the elliptical cavity with r_z = 0.8 r_x, the resonant wavelength is at 1.408 μm rather than 1.55 μm (which is the central resonance wavelength for circular cavity with r_x = 0.7612 μm). However there is another resonance at 1.592 μm closer to 1.55 μm.

II. At the central resonant wavelength (λ = 1.408 μm) T2 reduces to a value 0.096 and T4 reaches a peak value of 0.531.

III. T3 and R1 are very small at the resonance wavelength λ = 1.408 μm and have maximum values to 0.005 each. At resonance wavelength the value of T3 and R1 are smaller than the values of T3 and R1 for the add/drop filter wit circular cavity with r = 0.7612 μm.

IV. FPR reaches to 0.364 at λ = 1.408 μm.

V. The spectral width at the resonance wavelength λ = 1.592 μm of the add/drop filter with elliptical cavity (r_z = 0.8 r_x) is more if compared to the spectral width at the resonance wavelength of the add/drop filter with circular cavity (λ = 1.55 μm).
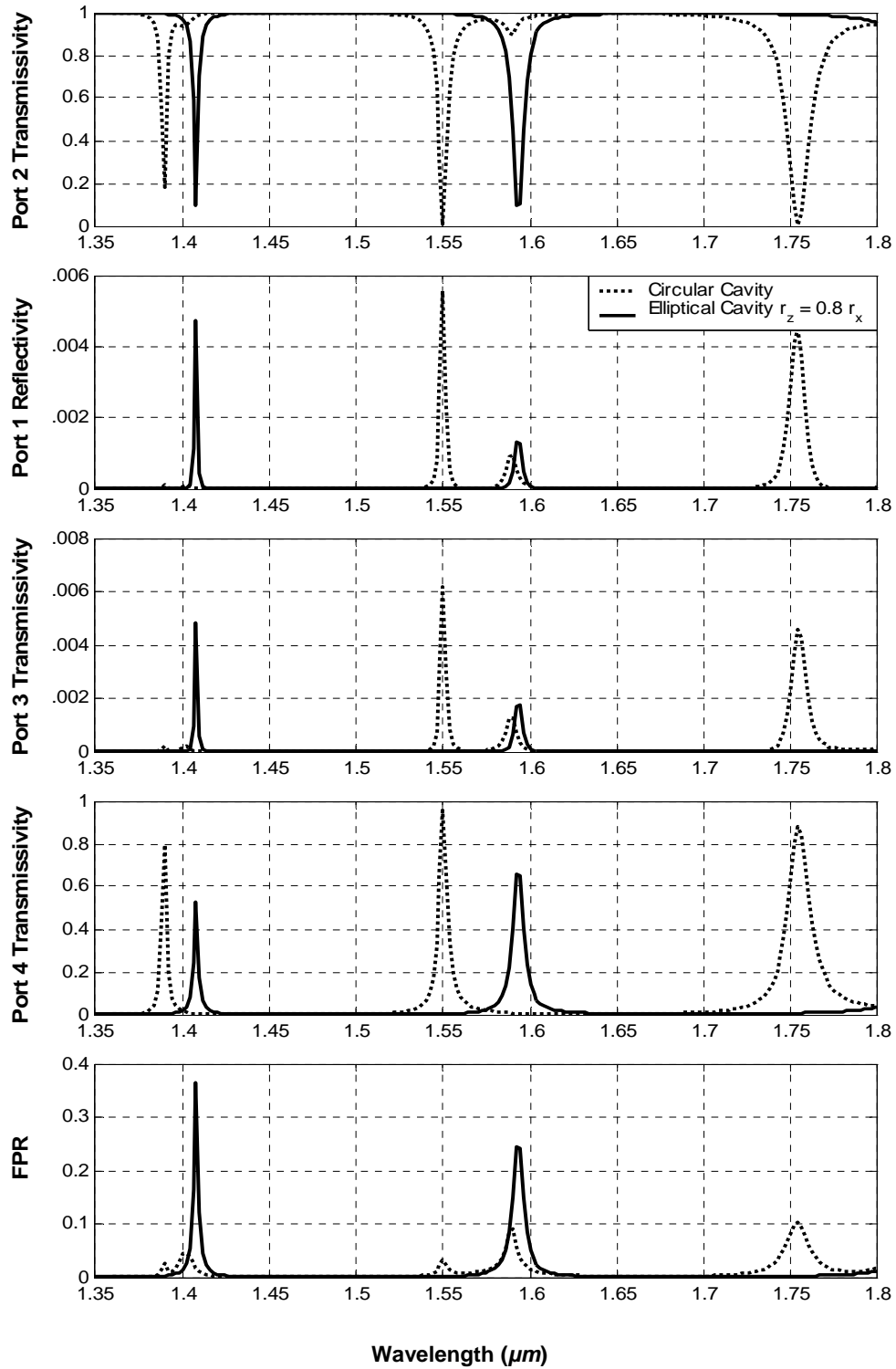
Figure 7.12: Filter Responses of Add/Drop Filters with Elliptical cavity ($r_z = 0.8\ r_x$) and

Circular Cavity with radius $r = r_x$. ($g = 0.15\ \mu m$, $r_x = 0.7612\ \mu m$)

Effects of the Elliptical Cavity Radius for $r_z < r_x$

By fixing all parameters, including the operating wavelength, the effect of the cavity radius is examined. The wavelength is 1.55 μm and the air gap width is fixed at 0.15 μm. The elliptical cavity is assumed to have a smaller dimension in z-direction than its dimension in the x-direction with $r_x = 0.8$ r_x. r_x is varied from 0.35 μm to 0.90 μm. Figure 7.13 shown the filter responses of the four ports of the add/drop filter along with filter response of add/drop filter with circular cavity ($r = r_x$). The followings are observed from the curves:

I. Similar to the circular cavity, the elliptical cavity with $r_x = 0.8$ r_x also resonates at several values of radii at $\lambda = 1.55$ μm. However, the resonances occur at smaller radii than those of the circular cavity.

II. When the cavity radius is small, the value of T4 is very small at resonance radius. As the cavity size increases the value of T4 at resonance radius increases reaching a value of 0.785 at $r_x = 0.84$ μm.

III. The values of R1 and T3 peak to 0.048 and 0.054 respectively at $r_x = 0.5360$ μm. The values of R1 and T3 at resonance radii drop with increasing cavity radius after $r_x = 0.5360$. However, both R1 and T3 remain small (≤ 0.055) in the entire range of figure 7.13.

IV. The FPR is large at the low resonance radii. The value of the FPR peaks to 0.415 at resonance radii $r_x = 0.639$ μm and gradually reduces with increasing radius.

V. The overall response of the add/drop filter with elliptical cavity of $r_x = 0.8$ r_x is poorer than the circular cavity.
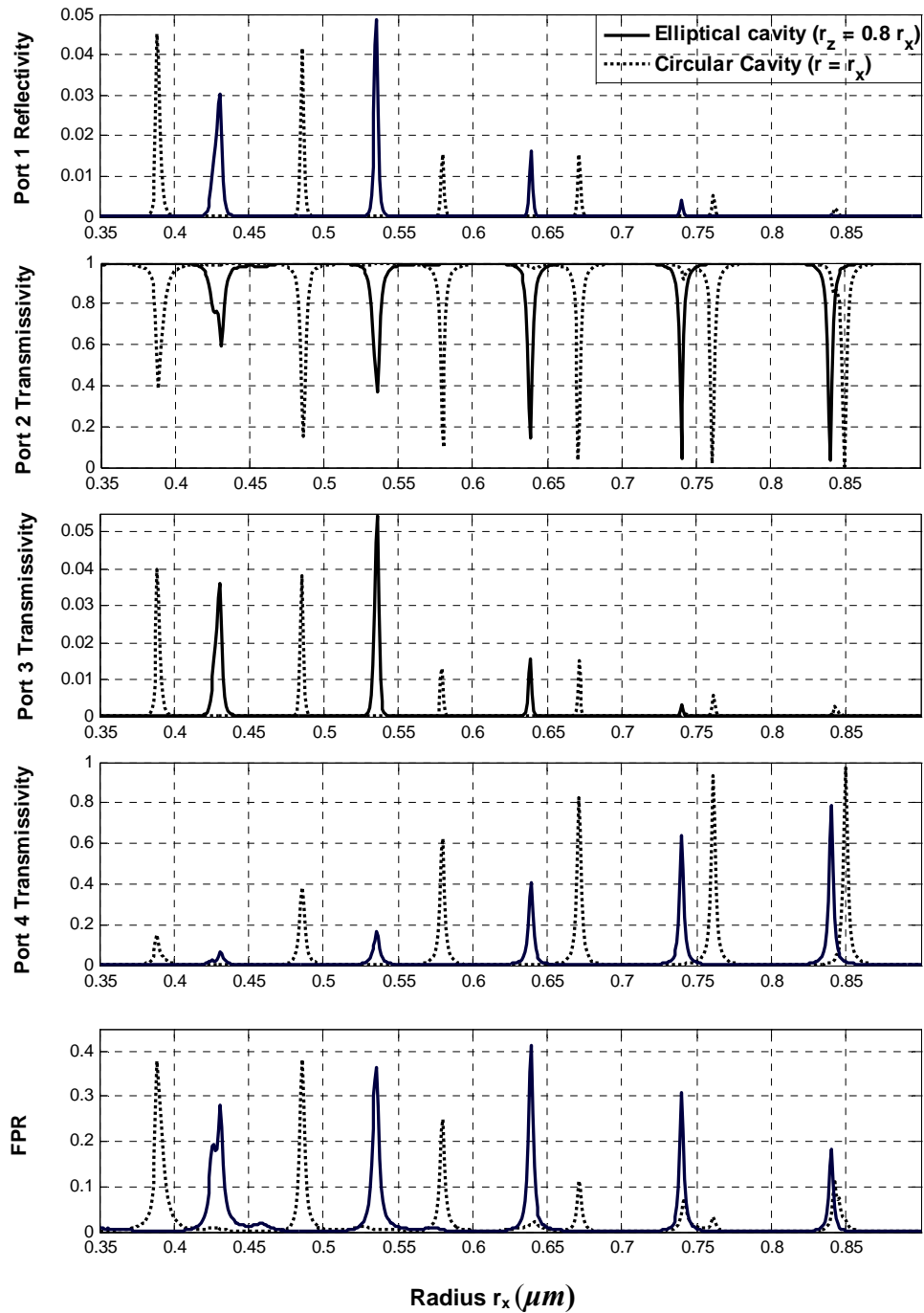
Figure 7.13: Filter Responses of Add/Drop Filters with Elliptical cavity ($r_z = 0.8\ r_x$) and

Circular Cavity ($r = r_x$) with different Cavity Radii. (g = 0.15 μm, λ = 1.55 μm)

Figure 7.14 shows images of the electric filed intensity distribution inside filter. It can be observed from the figure that When the add/drop filter with elliptical cavity width is larger than its height ($r_x = 0.809 \ \mu m$, $r_z = 1.1 \ r_x = 0.890 \ \mu m$), 8 cycles are resonated inside the cavity at resonant wavelength $\lambda = 1.55 \ \mu m$ (figure 7.15 a). The highest field intensity in side the cavity in this case is 3.199. When the add/drop filter with elliptical cavity width is smaller than its height ($r_x = 0.7405 \ \mu m$, $r_z = 0.8 \ r_x = 0.5924 \ \mu m$), 6 cycles are resonated inside the cavity at resonant wavelength $\lambda = 1.55 \ \mu m$ (figure 7.15 b). The highest field intensity inside the cavity in this case is 3.278.

(a) $r_x = 0.809 \ \mu m$, $r_z = 1.1 r_x = 0.890 \ \mu m$;   (b) $r_x = 0.7405 \ \mu m$, $r_z = 0.8 \ r_x = 0.5924 \ \mu m$;
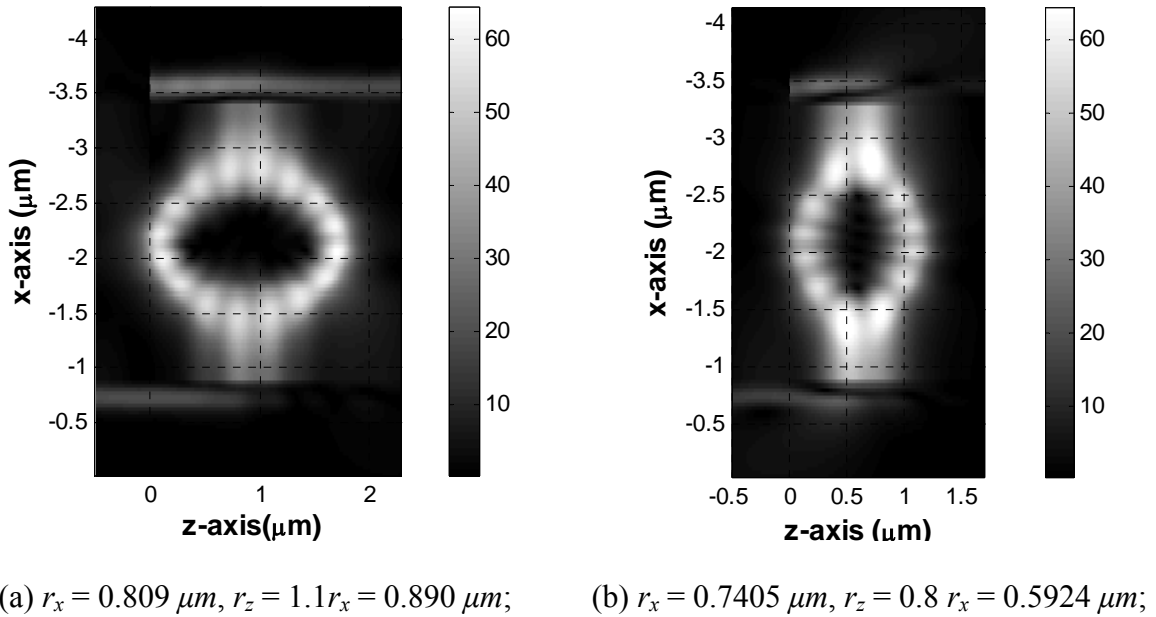
Figure 7.14: Electric Field Intensity Distributions inside Add/Drop Filter with

Elliptical Cavities, (g = 0.15 μm, $\lambda = 1.55 \ \mu m$)

7.5 Filter response comparison between the add/drop filter with circular and elliptical cavity

Figure 7.15 shows the filter response of an add/filters with elliptical cavities $r_z = 0.8\ r_x$ and $r_z = 1.1\ r_x$, together with filter responses of add/drop filters with circular cavity with $r = r_x$. Here Air gap g $= 0.15\ \mu m$ and $r_x = 0.7612\ \mu m$. The followings are observed from filter responses of add/drop filters with the circular and the elliptical cavities:

I. When the circular cavity ($r = 0.7612\ \mu m$) is expanded along z-axis ($r_z = 1.1\ r_x$) the resonant wavelengths shifts to higher wavelength ($\lambda = 1.632\ \mu m$) and when the circular cavity is shrunk along z-axis ($r_z = 0.8\ r_x$) the resonant wavelengths shifts to lower wavelength ($\lambda = 1.408\ \mu m$).

II. At resonance T2 in the circular cavity case drops to nearly zero and T4 peaks to nearly 1. In case of elliptical cavities the minimum values of T2 is about 0.05 and T4 peaks to 0.8 at resonance. Minimum values of R1, T3 and FPR for elliptical cavity cases are not as small as those of the circular cavity case.

III. For the elliptical cavity the transmission window is a little wider than the circular cavity.

Observing the above results it is observed that the power is almost completely dropped from the bus to the receiver waveguide at resonance when a circular cavity is used, which is not the case for the elliptical cavity. This feature makes the add/drop filter with circular cavity superior to add/drop filter with elliptical cavities.
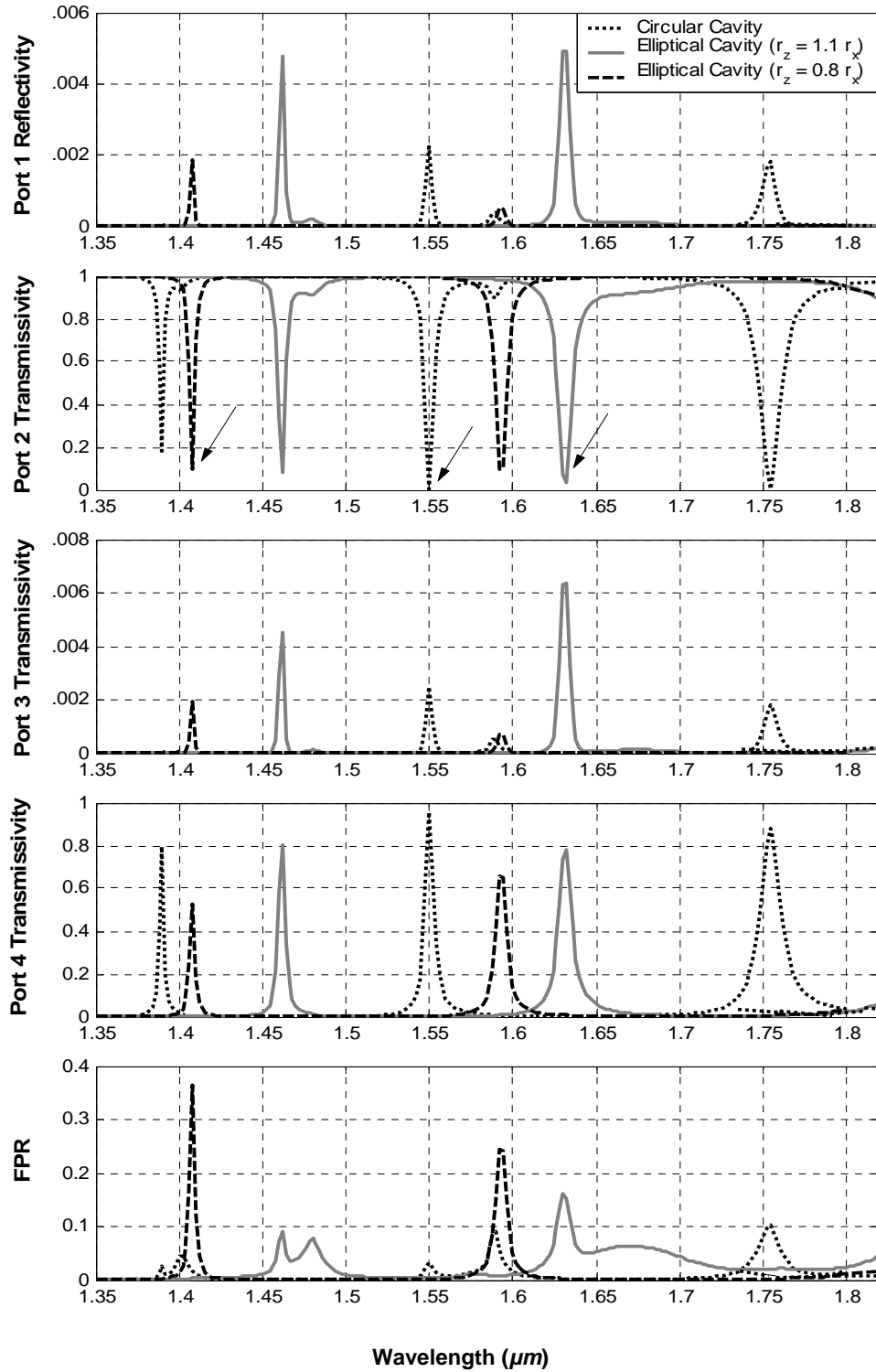
Figure 7.15: Filter Responses of Add/Drop Filters with circular cavity with $r = r_x$ and

Elliptical cavities with $r_z = 0.8\ r_x$ and $r_z = 1.1\ r_x$. ($r_x = 0.7612\ \mu m$, g = 0.15 μm)

Chapter 8

Summary, Conclusion and Future Work

8.1 Introduction

In this thesis work Method of Lines has been used for the analysis of Add/Drop Filter with imbedded cavities of different shapes and size. Enhancement of the Method of Line has been carried out by using an improved higher order approximation of the transverse second derivative operator. An absorbing PML layer of tan-profile has also been implemented. The staircase approach has been used successfully to simulate the circular and elliptical cavities. In this chapter a brief summary of the work that has been carried out in the theses is presented followed by conclusions and some suggestions for extension of the work.

8.2 Summary

- The MOL with the improved higher order approximations of the transverse second derivative operator has been implemented for Add/Drop Filters. The three-point and the five point approximations were implemented for these structures with high contrast.

- PML with absorbing boundary conditions with non linear tangent loss profile has been implemented and it has successfully improved performance. The PML has been used extensively in this work to absorb the radiative field.

- Longitudinal waveguide discontinuities have been studied using the improved MOL. The layer by layer method were used to analyze multiple longitudinal discontinuities and compared with results in the literature.

- Add/Drop Filters with single and multiple imbedded square cavities have been simulated with MOL using layer by layer Algorithm in an efficient manner. Their filter responses have been calculated numerically and the effects of different parameters on the filtering performance of the device have been analyzed.

- Staircase approximations have been used efficiently with the layer by layer algorithm to simulate Add/Drop Filters with imbedded circular and elliptical cavities. The filter responses of the four ports have been calculated numerically. The effects of different parameters on the filtering performance and the whispering gallery modes of the device have been analyzed.

8.3 Conclusions

- The three points and the five point approximations are used in the MOL to model waveguide structure. It is found that the improved higher order approximations required relatively fewer discretization points along x-axis to sample the problem space. The approach used in the approximation allows the refractive index and the mesh size to vary in an arbitrary manner from one layer to the adjacent layer. This results in flexible and numerically efficient simulations.

- An improved PML with a non-uniform tangent loss profile is shown to give a superior performance when compared to the ordinary PML with uniform loss profile. The improved PML requires fewer number of mesh points than that of the PML with uniform loss profile. The PML is easily incorporated into the MOL and the matrix size for the basic MOL is not increased substantially.

- The layer by layer algorithm was used to calculate the filter response of add/drop Filter with single and multiple square cavities. The results of the single and double square cavities agree with already published results. With simulations it is shown that, with two identical square cavities it is possible to drop approximately 95% of the power at a certain wavelength from the bus waveguide, of which 65% is at a certain port (Port 3) of the receiver. But with three identical square cavities the performance of the add/drop filter deteriorate.

- Staircase approximation has been used efficiently with the layer by layer algorithm to simulate add/drop Filters with circular imbedded cavities with the hope that it would improve the filtering efficiency of the add/drop Filter. Their filter responses show dramatic improved performance over the square cavities. It

is shown that with circular cavity it is possible to drop a certain wavelength completely from the bus waveguide to one port of the receiver waveguide without disturbing the other wavelengths by WGM.

- Add/Drop Filter with an imbedded Elliptical cavity has also been simulated with the hope of a superior performance than that of a circular cavity. But it was observed that the filter performance of an elliptical cavity is not as good as the circular cavity.

- It can be concluded that add/drop filter with a circular cavity has the best filtering performance among all the add/drop filters analyzed in this thesis work.

8.4 Future Prospects

There is always some room for improvements in any scientific research. The following is a brief list of suggestions for possible future work in this area.

- We have analyzed the filter response and filtering efficiency of add/drop Filter with single and multiple square cavities, circular cavities and elliptical cavities. The filter response of add/drop filter with multiple circular cavities and elliptical cavities can also be analyzed with the help of MOL.

- The filter response of Add/Drop Filter with circular cavity has been analyzed in this thesis work. One can look into the behavior of an add/drop Filter with ring resonator and vertically coupled microring resonator (VCMRR) using MOL.

- All the numerical simulations done in this thesis work are for 2D models. As 3D waveguide modeling gives more realistic results than a 2D model, extension of

this work to 3D is also of importance. As circular and elliptical cavities need staircase approximation for simulations with MOL, they require large number of layers. This results in higher computational time and memory requirements. So for 3D simulations of Add/Drop Filters, new approaches like Pade Approximations may be considered.

Appendix A

Improved Higher-Order Approximations

A.1 The three point formulation

Referring to figure A.1, the following is the final is the final expression for the 3-point

approximation technique:

$$\begin{bmatrix} \psi_{i-}^{(1)} \\ \psi_{i-}^{(2)} \\ \psi_{i-}^{(3)} \end{bmatrix} = C^{-1} \begin{bmatrix} \psi_{i-1} \\ \psi_i \\ \psi_{i+1} \end{bmatrix} \qquad\qquad (A.1)$$

where

$$C = \begin{bmatrix} & q_i^- & \\ 1 & 0 & 0 \\ & q_{i+1}^+ M_i & \end{bmatrix}$$ (A.2)

$$M_i^{\pm} = \begin{bmatrix} 1 & 0 & 0 \\ 0 & \rho_i^{\pm 1} & 0 \\ \mp \delta_i & 0 & 1 \end{bmatrix}$$ (A.3)

$$q_i^{\pm} = \begin{bmatrix} 1 & \pm h_i & \dfrac{h_i^2}{2!} \end{bmatrix}$$ (A.4)

$$N_i^{\pm} = \begin{bmatrix} 1 & \pm h_i & \dfrac{h_i^2}{2!} \\ 0 & 1 & \pm h_i \\ 0 & 0 & 1 \end{bmatrix}$$ (A.5)

where $\rho_i = 1$ for the TE waves and $\rho_i = \dfrac{n_{i+1}^2}{n_i^2}$ for the TM waves, and $\delta_i = k_0^2 \left(n_{i+1}^2 - n_i^2 \right)$.
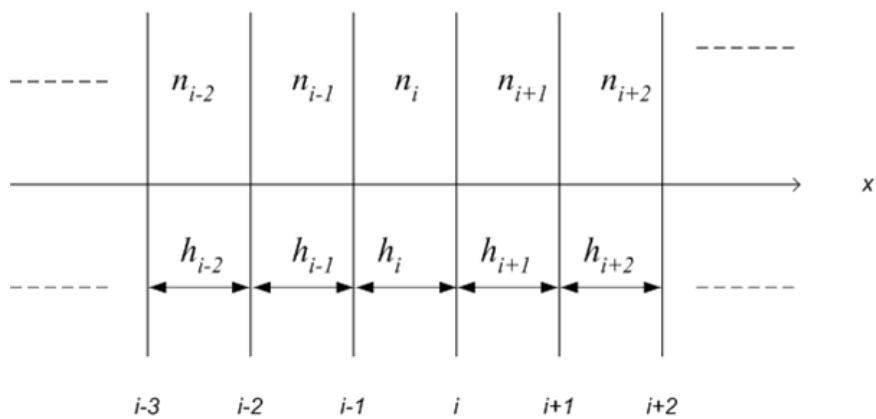
Figure A.1: Generalized refractive index and mesh size distributions

A.2 The Seven-Point Formulation

The seven-point transverse second derivative approximation can also be found in a similar manner. The relevant matrices in this case are given below:

$$
\begin{bmatrix}
\psi_i \\
\psi_{i-}^{(1)} \\
\psi_{i-}^{(2)} \\
\psi_{i-}^{(3)} \\
\psi_{i-}^{(4)} \\
\psi_{i-}^{(5)} \\
\psi_{i-}^{(6)}
\end{bmatrix}
= C^{-1}
\begin{bmatrix}
\psi_{i-3} \\
\psi_{i-2} \\
\psi_{i-1} \\
\psi_i \\
\psi_{i+1} \\
\psi_{i+2} \\
\psi_{i+3}
\end{bmatrix}
\tag{A.6}
$$

where the matrices C, M, q and N are given below

$$
C =
\begin{bmatrix}
q_{i-2}^- & M_{i-2}^- & N_{i-1}^- & & M_{i-1}^- & N_{i-1}^- \\
& q_{i-1}^- & M_{i-1}^- & N_{i-1}^- & & \\
& & q_i^- & & & \\
1 & 0 & 0 & 0 & 0 & 0 & 0 \\
& & q_{i+1}^+ M_i & & & \\
& q_{i+2}^+ & M_{i+1}^+ N_{i+1}^+ & M_i & & \\
q_{i+3}^+ & M_{i+2}^+ & N_{i+2}^+ & M_{i+1}^+ N_{i+1}^+ & M_i
\end{bmatrix}
\tag{A.7}
$$

$$
M_i^{\pm} = \begin{bmatrix}
1 & 0 & 0 & 0 & 0 & 0 & 0 \\
0 & \rho_i^{\pm 1} & 0 & 0 & 0 & 0 & 0 \\
\mp\delta_i & 0 & 1 & 0 & 0 & 0 & 0 \\
0 & \mp\rho_i^{\pm 1}\delta_i & 0 & \rho_i^{\pm 1} & 0 & 0 & 0 \\
\delta_i^2 & 0 & \mp 2\delta_i & 0 & 1 & 0 & 0 \\
0 & \rho_i^{\pm 1}\delta_i^2 & 0 & \mp 2\rho_i^{\pm 1}\delta_i & 0 & \rho_i^{\pm 1} & 0 \\
\mp\delta_i^3 & 0 & 3\delta_i^2 & 0 & \mp 3\delta_i & 0 & 1
\end{bmatrix}
\tag{A.8}
$$

$$
q_i^{\pm} = \begin{bmatrix}
1 & \pm h_i & \dfrac{h_i^2}{2!} & \dfrac{\pm h_i^3}{3!} & \dfrac{h_i^4}{4!} & \dfrac{h_i^5}{5!} & \dfrac{h_i^6}{6!}
\end{bmatrix}
\tag{A.9}
$$

$$
N_i^{\pm} = \begin{bmatrix}
1 & \pm h_i & \dfrac{h_i^2}{2!} & \dfrac{\pm h_i^3}{3!} & \dfrac{h_i^4}{4!} & \dfrac{h_i^5}{5!} & \dfrac{h_i^6}{6!} \\[2ex]
0 & 1 & \pm h_i & \dfrac{h_i^2}{2!} & \dfrac{\pm h_i^3}{3!} & \dfrac{h_i^4}{4!} & \dfrac{h_i^5}{5!} \\[2ex]
0 & 0 & 1 & \pm h_i & \dfrac{h_i^2}{2!} & \dfrac{\pm h_i^3}{3!} & \dfrac{h_i^4}{4!} \\[2ex]
0 & 0 & 0 & 1 & \pm h_i & \dfrac{h_i^2}{2!} & \dfrac{\pm h_i^3}{3!} \\[2ex]
0 & 0 & 0 & 0 & 1 & \pm h_i & \dfrac{h_i^2}{2!} \\[2ex]
0 & 0 & 0 & 0 & 0 & 1 & \pm h_i \\[2ex]
0 & 0 & 0 & 0 & 0 & 0 & 1
\end{bmatrix}
\tag{A.10}
$$

Here $\rho_i = 1$ for the TE waves and $\rho_i = \dfrac{n_{i+1}^2}{n_i^2}$ for the TM waves, and $\delta_i = k_0^2\left(n_{i+1}^2 - n_i^2\right)$.

Appendix B

Stf1 Program: Zero Finding Routine,

Eigenvalue Finding Routine

```
%_____
% Written By: Dr. H. A. Al-Jamid
% Professor, Electrical Engineering Department,
% King Fahd University of Petroleum & Minerals, Dhahran, KSA
%_____
% zero.m is a zero-finding program based on Muller's method.
% to use it, define the function who's zero is to be found as an M-file
% ( i.e ftest.m) , then run zero.m with the initial guess.
% the ftest.m file may for example be:
%
%    function y=ftest(x);
%    y=x^2-2.001*x+1.001;
%
%   run mat386 then type:
%
%  zero('ftest',1.9);
%
% where ftest is the fuction name (must be the same as the M-file name),
% 1.9 is the initial guess.
%
function b=zero(FunFcn,x2);
```

```
global flag;

flag=0;% Reset flag.

nm=10;%nm=input('number of iterations required = ');
low=10^(-10);
h1=-1*10^(-6);
h2=.5*10^(-6);
x1=x2-h2;
x0=x1-h1;
f0=feval(FunFcn,x0);

flag=1;% Set flag.

f1=feval(FunFcn,x1);
f2=feval(FunFcn,x2);
fu=(f2-f1)/h2;
fd=(f1-f0)/h1;
%
%start loop
%
for m=1:nm;
f3=(fu-fd)/(h1+h2);
c=fu+h2*f3;
h1=h2;
pa=c-sqrt(c*c-4*f2*f3);
ma=c+sqrt(c*c-4*f2*f3);
paa=abs(pa);
maa=abs(ma);
if paa>maa;
h2=-2*f2/pa;
else h2=-2*f2/ma;
end
x1=x2;
x2=x2+h2;
f1=f2;
f2=feval(FunFcn,x2);
%m
%[x2 f2]
fd=fu;
fu=(f2-f1)/h2;
if abs(f2)<low zr=x2;
end
low=min(low,abs(f2));
end
format long e
[zr feval(FunFcn,zr)]
```

```
%_____
%                              STF1
% This program computes the eigenvalues of guided
% TE and TM modes of a slab waveguide with an arbitrary number of
% layers.
% nps=superstrate refracive index squared. The superstrate is assumed
% to occupy the region x>0.
% nbs=substrate refractive index squared.
% ns=array containing the refractive index squared distribution of the
% layers between the superstrate and the substrate. The first entry
% corresponds to a layer next to the superstarate.
% d is similar to ns, but it contains the width distribution of the
% layers.
% Let TE=1 or any other non-zero number if TE modes are desired
% otherwise let TE=0 for TM modes.

function f=stf1(ne);

global co;
global lo;
global d;

TE=1;
%TE=0;

lambda=1.55;

nps=1.0^2;
nbs=1.0^2;
ns=[3.20^2];

d=[1 .6 1];

% Start calculation.

nes=ne*ne;
k0=2*pi/lambda;
asp=k0*sqrt(nes-nps);

%asp=-asp;%asp=-asp to account for leaky waves in the superstrate.

l1=k0*sqrt(ns(1)-nes);
rho=1;if TE==0;rho=ns(1)/nps;end;
a=1;
b=rho*asp/l1;
```

```
co=[a b];
lo=[l1];
m=length(ns);

for s=2:m;
    l=k0*sqrt(ns(s-1)-nes);
    lp=k0*sqrt(ns(s)-nes);

    t=d(s-1);
    lt=l*t;

    rho=1;if TE==0;rho=ns(s)/ns(s-1);end;
    at=a*cos(lt)+b*sin(lt);
    b=rho*(-a*sin(lt)+b*cos(lt))*l/lp;
    a=at;

    co=[co
       a b];

    lo=[lo
        lp];

    end;

    l=k0*sqrt(ns(m)-nes);
    asb=k0*sqrt(nes-nbs);

    %asb=-asb;%asb=-asb to account for leaky waves in the substrate.

    t=d(m);
    lt=l*t;

    rho=1;if TE==0;rho=nbs/ns(m);end;

    at=a*cos(lt)+b*sin(lt);
    a=-rho*(-a*sin(lt)+b*cos(lt))*l/asb;

    f=at-a;

% Compute the matrix co and lo used for plotting the eigenfields.

    co=[1 0
        co
        a 0];

    lo=[asp
        lo
```

```
        asb];
%_____
%                          STFG
% This program is used to plot the eigenfield of modes. The output
% from STF1 is used for this purpose.

global co;
global lo;
global d;

np=50;

% Define the x-coordinates.

xl=-abs(log(.001)/lo(1,1));

xhd=abs(log(.001)/lo(length(lo)));

ld=length(d);
sd=sum(d);

xd=[];

for i=1:ld;
xd=[xd
    sum(d(1:i))];
end;

x=[xl
    0
    xd
    xhd+sd];

lx=length(x);
on=ones(np,1);

% Compute field and position in the superstrate.

xt=cumsum((x(1)/np)*on);
xt=flipud(xt);
xt=[xt
    0];

gf=[xt exp(xt*lo(1))];

% Compute field within the intermediate layers.
for i=2:lx-2;
```

```
 xt=cumsum(((x(i+1)-x(i))/np)*on);
 xt=x(i)+xt;
 gf=[gf
     xt co(i,1)*cos(lo(i)*(xt-x(i)))+co(i,2)*sin(lo(i)*(xt-x(i)))];
 end;

% Compute field in the substrate.
xt=cumsum(((x(lx)-x(lx-1))/np)*on);
xt=xt+x(lx-1);
gf=[gf
xt co(lx-1,1)*exp(-lo(lx-1)*(xt-sd))];

% Plot modal field vx x.
%plot(gf(:,1),(abs(gf(:,2))/max(abs(gf(:,2)))));%pause;plot(gf(:,1),(real(g
f(:,2))/max(real(gf(:,2)))))
plot(-gf(:,1),(abs(gf(:,2))/max(abs(gf(:,2)))))
```

Appendix C

MOL Three-Point Approximation

```
%_____
% Written By: Mohammad Mahbubul Isalm
% This function will calculate the square matrix Q of equation 3.17
% by using the Method of Lines (MOL), 3 point.
% Implementing the boundary conditions at the two meshes
% points at the interface.
%
% [Q,N]=threept(n,M,h1,n1,TE,K0)
%
% TE = Mode selection,
% TE = 1 for TE mode and TE = 0 for TM mode
% n = Vector (equal number of layers) of refractive indices of layers
% n1 = Vector (equal number of mesh points) of refractive indices of layers
% h1 = Vector (equal number of mesh points) of layer widths
% M = Vector containing number of discretization points of layers
%(superstate, core, substate)
% K0 = Free space wave number
%_____
function [Q,N]=threept(n,M,h1,n1,TE,K0);

%%% total number of layers %%%
nlyr=length(n);
MN=cumsum(M);   %Interface points
```

```matlab
%%% REFRACTIVE INDEX MATRIX (N^2)
N=diag(n1.^2);

%%% C Matrix %%%
MM=sum(M);
C=zeros(MM);
C(1,1)=-2;
C(1,2)=1;
C(MM,MM)=-2;
C(MM,MM-1)=1;
for i=2:MM-1
    C(i,i-1)=1; %Subdiag. elements
    C(i,i)=-2;  %diagonal elements
    C(i,i+1)=1; %Superdiag.elements
end

%%%%%(deviding by h^2)%%%%%%
C(1,:)=C(1,:)/h1(1)^2; %first row
for i1=2:length(h1)-1   %from 2nd row to row before last
    if abs(h1(i1))==abs(h1(i1+1))&&n1(i1)==n1(i1+1)
        C(i1,:)=C(i1,:)/h1(i1)^2;
    end
    if abs(h1(i1))~=abs(h1(i1+1))||n1(i1)~=n1(i1+1)
        if TE==1
        r21=1;
        else
        r21=(n1(i1+1)/n1(i1))^2;
        end
        B=K0^2*(n1(i1)^2-n1(i1+1)^2);
        D=0.5*((h1(i1)*h1(i1+1)*r21)+h1(i1+1)^2);
        C(i1,i1-1)=(h1(i1+1)/h1(i1))*r21/D;
        C(i1,i1)=-((r21*h1(i1+1)/h1(i1))+1+0.5*h1(i1+1)^2*B)/D;
        C(i1,i1+1)=C(i1,i1+1)/D;
    end
end
i1=length(h1);C(i1,:)=C(i1,:)/h1(i1)^2;  % last row


%%% Q MATRIX %%%
Q=C+K0^2*N
```

Appendix D

MOL Five-Point Approximation and Its

Functions

```
%_____
% Written By: Mohammad Mahbubul Isalm
% This function will calculate the square matrix Q of equation 3.17
% by using the Method of Lines (MOL), 5-point.
% Implementing the boundary conditions at the two meshes points at the % %
interface.
%
% Q=fivept (n,h,TE,K0)
%
% n = Vector (equal number of layers) of refractive indices of layers
% h = Vector (equal number of mesh points) of layer widths
% TE = Mode selection, TE = 1 for TE mode and TE = 0 for TM mode
% K0 = Free space wavenumber
%_____

function Q=fivept (n,h,TE,K0);
Qt=[];% 5 col metrix containg the Cs

n=n.^2.';
mx=length(n);
%%% C Matrix %%%
for k=1:mx
```

```
    if k<2 qm=qminus(h(k)); Mm=Mminus(n(k),n(k),TE,K0);
     else
         qm=qminus(h(k-1)); Mm=Mminus(n(k-1),n(k),TE,K0);end;
     Nm=Nminus(h(k));
     C=qm*Mm*Nm;

     C=[C
         qminus(h(k))];

     C=[C
         1 0 0 0 0];

     if k>mx-1
         qp=qplus(h(k));
     Mp=Mplus(n(k),n(k),TE,K0);
else
     qp=qplus(h(k+1));
     Mp=Mplus(n(k),n(k+1),TE,K0);end

C=[C
  qp*Mp];

     if k>mx-2
           qp=qplus(h(k));
     Mp1=Mplus(n(k),n(k),TE,K0);
     Np=Nplus(h(k));
     Mp0=Mplus(n(k),n(k),TE,K0);
else
     qp=qplus(h(k+2));
     Mp1=Mplus(n(k+1),n(k+2),TE,K0);
     Np=Nplus(h(k+1));
     Mp0=Mplus(n(k),n(k+1),TE,K0);end

     C=[C
         qp*Mp1*Np*Mp0];
C=inv(C);
Qt=[Qt
     C(3,:)];
C(3,:);
end
%%% Q Matrix %%%
Qtpp=[0
     0
     Qt(1:mx-2,5)];
Qtp=[0
     Qt(1:mx-1,4)];
Qt0=Qt(:,3)+K0^2*n;
```

```
Qtm=[Qt(2:mx,2)
    0];
Qtmm=[Qt(3:mx,1)
   0
   0];
Qt=[Qtmm Qtm Qt0 Qtp Qtpp];

Q=spdiags(Qt,-2:2,mx,mx);
Q=full(Q);
```

Functions of Five-Point

```
%******************** Start of function Mminus *********************%

% This function construct the matrix M(-) of equation 3.29

function y=Mminus(n1,n2,TE,K0)
if TE==1;rho=1;else rho=n1/n2;end;% sqr it before
del=K0^2*(n1-n2);

y=[1           0           0           0           0
   0           rho         0           0           0
   -del        0           1           0           0
   0           -rho*del    0           rho         0
   del^2       0           -2*del      0           1];

%******************** End of function Mminus *********************%

%******************** Start of function Mplus *********************%

% This function construct the matrix M(+) of equation 3.29

function y=Mplus(n1,n2,TE,K0)
if TE==1;rho=1;else rho=n2/n1;end% sqr it before
del=K0^2*(n2-n1);

y=[1           0           0           0           0
   0           rho         0           0           0
   -del        0           1           0           0
   0           -rho*del    0           rho         0
   del^2       0           -2*del      0           1];

%******************** End of function Mplus *********************%

%******************** Start of function Nminus *********************%
```

```
% This function construct the matrix N(-) of equation 3.31

function y=Nminus(h)
h1=-h;
y=[1          h1          h1^2/2        h1^3/6        h1^4/24
    0          1            h1           h1^2/2        h1^3/6
    0          0            1            h1            h1^2/2
    0          0            0            1             h1
    0          0            0            0             1];

%******************* End of function Nminus **********************%

%****************** Start of function Nplus **********************%

% This function construct the matrix N(+) of equation 3.31

function y=Nplus(h)
h1=h;
y=[1          h1          h1^2/2        h1^3/6        h1^4/24
    0          1            h1           h1^2/2        h1^3/6
    0          0            1            h1            h1^2/2
    0          0            0            1             h1
    0          0            0            0             1];

%******************** End of function Nplus **********************%

%****************** Start of function qminus **********************%

% This function construct the matrix N(+) of equation 3.30

function y= qminus(h);
y=[1 -h h^2/2 -h^3/6 h^4/24];

%****************** End of function qminus **********************%

%****************** Start of function qplus **********************%

% This function construct the matrix N(+) of equation 3.30

function y= qplus(h);
y=[1 h h^2/2 h^3/6 h^4/24];

%******************* End of function qplus **********************%
```

Appendix E

The PML Program

```
%******************** Start of function pml2b **************************%

% This function includes layers of PML with the vector of refractive
% indices of layers (n and n1) and Vector of layer widths (h and h1)

function [n1,h1,n,M,h]=pml2b(EQ,w,M,n,npml,pmlpro,pmls);
%%% NON UNIFORM MESH ( h = discritization distance )
if EQ~=1
    h=w./M;
else        %%% UNIFORM MESH
    h=w(2)/M(2);
    h=h*ones(1,nlyr);
    w=M*h(1);
end

pmlu=ones(1,npml(1));
pmld=ones(1,npml(2));
xi=[];
xi(1)=(pi/2)/(npml(1)+1);
xi(2)=(pi/2)/(npml(2)+1);
```

132

```
n1=[n(1)*ones(1,npml(1))];for i1=1:length(n);n1=[n1
n(i1)*ones(1,M(i1))];end;n1=[n1  n(end)*ones(1,npml(2))];

if pmlpro==1

h1=[pmlu*h(1)];for i1=1:length(n);h1=[h1 h(i1)*ones(1,M(i1))];end;h1=[h1
pmld*h(end)];
n=[n(1) n n(end)];
M=[npml(1) M npml(2)];
%%%% h matrix open %%%
i2=1;%down
for i1=(length(h1)-npml(2)+1):length(h1)  % Uniform
    h1(i1)=h1(i1)+j*(pmls(2)/npml(2));
    i2=i2+1;
end

i3=1;%%up
i2=npml(1);
for i1=1:npml(1)     % Uniform
    h1(i2)=h1(i2)+j*(pmls(1)/npml(1));
    i3=i3+1;
    i2=npml(1)-i1;
end

%%%%%% h matrix with values of all regions %%%
h=[];
M1=cumsum(M);
for i1=1:length(M1)-1
    h2=h1(M1(i1));
    h=[h,h2];
end
h=[h,(h1(M1(i1)+1))];

end


if pmlpro~=1

    h1=[h(1)*ones(1,npml(1))];for i1=1:length(n);h1=[h1
h(i1)*ones(1,M(i1))];end;h1=[h1 h(end)*ones(1,npml(2))];
    n=[n(1)*ones(1,npml(1)) n n(end)*ones(1,npml(2))];
    M=[ones(1,npml(1)) M ones(1,npml(2))];

%     h=[h(1)*ones(1,npml(1)) h h(end)*ones(1,npml(2))];

    %%%% h matrix open %%%
    i2=1;%%down
```

```matlab
    for i1=(length(h1)-npml(2)+1):length(h1)
        if pmlpro==2  %%%% Linear
            h1(i1)=h1(i1)+j*(pmls(2)/npml(2))*i2*xi(2);
        elseif pmlpro==3  %%%% Parabolic
            h1(i1)=h1(i1)+j*(pmls(2)/npml(2))*i2*((xi(2))^2);
        elseif pmlpro==4                %%%% tan
            h1(i1)=h1(i1)+j*(pmls(2)/npml(2))*(tan(i2*xi(2)));
        end
        i2=i2+1;
    end
    i3=1;%%up
    i2=npml(1);
    for i1=1:npml(1)
        if pmlpro==2  %%%% Linear
            h1(i2)=h1(i2)+j*(pmls(1)/npml(1))*i3*xi(1);
        elseif pmlpro==3  %%%% Parabolic
            h1(i2)=h1(i2)+j*(pmls(1)/npml(1))*i3*((xi(1))^2);
        elseif pmlpro==4                %%%% tan
            h1(i2)=h1(i2)+j*(pmls(1)/npml(1))*(tan(i3*xi(1)));
        end
        i3=i3+1;
        i2=npml(1)-i1;
    end
    %%%%%%% h matrix closed
    h=[];
    M1=cumsum(M);
    for i1=1:length(M1)-1
        h2=h1(M1(i1));
        h=[h,h2];
    end
    h=[h,(h1(M1(i1)+1))];

end
%********************* End of function pml2b *************************
```

Appendix F

The Program for Add/Drop Filter and Its Functions

The Program for Add/Drop Filter

```
%_____
% Written By: Mohammad Mahbubul Isalm
% This program will calculate the Transmissivities (T2, T3, and T4),
Reflectivity R1 % and FPR.
% by using the Method of Lines (MOL).
%_____
clear all;close all;clc;
time=cputime; % time counter
TE=1;% TE mode (TE=1) %%%%% Tm mode (TE=0);
EQ=0;% UNIFORM MESH (EQ=1) %%%%EQ=1;
Ta=[];Dra=[];Ra=[];Dla=[];reda=[];
loop=0; % loop counter
```

```
%%%% Square cavities %%%%
nm=[ 1        1        1        1        1
     3.2      3.2      3.2      3.2      3.2
     1        1        1        1        1
     1        3.2      1        3.2      1
     1        1        1        1        1
     3.2      3.2      3.2      3.2      3.2
     1        1        1        1        1];
                              %%% layer refractive index in column


sep=.715; %%% Seperation between the cavities
Dv=[1.54    sep    1.54];  %%%layer width
w=[1    .2       .32      1.54     .28      .2      1]; %%% vector with widths
of layers


%%%% For Circular cavity %%%%
radiusR=0.85; %%% Radius of the circle
for radius=radiusR
nlr=30; %%% sections in redius of the circle along z-axis
[delZ,delX,nm]=Circle3(nlr,radius); %% nm layer by layer refractive index
in column, cavlayer- # of regions in x-axis


%%%% For Elliptical cavity %%%%
MltR=1.1; %%% Radius multiplier
for Mlt=MltR
Dv=delZ.*Mlt;  %%%layer width in z-axis


AG=0.15; %%% Airgap
for Agap=AG
[i2,i1]=size(nm);
w=[1    .2       Agap     delX     Agap     .2      1];% vector with widths of
layers
M=ceil(25*w); % discretizations of layers (superst, core, subst.)
npml=[5 5];   %number of pml points
pmls=[1.2 1.2]; %Eta, PML strength parameter
pmlpro=4;  %pml profile, 1=uni[form, 2=linear, 3=parabolic, 4=tan


rangeL=1.35:0.002:1.88;  %%% Wavelength
for lambda=rangeL
    K0=2*pi/lambda; %%% free space wavenumber



%%%% Q Matrix and Fundamental mode calculation %%%%
Uv=[];Gv=[];
for i2=1:i1
    n=nm(:,i2)';  % reflective index of the layers (superst, core, subst.)
    [n1,h1,n,M1,h]=pml2b(EQ,w,M,n,npml,pmlpro,pmls);    %%%% applying PML
```

```
        Q=fiveptDrJ(n1,h1,TE,K0);    %%%% calculating the Q matrix
        N=diag(n1.^2);
        [U,f,V]=Sqroot(Q); % Square root of Q matrix
        if TE==1;else U=(N^-1)*U;end
        Uv=[Uv,U];

        if i2==1;
            x=cumsum(real(h1))-(sum(real(h1))/2);%%% X axis
            %%% fundamental modes calculation
            [a,b]=min(imag(f));
            a=f(b);
            mx=length(h1);
            uu=V(1:ceil(mx/2),b); % locating the middle of the problem space
            [a2,b2]=max(abs(uu));
            V(:,b)=V(:,b)/V(b2,b); % normalize

            A=abs(V(:,b));

            Aup=A;Aup(ceil(length(Aup)/2):length(Aup))=0;
            Alo=A;Alo(1:ceil(length(Alo)/2))=0;
            A=Aup; % source field in the top core

%           figure;plot(x,V(:,b));hold on;plot(x,A,'or');plot(x,Alo,'.k');
        end

        if i2==1||i2==i1;
        else dd=exp(j*f*Dv(i2-1));
                dd=diag(dd);
                G=V*dd/V;
                Gv=[Gv,G];
        end
    end
end
I=eye(size(Q));lenI=length(I);

%%% Reflection matrix calculation %%%
Rv=[];
for i2=1:i1-1
    i3=i1-i2;
    if i2==1
        R=(I-(Uv(:,((((i3-1)*lenI)+1):(i3*lenI)))^-
1)*Uv(:,((i3*lenI)+1):((i3+1)*lenI)))*((I+(Uv(:,((((i3-
1)*lenI)+1):(i3*lenI)))^-1)*Uv(:,((i3*lenI)+1):((i3+1)*lenI)))^-1);
        Rv=[R,Rv];
    else
        UU=(Uv(:,((((i3-1)*lenI)+1):(i3*lenI)))^-
1)*(Uv(:,(((i3*lenI)+1):((i3+1)*lenI)))));
```

```
        GRG=(Gv(:,(((((i3-
1)*lenI)+1):(i3*lenI)))))*Rv(:,(1:lenI))*(Gv(:,(((((i3-
1)*lenI)+1):(i3*lenI)))));

        R=((I-UU)+(I+UU)*GRG)*(((I+UU)+(I-UU)*GRG)^-1);
        Rv=[R,Rv];
    end
end

%%% Tramsmissivity and Reflectivity calculation %%%
Av=[];Bv=[];
for i2=1:i1
    if i2==1    %%% first layer
        Av=[Av,A];
        B=Rv(:,(1:lenI))*A;
        Bv=[Bv,B];
    elseif i2==2    %%% second Layer
        UU=(Uv(:,(((((i2-1)*lenI)+1):(i2*lenI)))^-1)*(Uv(:,(((((i2-
2)*lenI)+1):(i2-1)*lenI)));
        Aloc=0.5*((I+UU)*Av+(I-UU)*Bv);
        Av=[Av,Aloc];
        Bloc=Rv(:,(((((i2-1)*lenI)+1):(i2*lenI)))*(Gv(:,(((((i2-
2)*lenI)+1):((i2-1)*lenI)))*Aloc);
        Bv=[Bv,Bloc];
    elseif i2==i1    %%% last layer
        Aloc=0.5*((I+(Uv(:,(((((i2-1)*lenI)+1):(i2*lenI)))^-1)*(Uv(:,(((((i2-
2)*lenI)+1):(i2-1)*lenI)))))*Gv(:,(((((i2-3)*lenI)+1):((i2-
2)*lenI)))*Av(:,(i2-1))+(I-(Uv(:,(((((i2-1)*lenI)+1):(i2*lenI)))^-
1)*(Uv(:,(((((i2-2)*lenI)+1):(i2-1)*lenI))))*Bv(:,(i2-1)));
        Av=[Av,Aloc];
    else
        Aloc=0.5*((I+(Uv(:,(((((i2-1)*lenI)+1):(i2*lenI)))^-1)*(Uv(:,(((((i2-
2)*lenI)+1):(i2-1)*lenI)))))*Gv(:,(((((i2-3)*lenI)+1):((i2-
2)*lenI)))*Av(:,(i2-1))+(I-(Uv(:,(((((i2-1)*lenI)+1):(i2*lenI)))^-
1)*(Uv(:,(((((i2-2)*lenI)+1):(i2-1)*lenI))))*Bv(:,(i2-1)));
        Av=[Av,Aloc];
        Bloc=Rv(:,(((((i2-1)*lenI)+1):(i2*lenI)))*(Gv(:,(((((i2-
2)*lenI)+1):((i2-1)*lenI)))*Aloc);
        Bv=[Bv,Bloc];
    end
end
%
T=(Av(:,i1).*Aup).'*real(h1).';
T=T/((Aup.*Aup).'*real(h1).');
T=abs(T)^2;Ta=[Ta,T]; %%% T2

Dr=(Av(:,i1).*Alo).'*real(h1).';
```

```
Dr=Dr/((Alo.*Alo).'*real(h1).');
Dr=abs(Dr)^2;Dra=[Dra,Dr]; %%% T3

R=(B.*Aup).'*real(h1).';
R=R/((Aup.*Aup).'*real(h1).');
R=abs(R)^2;Ra=[Ra,R]; %%% R1

Dl=(B.*Alo).'*real(h1).';
Dl=Dl/((Alo.*Alo).'*real(h1).');
Dl=abs(Dl)^2;Dla=[Dla,Dl]; %%% T4

red=1-(T+R+Dl+Dr);reda=[reda,red];loop=loop+1 %%% FPR
end
end
end
end
Mlt=MltR;
radius=radiusR;
lambda=rangeL;
Agap=AG;
time=(cputime-time)/60
%figure;plot(radius,Ta,'r',radius,Ra,'c',radius,Dla,'m',radius,Dra,'k',radi
us,reda);%%% Varying Radius
%figure;plot(Agap,Ta,'r',Agap,Ra,'c',Agap,Dla,'m',Agap,Dra,'k',Agap,reda);
%%% Varying Air gap
figure;plot(lambda,Ta,'r',lambda,Ra,'c',lambda,Dla,'m',lambda,Dra,'k',lambd
a,reda);%%% Varying Wavelength
% figure;plot(Mlt,Ta,'r',Mlt,Ra,'c',Mlt,Dla,'m',Mlt,Dra,'k',Mlt,reda); %%%
Varying multiplier
exit
```

Function of the Program

```
%****************** Start of function Sqroot  *********************%

% This function generates the Square root of the matrix Q

function[S,f,V]=Sqroot(Q);

[V,D]=eig(Q);% Eigen Value(D) and Eigen Vector(V) Matrix
D=diag(D);
f=sqrt(D);
for rep=1:length(f);    % Making all the imaginary parts of V in to
positive.
```

```
    if imag(f(rep))<0; f(rep)=conj(f(rep));end;
end;
S=V*diag(f)/V; % sqrt of Q

%****************** End of function Sqroot  *********************
```

Bibliography

[1] S. E. Miller, "Light propagation in generalized lenslike media," *Bell Syst. Tech. Journal,* vol. 44, PP.2017-2064, 1965.

[2] S. E. Miller, *"Integrated Optics: an Introduction,"* *Bell Syst. Tech. Journal,* vol. 48 PP.2059-2069, 1969.

[3] H. Nishihara, M. Haruna, and T. Suhara, *Optical Intigrated circuits.* McGrawHill, 1989.

[4] A. Sharma, *"Collocation Method for Wave Propagation Through Optical Waveguide Structures",* Progress in Electromagnetic Research, (PIER) 11, Elsevier Science Publications Co., Inc., 1995.

[5] A. K. Ghatak and K. Thyagarajan, *Optical Electronics*. Cambridge Press, 1989..

[6] Alexander M. Kenis, Ilya Vorobeichik, Meir Orenstein, and Nimrod Moiseyev, *"Non-Evanescent Adiabatic Directional Coupler,"* *IEEE Journal of Quantum Electronics*, Vol. 37, No. 10, Oct. 2001

[7] C. Kostrewa, K. Peterman, *"Bandwidth optimizationof optical Add/drop multiplexers using cascaded and Mach-Zehnder sections"*, IEEE Photonics Technology Letters, p 902-904, vol. 7, Aug. 1995.

[8] R. G. Walker, J. Urquhart, I. Bennion, A. C. Carter, *"1.3/1.53 mum Mach-Zehneder wave length duplexers integrated optoelectronics modules",* IEE proceedings on Optoelectronics, P 33-38, Vol 137, Feb. 1990.

[9] D. G. Rabus, M. Hamacher, H. Heidrich, U. Troppenz, *" Box like filter response of triple ring resonators with integrated SOA sections based on GaInAsP/ Inp".*

[10] H. H. Yaffe, C.H. Henry, M. R. Serbin, L. G. Cohen, *"Resonant couplers acting as add/drop filters made of silica-on silicon waveguide technology",* Journal of light wave technology, vol 12, p 1010- 1019, June 1994.

[11] C. Kostrewa, K. Peterman, R. Moosburger, G. Fischbeck, B. Schuppert, *"Tunable Polymar optical add/drop filter for multi wavelengthnetwork".* IEEE Photonics tech letters," vol. 9, p 1487-1489, Nov. 1997.

 [12] H. M. Masoudi, M. Al-Sunaidi, andJ. M. Arnold, *"Time-domain finite difference beam propagation method,"* IEEE Photonics technology Letters, vol. 11, pp. 1274-1276, Oct. 1999.

[13] R. Scarmozzino. A. Gopinath, R. Pregla, and S. Helfert, *"Numerical techniques for modeling guided-wave photonic devices,"* IEEE Journal of selected topics in Quantum Electronics, vol. 6, No. 1, pp. 150-162, Jan. 2000.

[14] S. T. Chu and S. K. Chaudhrui, *"Finite-difference-time-domine methods for Optical waveguide analysis."* Progress in Electromagnetics Research (PIER) 11, Elsevier Science Publishing Co. inc. 1995.

[15] A. K. Taneja and A. Sharma, *"Reflection characteristics of guided wave bragg gratings using the collection method,"* SPIE Proceeding, International conference on fiber optics and photonics, vol. 3666, pp. 112-119, April 1999.

[16] Q, H. Liu and W. C. Chew, *"Analysis of discontinuities in planar dielectric waveguide, An eigen mode propagation method," IEEE Transactions on Microwave Theory and Techniques,* vol. 39, pp. 422-430, Mar. 1991.

[17] U. Rogge and R. Pregla. *"Method of lines for the analysis of strip loaded optical waveguides," Optical society of America (B),* vol. 8 pp. 459-463, Feb. 1991.

[18] J. Geres and R. Pregla, *"Beam-propagation algorithm based on the method of lines," Optical society of America (B)*, vol. 8, pp. 389-394, Feb. 1991.

[19] J J Gerdes. Bidirectional eigenmode propagation analysis of optical waveguides based on method of lines. *Electronics Letters*, 30(7) 550, March 1994.

[20] S. T. Peng and T. Tamir. TM mode perturbation analysis of dielectric gratings. *Applied Physics*, 7(35) 35-38, 1975.

[21] Jose Rodriguez, R. D. Crespo, and S. Fernandez. Radiation losses on discontinuities in integrated optical waveguides. *Optical Engineering*, 38(11) 1896-1906, November 1999.

[22] Al-Bader S. J. and Jamid H. A. Mode scattering by a non-linear step-discontinuity in dielectric optical waveguides. *IEEE Transactions on Microwave theory and Techniques*, 44(2) 218-224, February 1996.

[23] Y. P. Chiou and H. C. Chang, "Analysis of optical waveguide discontinuities using pade approximation," IEEE Photonics Technology Letters, vol. 9, pp. 964-966, 1997.

[24] J. Gerdes, B. Lunitz, D. Benish, and R. Pregla, "Analysis of slab waveguide discontinuities including radiation and absorption effects," Electronics Letters, vol. 28, p. 1013, May 1992.

[25] J. Gerdes and R. Pregla, "Beam-propagation algorithm based on the method of lines," Optical Society of America (B), vol. 8, pp. 389-394, Feb. 1991.

[26] M. N. Akram, "Analysis of anti-resonant reecting optical waveguide (ARROW) grating using the method of lines," Master's thesis, King Fahd University of Petroleum and Minerals, Saudi Arabia, April 2000.

[27] W. D. Yang and R. Pregla, "Method of lines for analysis of waveguide structures with multidiscontinuities," Electronics Letters, vol. 31, p. 892, May 1995.

[28] R. Pregla and W. Yang, "Method of lines for analysis of multilayered dielectric wavegides with bragg gratings," Electronics Letters, vol. 29, p. 1962, October 1993.

[29] R. Pregla and E. Ahlers, "Method of lines for analysis of discontinuities in optical waveguides," Electronics Letters, vol. 29, p. 1845, October 1993.

[30] A. A. Shittu, Study of periodic waveguides by the _nite-di_erence time-domain method and the Method of Lines. PhD thesis, King Fahad University of Petroleum and Minerals, Dhahran 31261, Saudi Arabia, September 1994.

[31] T. Itoh, ed., Numerical Techniques for Microwave and Millimeter-Wave Passive Structures. John Wiley and Sons Inc., 1989.

[32] E. Ahlers and R. Pregla, 3-D modeling of concatenations of straight and curved waveguides by MOL-BPM, Optical and Quantum Electronics, pp. 151{156), 1997.

[33] W. D. Yang and R. Pregla, The method of lines for analysis of integrated optical waveguide structures with arbitrary curved interfaces," *Journal of Lightwave Technology*, vol. 14, pp. 879-884, May 1996.

[34] F. H. Al-Harbi, \Implementation of a full vectorial method of lines analysis in the study of metal clad rib waveguide," *Master's thesis*, King Fahd Univeristy of Petroleum and Minerals, Saudi Arabia, December 2000

[35] S. J. Al-Badar and H. A. Jamid. Method of lines applied to non-linear guided waves. *Electronic letters*, 31(17):79-85, February 1995.

[36] M. Imtaar and S. J. Al-Badar. Analysis of diffraction from abruptly terminated optical fiber by the Method of lines. *Journal of lightwave Technology*, 13(2):137-141, February 1995

[37] M. J. Al-Majid, "Method of line analysis for Gaussian beam coupling of the dielectric slab waveguide," Master's thesis, King Fahd University of Petroleum and Minerals, Saudi Arabia, Feb. 1994.

[38] M.N. Akram, "Analysis of anti-resonant reflecting optical waveguide (ARROW) grating using the method of lines," Master's thesis, King Fahd University of Petroleum and Minerals, Saudi Arabia, April 2000.

[39] V. Vemuri and Walter J. Karplus, Digital Computer treatment of Partial Differential Equations. Prentice-Hall Series on Computational Mathematics. Prentice-Hal, Inc., Englewood Cliffs, New Jersey, 1981

[40] H. Diestel, Analysis of planar multiconductor transmission line systems with the method of lines, Arch. Elektron Ueber, vol. 41, pp. 169-175, 1987.

[41] H. Diestel and S. Worm, Analysis of hybrid field problems by the method of lines with nonequidistant discretization, *IEEE Trans. Microwave Theory Tech.*, vol. MTT-32, no. 6, pp. 633-638, 1984.

[42] Hussain A. Al-Jamid. A new Generalized finite difference higher order approach for the solution of the wave equation. *Personal notes*.

[43] Hussain A. Al-Jamid and Muhammad Nadeem Akram, A new higher order finite difference approximation schemes for method of lines, *Journal of lightwave technology*, 19(3):398-404, March 2001.

[44] A. Kurnatz and R. Pregla, Increasing in the order of approximation and improvement of the interface conditions for the method of lines, *Journal of lightwave technology*, vol. 11, pp. 249-251, February 1993

[45] S. J. Al-Badar and H. A. Jamid, "Perfectly matched layer absorbing boundary condisions for the method of lines modeling scheme," *IEEE Microwave and Guided Wave Letters,* 8(11):357-359, Nov 1998.

[46] H. A. Jamid, "Frecuency-Domain PML layer based on the complex mapping of space boundary condition treatment," *IEEE Microwave and Guided Wave Letters,* 10:356-358, Sep. 2000.

[47] H. A. Jamid, Enhanced PML performance using the higher order approximation, *IEEE Transactions on Microwave Theory and Techniques*, April 2004.

[48] R. Syms and J. Cozens, Optical Guided Waves and Devices. Shopenhangers Road, Maidenhead, Bershire, SL6 2QL, England,: McGraw-Hill Book Company Europ, 1992.

[49] Q.-H. Liu and W. C. Chew, Analysis of discontinuities in planar dielectric waveguides: An eigenmode propagation method, *IEEE Transactions on Microwave Theory and Techniques*, vol. 39, pp. 422-430, Mar. 1991.

[50] Y. P. Chiou and H. C. Chang, Analysis of optical waveguide discontinuities using pade approximation, *IEEE Photonics Technology Letters*, vol. 9, pp. 964-966, 1997.

[51] W. D. Yang and R. Pregla, Method of lines for analysis of waveguide structures with multidiscontinuities, *Electronics Letters*, vol. 31, p. 892, May 1995.

[52] R. Pregla and W. Yang, Method of lines for analysis of multilayered dielectric wavegides with bragg gratings, *Electronics Letters*, vol. 29, p. 1962, October 1993.

[53] J. J. Gerdes, Bidirectional eigenmode propagation analysis of optical waveguides based on method of lines, Electronics Letters, vol. 30, p. 550, March 1994.

[54] S. T. Peng and T. Tamir, TM mode perturbation analysis of dielectric gratings, *Applied Physics*, vol. 7, no. 35, pp. 35-38, 1975.

[55] A. A. Shittu, "Study of periodic waveguides by the finite-difference time domain method and the Method of lines," PhD thesis , King Fahd University of Petroleum and Minerals, Saudi Arabia, Sep. 1994.

[56] H. A. Jamid and M. N. Akram, "Analysis of deep waveguide gratings: An efficient Cascading and Doubling algorithm in the method of linesframe work." *Journal of lightwave technology*, 20(7):1204-1208, July 2002.

[57] J. Ctyroky, S. Helfert and R. Pregla, "Analysis of deep waveguide bragggrattings," *Optical and Quantum Electronics Letters*, vol. 14, pp. 1533-1535, Nov 2002.

[58] M. A. Khan, "Analysis of metal clad TM pass polarizer using the method of lines," *Master's thesis,* King Fahd University of Petroleum and Minerals, Saudi Arabia, Feb. 2001.

[59] Alexander M. Kenis, Ilya Vorobeichik, Meir Orenstein, and Nimrod Moiseyev, "Non-Evanescent Adiabatic Directional Coupler," *IEEE Journal of Quantum Electronics*, Vol. 37, No. 10, Oct. 2001

[60] Charles K. Kao, "Optical Fiber Systems: Technology, Design and Applications,"McGraw-Hill, 1982

[61] Bahaa E. Saleh and Malvin Carl Teich, "Fundamentals of Photonics,"John Wiley & sons, 1991

[62] C. Kostrewa, K. Peterman, "Bandwidth optimization of optical Add/drop multiplexers using cascaded and Mach-Zehnder sections, IEEE Photonics Technology Letters, p 902-904, vol. 7, Aug. 1995.

[63] R. G. Walker, J. urquhart, I. Bennion, A. C. Carter, "1.3/1.53 mum Mach-Zehneder wave length duplexers integrated optoelectronics modules", IEE proceedings on Optoelectronics, P 33-38, Vol 137, Feb. 1990.

[64] D. G. Rabus, M. Hamacher, H. Heidrich, U. Troppenz, " box like filter response of triple ring resonators with integrated SOA sections based on GaInAsP/ Inp.

[65] H. H. Yaffe, C.H. Henry, M. R. Serbin, L. G. Cohen, "Resonant couplers acting as add/drop filters made of silica-on silicon waveguide technology, Journal of light wave technology, vol 12, p 1010- 1019, June 1994.

[66] C. Kostrewa, K. Peterman, R. Moosburger, G. Fischbeck, B. Schuppert, "Tunable Polymar opticaladd/drop filter for multi wavelengthnetwork. IEEE Photonics tech letters," vol. 9, p 1487-1489, Nov. 1997.

[67] C. Manolatou, M. J. Khan, Shanhui Fan, Pierre R. Villeneuve, H. A. Haus, *Life Fellow, IEEE,* and J. D. Joannopoulos, "Coupling of Modes Analysis of Resonant Channel Add–Drop Filters," *IEEE Journal of Quantum Electronics*, Vol. 35, No. 9, Sep 1999.

[68] H. A. Haus, wave and Fields in Optoelectronics. Englewood Cliff, NJ, Prentice-Hall, 1994.

[69] H. M. Nussenzveig, Diffraction Effects in Semiclassical Scattering (Cambridge University, Cambridge, UK, 1992).

[70] C. Vedrenne and J. Arnaud, ''Whispering-gallery modes of dielectric resonators,'' IEE Proc. 129, 183–187 (1982).

[71] D. Cros and P. Guillon, ''Whispering gallery dielectric resonator modes for W-band devices,'' IEEE Trans. Microwave Theory Tech. 38, 1667–1674 (1990).

[72] L. Collot, V. Lefe`vr-Seguin, M. Brune, J. M. Raimond, and S. Haroche, ''Very high-Q whispering-gallery mode resonances observed in fused silica microspheres,'' Europhys. Lett. 23, 327–334 (1993).

[72] S. Chiller and R. L. Byer, ''High-resolution spectroscopy of whispering gallery modes in large dielectrics,'' Opt. Lett.16, 1138–1140 (1991).

[73] A. T. Rosenberger, ''Nonlinear optical effects in the whispering-gallery modes of microspheres,'' in OperationalCharacteristics and Crystal Growth of Nonlinear OpticalMaterials, R. B. Lal, D. O. Frazier, eds., Proc. SPIE 3793, 179–186 (1999).

[74] S. M. Spillane, T. J. Kippenberg, and K. J. Vahala, ''Ultralow-threshold Raman laser using a spherical dielectric microcavity,'' Nature 415, 621–623 (2002).

[75] V. S. Ilchenko, P. S. Volikov, V. L. Velichansky, F. Treussart, V. Lefe`vre-Seguin, J.-M. Raimond, and S. Haroche, ''Straintunable high-Q optical microsphere resonator,'' Opt. Commun. 145, 86–90 (1998).

[76] P. Rabiei, W. H. Steier, C. Chang, and L. R. Dalton, ''Polymer micro-ring filters and modulators,'' J. Lightwave Technol. 20, 1968–1975 (2002).

[77] V. S. Ilchenko, X. S. Yao, and L. Maleki, ''Pigtailing the high-Q microsphere cavity: a simple fiber coupler for optical whispering-gallery modes,'' Opt. Lett. 24, 723–725 (1999).

[78] P. Barthia and I. J. Bahl, Millimeter Wave Engineering and Applications (Wiley, New York, 1984).

[79] G. Annino, D. Bertolini, M. Cassettari, M. Fittipaldi, I. Longo, and M. Martinelli, ''Dielectric properties of materials using whispering-gallery dielectric resonators: Experiments and perspectives of ultra-wideband characterization,'' J. Chem. Phys. 112, 2308–2314 (2000).

[80]   Jiangquan Zhang and D. Grischkowsky. "Whispering-gallery-mode cavity for terahertz pulses," J. Opt. Soc. Am. B/Vol. 20, No. 9, page 1894-1904, September 2003

Vitae

1977: Born in Dhaka, Bangladesh.

1992: Secondary School Certificate examinations (SSC) in Science group.

1994: Higher Secondary Certificate examinations (HSC) in Science group.

1996 – 2001: Bachelor of Science in Electrical and Electronic Engineering from Islamic University of Technology, Gazipur, Bangladesh.

Major: Electronics.

2001 – 2002: Sales and Service Engineer, Tangent Engineering Limited, Dhaka, Bangladesh.

2002 – 2005: Master of Science in Electrical Engineering from King Fahd University of Petroleum and Minerals, Dhahran, KSA.

Major: Integrated Optics.